The effect of platform motions on turbine performance

A study on the hydrodynamics of marine current turbines on the floating tidal energy converter BlueTEC

MSc. Thesis P.C.A. van der Plas

MT1223429

Delft University of Technology

Faculty of Mechanical, Maritime and Materials Engineering

Department of Ship Hydromechanics

MSc. Thesis Pieter C.A. van der Plas

Delft University of Technology

June 2014

Committee:

Prof. Dr. ir. T.J.C. van Terwisga

Ir. M. Palm

Ir. A. Jarquin Laguna

Dr. A.C. Viré

Ir. W. Otto

Katwijk aan Zee,

June 27, 2014

Pieter van der Plas

Contents

List of symbols

Blade element momentum theory

α	angle of attack
α_{stall}	stall angle of attack
β	pitch angle of blade
γ	local twist of blade element
θ	local pitch angle of blade element
ρ	density
σ	blade solidity
ν	viscosity
ϕ	inflow angle
ω	rotor frequency
A	area of ring element
A_{rotor}	rotor area
a	axial induction factor
a_t	tangential induction factor
C_d	drag coefficient
$\mathrm{C_{d_{max}}}$	maximum drag coefficient
$\mathrm{C_{d_{stall}}}$	drag coefficient associated α_{stall}
C_l	lift coefficient
$\mathrm{C_{l_{max}}}$	maximum lift coefficient
C_n	normal (or axial) force coefficient
C_p	power coefficient
C_t	thrust coefficient
C_t	tangential force coefficient
c	local chord length
D	drag of blade element
dF_x	normal (or axial) force per ring element
dP	total deliverd power per ring element
dQ	total delivered torque per ring element
dr	height (or width) of (ring)element
dT	total delivered thrust per ring element
F_n	normal (or axial) force on blade element
F_t	tangential force on blade element
F_{tip}	tip loss correction factor
F_x	total normal (or axial) turbine force
i	element subscript
j	blade subscript
L	lift of blade element
N_b	number of blades
N_i	number of iterations
N_s	number of segments, or ring elements
P	total delivered power
Q	total delivered torque
R	turbine radius
Re	Reynolds number
r	local radius of blade element
T	total delivered thrust
$\mathrm{TSR_{local}}$	local tips speed ratio of blade element
t/c	thickness/chord ratio
U_c	current velocity
V_∞	free stream current velocity
V_{rel}	relative inflow velocity

Unsteady modelling

δ	wave elevation	F_x	total axial turbine force
ε_{blade}	phase of turbine blade	g	gravitational acceleration
θ	pitch motion, -angle	H_s	significant wave height
$\theta_{platform}$	platform pitch angle	k	wave number
$\dot{\theta}_{platform}$	platform pitch velocity	M_y	moment around y-axis
φ	velocity potential	T_p	peak period
φ	roll motion, -angle	t	time
ψ	yaw motion, -angle	$U_{current}$	current velocity component
ω	wave frequency	$U_{platform}$	platform velocity component
Ω	rotor rotation direction	U_{rel}	relative inflow velocity
		U_{wave}	wave velocity component
A	area of actuator disk strip	$U_{x,wave}$	horizontal orbital velocity
a	wave amplitude	$U_{z,wave}$	vertical orbital velocity component
c_n	axial force coefficient	U_∞	free stream current velocity
C_{tweak}	tweaking coefficient	x	surge motion, -location
D	water depth	$x_{platform}$	platform x-location
d	blade element distance	$\dot{x}_{platform}$	platform surge velocity
d	blade element distance to hub	x_0	x-location of CoG of platform
d_{hub}	hub depth	y	sway motion, -location
dn	height of actuator disk strip	z	heave motion, -location
dt	time step	z	local depth
F_{drag}	drag load of actuator disk	z_0	z-location of CoG of platform

Abbreviations

AR	Aspect Ratio
BEM	Blade Element Momentum
BEMT	Blade Element Momentum Theory
BlueTEC	Bluewater Tidal Energy Converter
CoG	Centre of Gravity
DoF	Degree of Freedom
NACA	National Advisory Committee for Aeronautics
SB	Starboard
TSR	Tip Speed Ratio

Abstract

Bluewater New Energy department is developing BlueTEC, a floating offshore support platform that is able to support multiple horizontal tidal turbines. In order to analyse how the floating structure behaves in operation and how large the mooring forces will be, a hydrodynamic model is needed to predict the motion behaviour of the platform. A good hydrodynamic model will enable Bluewater to vary different components of the platform in order to optimize floater design, mooring loads and turbine choice to accomplish an as cost-efficient platform as possible. The Bluewater New Energy department has performed several model tests with different concepts of BlueTEC.

This study focuses on the effects of platform motions on the turbine performance. A numerical model to analyse turbine performance is developed based on blade element momentum theory (BEMT). A tip loss correction factor is implemented in the numerical model and lift- and drag characteristics for the turbine geometry as tested by Bluewater have been obtained.

The BEM model is extensively verified and validated against results of comparable numerical models and results of tests in a cavitation and circulation tank that are published in literature by Bahaj et al. The developed BEM model showed good agreement for the design case of the turbine, especially for the operating range of the turbine. Validation against single rotor tests executed by Bluewater on the BlueTEC showed satisfying results for the design condition of the turbine as well.

An unsteady inflow field is developed, based on the current velocity profile, orbital velocities due to waves and hub induced velocities due to platform motions. A unidirectional environment is assumed, only velocity components in longitudinal direction are accounted for. The platform is assumed to only have motions in surge-, heave- and pitch direction. The resulting sheared velocity profile that is experienced by the turbine is accounted for in the BEM model by taking the average inflow velocity over the blade elements that are spanned by one ring element. Besides the BEM approach, the actuator disk theory is modified to incorporate an unsteady flow field.

The numerical approaches are verified with results for uniform inflow conditions with the steady BEM model to check if the calculation of relative inflow velocities at the blade elements and lookup tables for power- and thrust coefficients are correctly implemented. This showed spot on results. Time registrations of axial load on the turbine for different configurations of the platform and under different environmental conditions have been obtained during basin tests on the BlueTEC platform. These datasets are used to validate the numerical approaches in an unsteady flow field.

A captive platform is subjected to a current only condition and a combined current and wave loading. In both situations no platform motions are present and the relative inflow velocity at the blades is the results of current velocity and orbital velocity due to waves. The same is repeated for a moored platform. Both the actuator disk approach and the BEM approach showed satisfying results in current only conditions for both captive and moored platform. When waves are added, the numerical models still show nice results for the captive platform. For the moored platform the numerical models fails to predict the behaviour of the axial loading that was observed during model tests. For this configuration the coupling effect from turbine loading to platform motions cannot be neglected and this effect is not accounted for in the numerical approaches.

The mean values of the axial load are fairly well predicted and the fluctuating behaviour due to wave loading is shown by both approaches. In general the BEM approach has the tendency to over predict the loading and showed higher amplitudes for the case were current and waves are combined. Both numerical models showed to be sensitive to the used current velocity profile and proper choice of this profile is of significant influence on the results of the numerical model. A more accurate actuator disk approach, with improved drag coefficients, could serve as a calculation method to implement in a coupled model. To analyse turbine loading this is a simple, fast and reliable method. The developed BEM model showed to give satisfying results for the analysis of turbine performance for a static turbine in uniform inflow conditions.

1 Introduction

Bluewater New Energy department is developing BlueTEC, a floating offshore support platform that is able to support horizontal tidal turbines. The platform consists of a longitudinal floater and a crossbeam in transverse direction. Two horizontal tidal energy turbines are connected by struts to the crossbeam and are capable of delivering 1 MW of power in total. Chapter 1 introduces the concept of BlueTEC and the problems associated with the developed of the platform with respect to the hydrodynamics of the turbines.

1.1 Problem description

Bluewater New Energy department is developing BlueTEC, a floating offshore support platform that is able to support multiple horizontal tidal turbines, see Figure 1-1. With its expertise in the offshore industry, the department focuses on the design of the floating support structure and the mooring system. For the turbines and control system, an existing type from a turbine manufacturer will be selected. Currently, the Bluewater New Energy department has performed several model tests with different concepts of BlueTEC. A full scale demonstration project is planned for a 1 MW unit at the test site of the European Marine Energy Centre located at the Orkney Island near the coast of Scotland.

In order to analyse how the floating structure behaves in operation and how large the mooring forces will be, a hydrodynamic model is needed to predict the motion behaviour of the platform. A good hydrodynamic model will enable Bluewater to vary different components of the platform in order to optimize floater design, mooring loads and turbine choice to accomplish an as cost-efficient platform as possible.

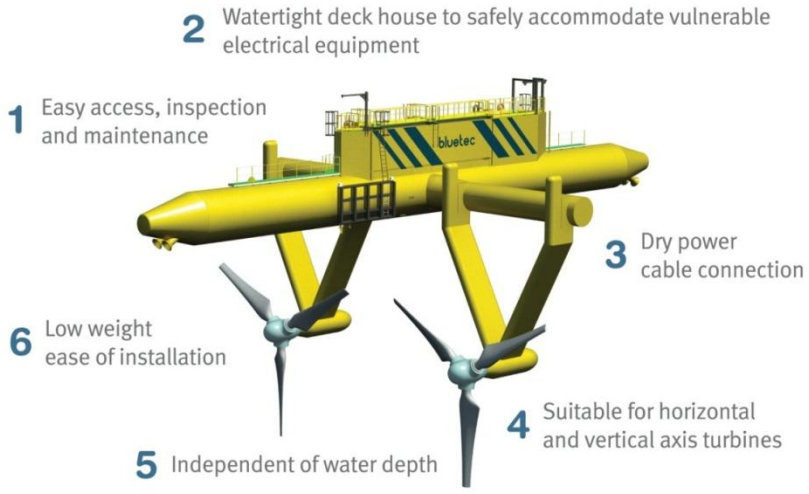

Figure 1-1: BlueTEC, a floating tidal energy converter platform

The floating platform is a complex coupled system; forces exerted by the turbines on the platform influence its motion behaviour, but this motion behaviour does in its turn influence the loading on the turbines by a changing inflow velocity and angle. At the same time, a control system ensures the power output of the turbine is kept constant by adjusting the rotational velocity or pitch angle of the turbine blades. A schematic overview of the coupled system is shown in Figure 1-2.

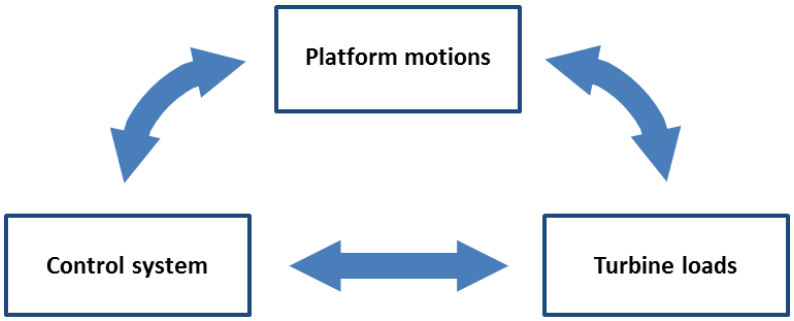

Figure 1-2: Schematic overview of the coupled dynamic simulation model (1)

To calculate the turbine loads, the relative inflow velocity on the turbine blades is considered. This relative inflow velocity is the result of the presence of current and waves and a third component. This third component is the result of platform motions. Motions of the platform induce a motion of the rotor hub and this contributes to the relative inflow velocity.

1.2 Objective & scope

The objective of Bluewater is to develop the most suitable and efficient floater design, mooring system and to calculate dynamic turbine loads and controller response. To be able to do so, as much knowledge needs to be gained on how the turbine operates in high velocity current and how the turbine influences the motion behaviour of the supporting platform.

This study focuses on the influence of the motion behaviour of the platform on the characteristics of the turbine. The aim of the study is to develop a model which is able to calculate the forces on the turbine as a result of environmental inflow fluctuations and platform motions. The objective is to analyse the hydrodynamics associated with a turbine connected to a floating platform and to gain knowledge about the platform motion behaviour under specific environmental conditions.

The approach to gain more knowledge with respect to the behaviour of the turbine is to analyse the effect of platform motions on turbine loading by using platform motions as input for the load simulation.

In this thesis the Blade Element Momentum theory (BEMT) will be used to model the loading on the turbine. Results of numerical models will be validated against scaled basin test results for static and dynamic conditions. The BEMT is a relatively simple approach based on 2-D lift- and drag characteristics of the blade sections of the turbine to calculate thrust and power output of a turbine. Because the environmental inflow velocity varies in time, the BEMT will be adjusted in such a way that simulations in time domain are possible. The relative flow field on each turbine blade will be calculated by a combination of theory and experimental measurements. Wave theory is used to calculate the wave induced particle velocity, significant wave height and wave periods will be obtained from measurement data. The current velocity profile is provided by the testing facility for a specific testing condition. Time series of platform motions are available from measurements which can be translated to hub motions. The output of the time domain BEM model can be compared to time series of axial turbine loads from experiments. This provides a valuable dataset for the validation of the numerical model and investigation of the hydrodynamic behaviour of the rotor.

The combination of available experimental data and the need to analyse the influence of platform motions on turbine loading creates a one-way approach; platform motions and environmental inflow are used to model the turbine loading. The numerical model does not predict the influence of varying turbine loads on the platform motion behaviour. The output of the model will be used to identify when differences between the numerical model and the basin tests occur and by which hydrodynamic effects these differences are

caused. The influence of the control system is not considered in this study. This reduces the schematic overview of Figure 1-2 to the simplified version shown in Figure 1-3.

Figure 1-3: Schematic overview of the coupling considered in this study

To capture the influence of the platform motion behaviour on the turbine loading a correct description of the flow field is of great importance. Besides the required input for the classical BEM theory as described in available literature, the input for this model will consist of time series of water particle velocities due to current, waves and motions of the hub due to platform motions. Time series for the wave induced water velocity will be calculated by the linear wave theory, time series from hub motions are obtained from the test data. A current velocity profile of the test basin is known and will also serve as input to the model. The output of the model will be validated against the test data.

A workflow diagram of the numerical model is shown in Figure 1-4.

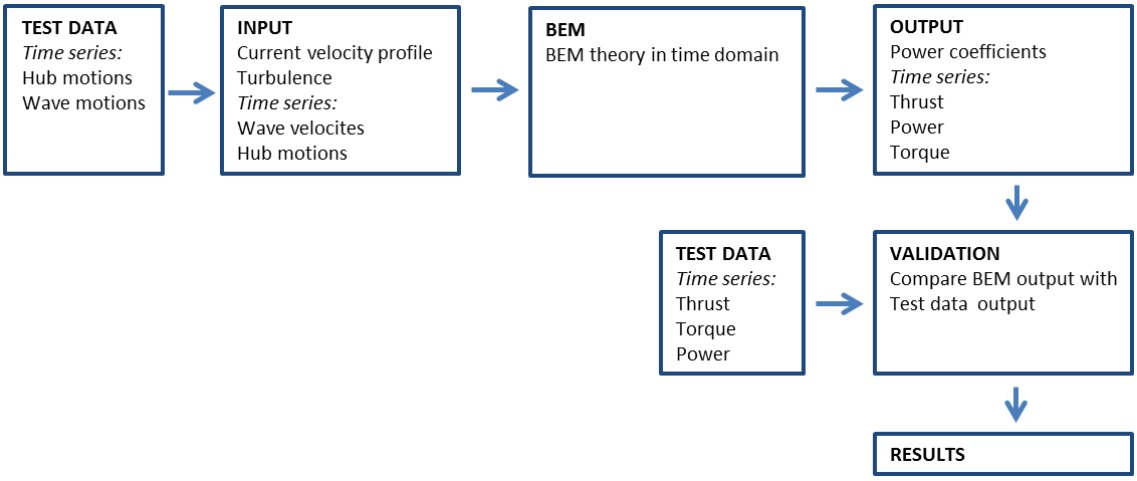

Figure 1-4: Workflow diagram of the BEMT model

1.3 Relevance

While most tidal energy developments focus on bottom founded structures, Bluewater is one of the few that sees great potential in a floating support platform. Up to date, only one floating tidal energy converter is installed by Scotrenewables. A lot of research is done on the behaviour of bottom founded tidal turbines, and many of these studies use the BEMT to model turbine loading. Recent interest from the industry in floating solutions is increasing as bottom founded structures appear to be expensive with respect to installation and maintenance.

Not much is known however on how a tidal turbine will operate supported by a moored platform. Positioning of the turbine near the sea surface and platform motions will most likely influence the loading of the turbine and knowledge of these effects is important for the design and development of the support structure.

The knowledge gained during this study can serve as valuable information for the further development of a coupled dynamic model in which the turbine loading would serve as an input for the simulation of the motion behaviour of the platform.

1.4 Approach

The development of a hydrodynamic model of the turbine can be divided in a number of steps, see Figure 1-5.

The first step is to develop a basic, steady BEM model and validate this model with existing models which can be derived from literature and previous work. Next, the model will be checked on convergence and look-up tables of the power-, thrust- and axial load coefficients for different pitch angles and tip speed ratios can be generated.

The second step is to use the lookup tables of the BEM model in time domain simulations in order to compare the output of the numerical simulations with the load registrations of the basin tests. In order to do so, time series of the flow field, consisting of wave and current velocity profile are generated to serve as input for the numerical model. An unsteady flow field with a fixed hub (i.e. captive platform) as input for the BEM model can be compared with the results of the captive model tests.

To be able to analyse the moored tests, the flow field is extended with the hub motions as an input for the analysis of the moored model tests. This leads to the final step, where the numerical model is implemented in an unsteady flow which is built up from environmental inflow fluctuations and platform motions. The results of the moored basin tests will be used to validate the unsteady model.

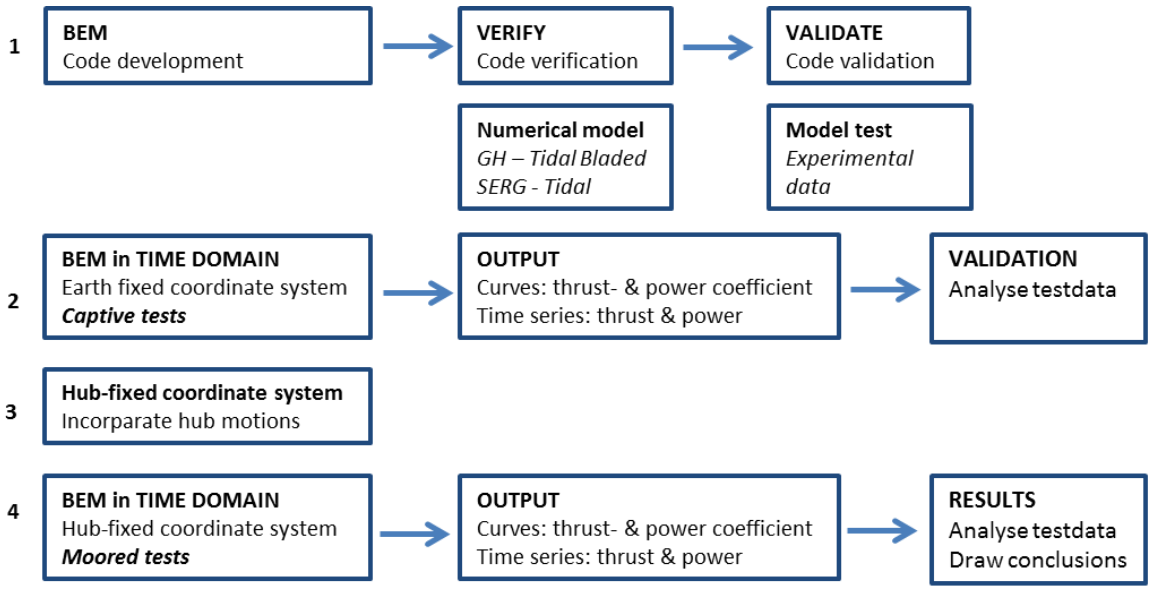

Figure 1-5: Schematic overview of the approach

2 Steady BEM model

Chapter 2 discusses the development of a numerical model based on the blade element momentum theory in order to analyse the loading and performance of a horizontal axis turbine operating in a marine current. Only a general overview of the theory is given in Chapter 2.1. For a detailed overview of the theory involved in BEMT, the reader is referred to the definition study that is part of this thesis (2). Important additions to the standard BEMT are given in Chapter 2.2 and Chapter 2.3 were the tip loss correction model and the generation of the 2-D lift- & drag coefficients are discussed respectively. The chapter continues with schematic overviews of the BEM theory and how this is implemented in the numerical model. This is discussed in Chapter 2.4.

2.1 Blade Element Momentum Theory

The blade element momentum theory is extensively described in the definition study of this thesis (2). In this paragraph the approach and goal of the BEM theory will be explained shortly and summary of the steps taken in the BEM theory is given.

BEM theory makes it possible to calculate the *steady* loads, thrust and power, for different setting of current velocity, rotational speed and pitch angle of the turbine. The theory couples 1-D momentum theory and the local loads on the blades. The stream tube as used in 1-D momentum theory is divided into N_s ring elements of height dr, as shown in Figure 2-1.

BEM theory assumes the following for the ring elements:

1. No radial dependency – in other words what happens at one element cannot be felt by the others;
2. The force from the blades on the flow is constant in each ring element; this corresponds to a rotor with an infinite number of blades.

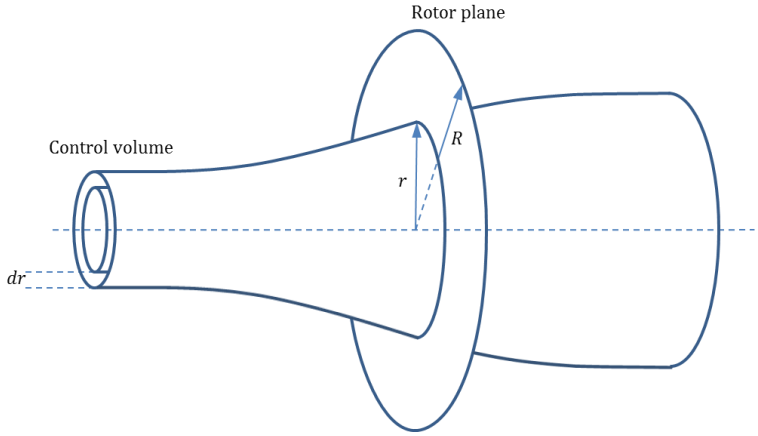

Figure 2-1: Control volume shaped as an annular element to be used in the BEM model

Figure 2-2 shows how a tidal stream turbine is represented in the theory. The figure shows a number of ring elements (N_s). A ring element is indicated by i. The ring element closest to the hub is indicated by $i = 1$. This number increases for increasing radius. .The number of blades (N_b), considered in this study is equal to three, a blade is indicated by j. The turbine position as showed in Figure 2-2 is its zero position. The vertical blade is indicated by $j = 1$, this number increases in for the following blades in clockwise direction.

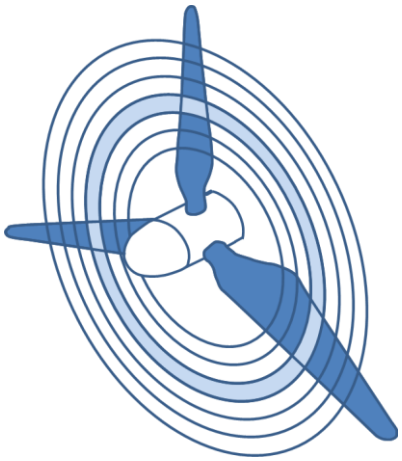

Figure 2-2: Numbering of ring elements and turbine blades for a rotor in BEMT

For the local events taking place on a blade element, the foil geometry is of importance. This varies in span-wise direction. Each ring element is considered as a 2-D foil and its foil geometry is defined in Figure 2-3.

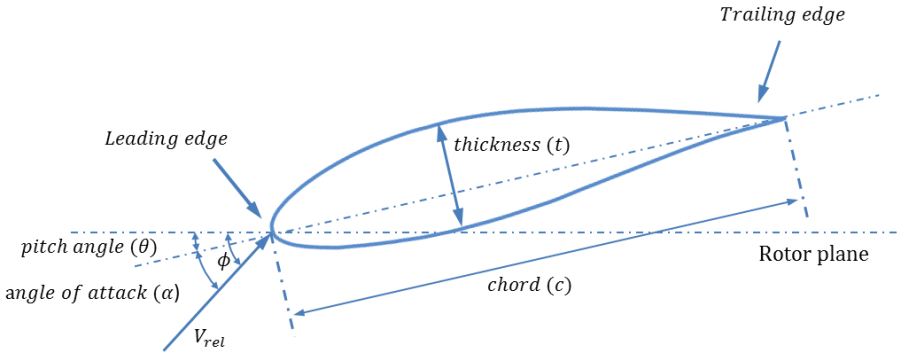

Figure 2-3: Foil geometry

BEM theory follows a number of steps to analyse the steady loads on a turbine. The main part consists of finding converged values for the axial- and tangential induction factor. The steps are described below.

1. Initialize the axial induction factor a and the tangential induction factor a_t;
2. Compute the inflow angle ϕ;
3. Compute the local angle of attack α;
4. Read off the lift coefficient $C_l(\alpha)$ and the drag coefficient $C_d(\alpha)$ from the lookup tables;
5. Compute the normal force coefficient C_n and tangential force coefficient C_t;
6. Calculate a and a_t;
7. If a and a_t have changed more than a certain tolerance, go to step (2) or else finish;
8. Compute the local loads on the segments of the blades. The total load on the turbine is calculated by summing up the local loads on all the ring elements.

Between step 1 and 2 a number of geometry calculation need to be done. These are discussed in the definition study of this thesis (2). Parameters indicated by i are related to that specific ring element, parameters indicated by j are related to a specific turbine blade.

Step 1

Initial values for the axial- and tangential induction, a and a_t, are needed to start the simulation. Normally zero or a value close to zero withstands to start the analysis.

Step 2

Figure 2-4 shows the velocities at the rotor plane. The inflow angle ϕ is calculated according to Equation 2-1;

$$\phi(i) = atan\frac{(1-a(i))\cdot V_\infty}{(1+a_t(i))\cdot\omega\cdot r(i)} \qquad \text{Equation 2-1}$$

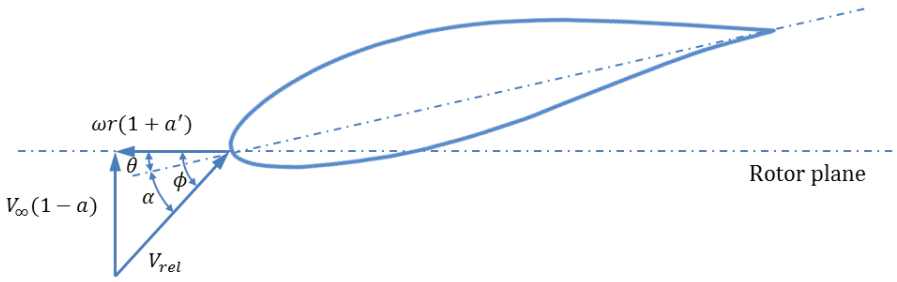

Figure 2-4: Velocities at the rotor plane

Step 3

The angle of attack $\alpha(i)$ is the result of the inflow angle $\phi(i)$ and the pitch angle $\theta(i)$ of the blade element. The pitch angle of a blade element is a combination of the pitch angle of the turbine blade $\beta(j)$ and the twist of the blade element $\gamma(i)$. This is illustrated in Figure 2-4 and given by Equation 2-2 and Equation 2-3;

$$\theta(i) = \beta(j) + \gamma(i) \qquad \text{Equation 2-2}$$

$$\alpha(i) = \phi(i) - \theta(i) \qquad \text{Equation 2-3}$$

Step 4

The local angle of attack is used to generate a lift- and drag coefficient, $C_l(i)$ and $C_d(i)$, for each element from the lookup tables. The generation of these lookup tables is discussed in Chapter 2.3.

Step 5

C_n and C_t are the force components normal and tangential to the rotor plane. The force coefficient normal to the rotor plane is of particular interest because this force is of big influence on the platform motion behaviour when a unidirectional environment, current and waves, is considered. Figure 2-5 shows the local loads on a blade element.

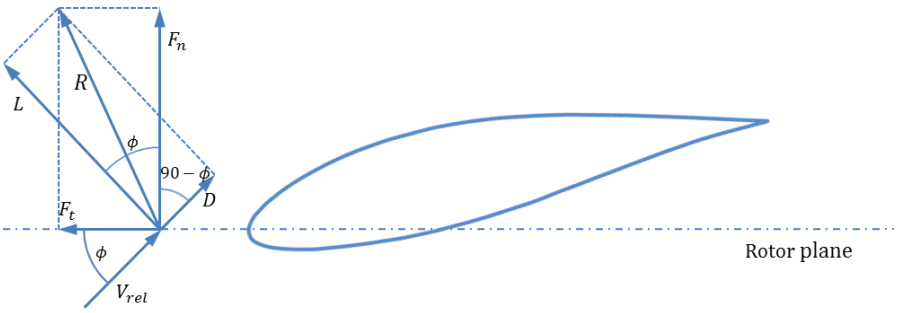

Figure 2-5: The local loads on a blade

The lift and drag on a blade element are calculated according to Equation 2-4 and Equation 2-5;

$$L(i) = \frac{1}{2} \cdot \rho \cdot V_{rel}^2(i) \cdot c(i) \cdot C_l(i) \qquad \text{Equation 2-4}$$

$$D(i) = \frac{1}{2} \cdot \rho \cdot V_{rel}^2(i) \cdot c(i) \cdot C_d(i) \qquad \text{Equation 2-5}$$

The force in normal- and tangential direction follows directly from Figure 2-5 and are given by Equation 2-6 and Equation 2-7;

$$F_n(i) = L(i) \cdot \cos\phi(i) + D(i) \cdot \sin\phi(i) \qquad \text{Equation 2-6}$$

$$F_t(i) = L(i) \cdot \sin\phi(i) - D(i) \cdot \cos\phi(i) \qquad \text{Equation 2-7}$$

The coefficients are easily obtained by making Equation 2-6 and Equation 2-7 dimensionless or replacing $L(i)$ and $D(i)$ by $C_l(i)$ and $C_d(i)$ respectively. The force coefficient in normal- and tangential direction then become;

$$C_n(i) = C_l(i) \cdot \cos\phi(i) + C_d(i) \cdot \sin\phi(i) \qquad \text{Equation 2-8}$$

$$C_t(i) = C_l(i) \cdot \sin\phi(i) - C_d(i) \cdot \cos\phi(i) \qquad \text{Equation 2-9}$$

Step 6

An expression for the axial- and tangential induction factor is found as function of the inflow angle, blade solidity and the normal- and tangential force coefficient;

$$a(i) = \frac{1}{\frac{4 \cdot sin^2\phi(i)}{\sigma(i) \cdot C_n(i)} + 1} \qquad \text{Equation 2-10}$$

$$a_t(i) = \frac{1}{\frac{4 \cdot sin\phi(i) \cdot cos\phi(i)}{\sigma(i) \cdot C_t(i)} - 1} \qquad \text{Equation 2-11}$$

Step 7

N_i is the total number of iterations that are performed to find the converged values of a and a_t. The iteration loop is illustrated in Figure 2-10. Once the axial- and tangential induction factors are converged, the converged values for the other parameters are known too. These are used in the final step in the BEM theory to calculate the local loads on segments of the blades and analyse the turbine performance.

Step 8

The local loads on the blade elements are the thrust and torque. Also the delivered power can be calculated. Form the normal force coefficient the load in x-direction can be calculated. Summation of the ring elements gives the total load on the rotor.

The thrust (dT), torque (dQ) and power (dP) for one ring element (i) are determined based on the normal- and tangential force coefficient;

$$dT(i) = \sigma(i) \cdot \pi \cdot \rho \cdot V_{rel}^2(i) \cdot C_n(i) \cdot r(i) \cdot dr(i) \quad \text{Equation 2-12}$$

$$dQ(i) = \sigma(i) \cdot \pi \cdot \rho \cdot V_{rel}^2(i) \cdot C_t(i) \cdot r^2(i) \cdot dr(i) \quad \text{Equation 2-13}$$

$$dP(i) = \omega \cdot dQ(i) \quad \text{Equation 2-14}$$

The force in x-direction (F_x) is directly related to the normal force coefficient;

$$dF_x(i) = \frac{1}{2} \cdot \rho \cdot V_{rel}^2(i) \cdot A(i) \cdot C_n(i) \quad \text{Equation 2-15}$$

The total force in x-direction, the thrust (T), torque (Q) and power (P) are obtained by summation over the ring elements; see Equation 2-16 till Equation 2-19.

$$F_x = \sum_{N_s} dF_x \quad \text{Equation 2-16}$$

$$T = \sum_{N_s} dT \quad \text{Equation 2-17}$$

$$Q = \sum_{N_s} dQ \quad \text{Equation 2-18}$$

$$P = \sum_{N_s} dP \quad \text{Equation 2-19}$$

The power- and thrust coefficient are obtained by making Equation 2-19 and Equation 2-17 dimensionless;

$$C_p = \frac{P}{\frac{1}{2} \cdot \rho \cdot V_\infty^3 \cdot A_{rotor}} \quad \text{Equation 2-20}$$

$$C_t = \frac{T}{\frac{1}{2} \cdot \rho \cdot V_\infty^2 \cdot A_{rotor}}$$ Equation 2-21

2.2 Tip loss correction model

Blade element momentum theory assumes that there is no flow along the span of the blade, the flow is considered to be 2-D along the chord. In reality, a flow along the span is caused by the pressure difference between the pressure and suction sides of the blade. This span wise flow results in a vortex at the tip of the blade.

The vortex negatively affects the aerodynamic efficiency near the tip. It will reduce the lift and therefore the torque, ultimately reducing the power production. Prandtl (3) (4) developed an approach for correcting the tip-loss using a factor F_{tip} that corrects the aerodynamic force components. Glauert (3) (4) implemented this correction in the momentum equations of BEMT to give the updated axial and tangential induction factor. A more elaborate description on the tip loss correction factor is given in the definition study of this thesis (2).

Glauert derives the following expression for the tip loss factor;

$$F_{tip} = \frac{2}{\pi} cos^{-1}(e^{-f})$$ Equation 2-22

In which:

$$f = \frac{N_b}{2} \frac{R - r}{r sin\phi}$$ Equation 2-23

Figure 2-6 shows the value of the tip loss correction factor along the span for a constant 10° inflow angle. For this specific case it is observed that the aerodynamic force components of the outer 28% of the span of the blade are corrected by the tip loss factor. Closer to the hub, the correction doesn't affect the aerodynamic forces. This distribution changes for different inflow angles, as shown in the figure by the red and green lines.

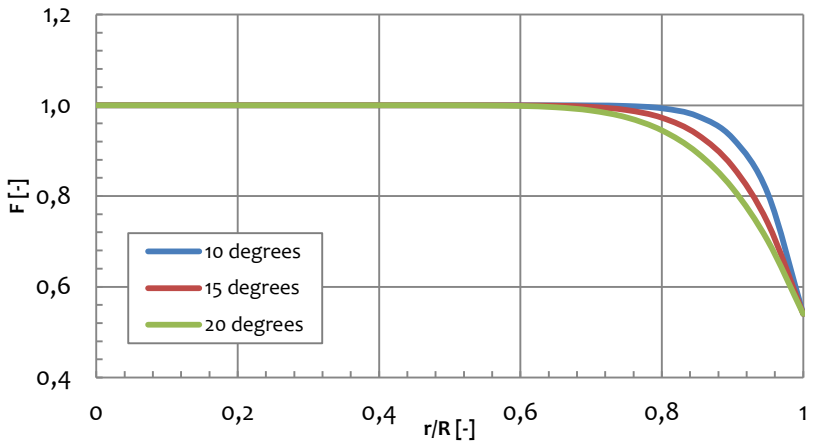

Figure 2-6: Tip-loss factor for a 3-bladed turbine with constant 10°, 15° and 20° inflow angle given along the non-dimensionless radius

Implementing of the tip loss in BEMT

The tip loss factor is implemented in step 6 of the BEM theory. Equation 2-10 and Equation 2-11 are adjusted and change into;

$$a(i) = \frac{1}{\frac{4 \cdot F_{tip}(i) \cdot sin^2\phi(i)}{\sigma(i) \cdot C_n(i)} + 1} \qquad \text{Equation 2-24}$$

$$a_t(i) = \frac{1}{\frac{4 \cdot F_{tip}(i) \cdot \sin\phi(i) \cdot \cos\phi(i)}{\sigma(i) \cdot C_t(i)} - 1} \qquad \text{Equation 2-25}$$

The tip loss factor also alters the calculation of the local loads on the blade segments. Equation 2-12 and Equation 2-13 change into;

$$dT(i) = F_{tip} \cdot \sigma(i) \cdot \pi \cdot \rho \cdot V_{rel}^2(i) \cdot C_n(i) \cdot r(i) \cdot dr(i) \qquad \text{Equation 2-26}$$

$$dQ(i) = F_{tip} \cdot \sigma(i) \cdot \pi \cdot \rho \cdot V_{rel}^2(i) \cdot C_t(i) \cdot r^2(i) \cdot dr(i) \qquad \text{Equation 2-27}$$

2.3 2-D Lift- & drag characteristics

In the BEM theory each element is considered as a 2-D hydrofoil. For calculating the lift- and drag, normal- and tangential forces acting on each element, the lift- and drag coefficients are needed. The 2-D characteristics have been obtained by XFOIL (5). XFOIL is capable to provide lift- and drag characteristics for a limited range of inflow angles, up until the stall angle of the foil. During the iteration process of the axial- and tangential induction factor however angles of attack above this stall angle will occur. Therefore the lift- and drag characteristics for a larger range of α are needed. A method described by Viterna (6) is used to extrapolate the data obtained by XFOIL to a full range of angles of attack.

Table 1 shows the geometry of a turbine blade. This shows the dimensions of the rotor blades on full scale, obtained from the model that has been used during model tests. The geometry is provided by IFREMER. The blades are composed of NACA 63-4xx profiles and are divided in 20 elements all which can be represented by a 2-D airfoil with a certain twist (γ), chord (c) and thickness over chord ratio (t/c). 'xx' in the profile-id represents the thickness ratio of the element. This geometry serves as input for the generation of the 2-D lift- and drag characteristics, as will be discussed in Chapter 2.3.1.

Element, i	Radius, r (m)	Twist, γ (deg)	Chord, c (m)	Thickness ratio, t/c (-)	Profile
1	1,7354	25,6273	1,3305	0,36	NACA 63-436
2	2,1146	22,1491	2,1652	0,21	NACA 63-421
3	2,4938	19,3031	2,0784	0,21	NACA 63-421
4	2,8729	16,9737	1,9767	0,22	NACA 63-422
5	3,2521	15,0538	1,8736	0,22	NACA 63-422
6	3,6313	13,4572	1,7753	0,22	NACA 63-422
7	4,0104	12,1169	1,6841	0,22	NACA 63-422

8	4,3896	10,9815	1,6008	0,23	NACA 63-423
9	4,7688	10,0114	1,5251	0,23	NACA 63-423
10	5,1479	9,1761	1,4566	0,22	NACA 63-422
11	5,5271	8,4516	1,3945	0,22	NACA 63-422
12	5,9063	7,8191	1,3383	0,22	NACA 63-422
13	6,2854	7,2638	1,2872	0,21	NACA 63-421
14	6,6646	6,7735	1,2407	0,21	NACA 63-421
15	7,0438	6,3387	1,1983	0,20	NACA 63-420
16	7,4229	5,9514	1,1595	0,19	NACA 63-419
17	7,8021	5,6050	1,1240	0,19	NACA 63-419
18	8,1813	5,2941	1,0913	0,18	NACA 63-418
19	8,5604	5,0143	1,0612	0,18	NACA 63-418
20	8,7500	4,8743	0,5731	0,25	NACA 63-425

Table 1: Geometry of the full scale turbine blade, given per element

2.3.1 XFOIL

The 2-D panel code XFOIL (5) is used to derive the lift- and drag coefficients data for the blade elements.

Reynolds number

In order to validate numerical results with measurement data from basin tests (Appendix A), the 2-D lift- and drag characteristics are generated for a Reynolds number that is based on the radius (R) of the turbine on model scale, see Equation 2-28;

$$Re = \frac{R \cdot U_c}{\nu} \qquad \text{Equation 2-28}$$

For further simulations and analysis, a Reynolds number of approximately 580.000 is assumed (7).

Figure 2-7 shows the lift- and drag characteristics obtained from XFOIL for the angles of attack between -9° and 20°. The lift coefficients show a linear behaviour for small angles of attack until the maximum value is obtained. The angle of attack which corresponds to the maximum lift coefficient is the stall angle (α_{stall}). Beyond this angle, the post-stall region starts. XFOIL is capable of generating the lift- and drag characteristics for only the first part of this post-stall region. This is indicated more clearly by the lift characteristics for profiles with a lower t/c ratio, XFOIL can generate the lift- and drag characteristics only up until a specific angle of attack.

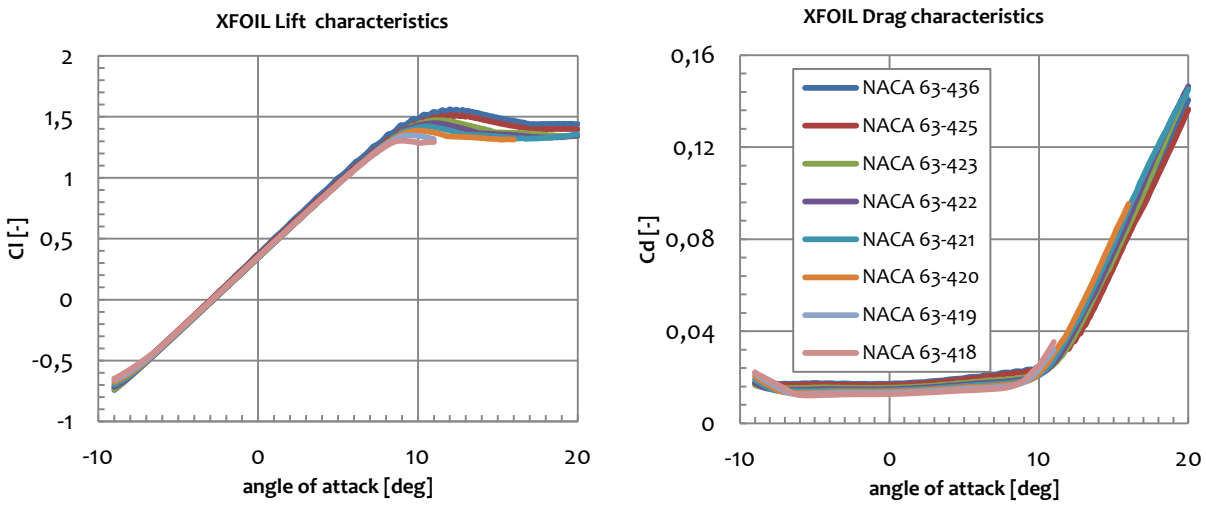

Figure 2-7: Results obtained from XFOIL for the 2-D lift- and drag characteristics

2.3.2 Post-stall C_l and C_d

XFOIL gives lift- and drag characteristics in the range of -10° to approximately 20°. A method proposed by Viterna (6) is used to extrapolate these curves to the range of 90 degrees. The Viterna method is used for predicting post-stall airfoil characteristics. The original Viterna equations are shown below and are based on airfoil characteristics in the laminar range.

First step by applying the Viterna equations is finding the stall angle. The stall angle corresponds to the associated (maximum) lift coefficient ($C_{l_{max}}$) and drag coefficient ($C_{d_{stall}}$). Combined with the aspect ratio (AR) of the specific blade element the lift- and drag characteristics for $\alpha_{stall} < \alpha \leq 90^o$ are determined by Equation 2-29 to Equation 2-35.

$$C_{d_{max}} = 1.11 + 0.018 \cdot AR \qquad (\alpha = 90^o) \qquad \text{Equation 2-29}$$

$$C_d = B_1 \sin^2 \alpha + B_2 \cos \alpha \qquad (\alpha = \alpha_{stall} \; to \; 90^o) \qquad \text{Equation 2-30}$$

In which:

$$B_1 = C_{d_{max}} \qquad \text{Equation 2-31}$$

$$B_2 = \frac{C_{d_{stall}} - C_{d_{max}} \sin^2 \alpha_{stall}}{\cos \alpha_{stall}} \qquad \text{Equation 2-32}$$

The lift coefficients follow from;

$$C_l = A_1 \sin 2\alpha + A_2 \frac{\cos^2 \alpha}{\sin \alpha} \qquad (\alpha = \alpha_{stall} \; to \; 90^o) \qquad \text{Equation 2-33}$$

In which:

$$A_1 = B_1/2 \qquad \text{Equation 2-34}$$

$$A_2 = \left(C_{l_{max}} - C_{d_{max}} \sin \alpha_{stall} \cos \alpha_{stall}\right) \frac{\sin \alpha_{stall}}{\cos^2 \alpha_{stall}} \qquad \text{Equation 2-35}$$

Figure 2-8 shows the lift- and drag characteristics after the Viterna method is applied to the XFOIl data. Comparing these graphs to the graphs shown in Figure 2-7 clearly indicates that the characteristics are determined by Viterna's equations starting from the stall angle.

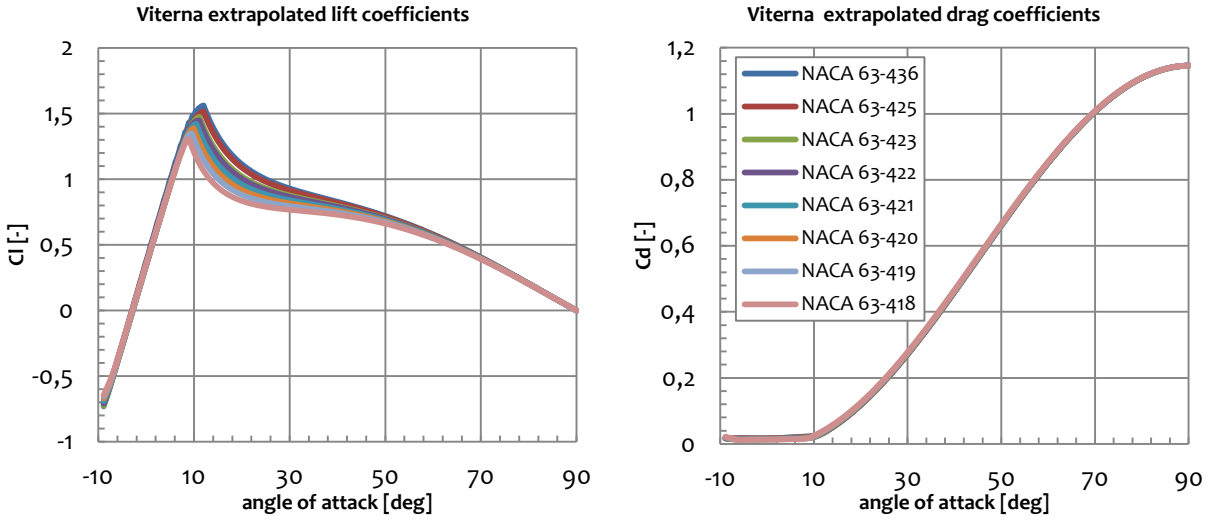

Figure 2-8: Extrapolated lift- and drag characteristics after applying the Viterna-correction of the XFOIL data

2.4 Calculation method

The BEM theory is solved in a numerical model to analyse the turbine performance. Figure 2-9 gives a schematic overview of the numerical model. The "block" BEM theory is explained by a different schematic overview, illustrated by Figure 2-10. The "2-D section data" are the lift- and drag characteristics discussed in the previous paragraphs. A linear interpolation function is used to find the appropriate lift- and drag coefficient for the angle of attack on each segment.

The output of the model is the power- and thrust coefficients (C_p and C_t), given as function of the tip speed ratio (TSR) of the turbine. The BEM theory is applied in a loop for a range of tip speed ratios. The power- and thrust coefficients are used in Chapter 3 for the verification and validation of the steady BEM model.

The numerical model can be used to generate lookup tables for the force coefficient in normal direction $C_n(i)$ as function of the local tip speed ratio (TSR_{local}). These lookup tables will serve as input for the unsteady model, which will be the topic of Chapter 4 and Chapter 5 of this thesis.

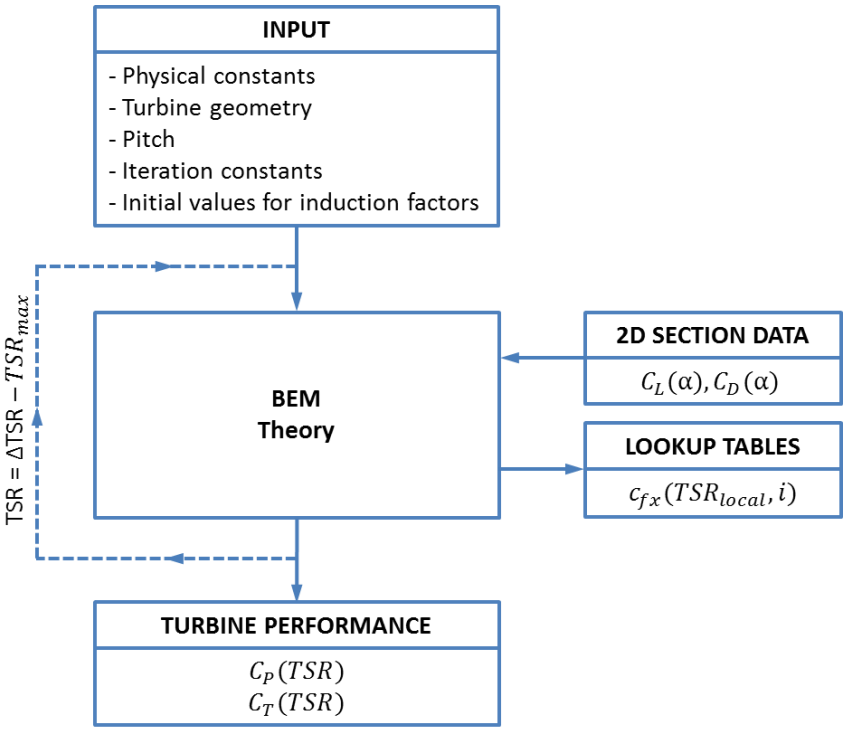

Figure 2-9: Schematic overview of the numerical model

Figure 2-10 gives a detailed view of the numerical implementation of the BEM theory. It shows that the complete numerical model consists of three loops; one for the tip speed ratio (TSR), one for each ring element (i) and finally an iteration loop for the convergence of the axial- and tangential induction factors.

In this iteration loop, the steps described in Chapter 2.1 are taken. The lookup tables for the lift- and drag coefficients serve as input for this loop, as well as the tip loss correction factor described in Chapter 2.2.

The number of iterations (N_i) is set equal to 50. This showed to serve as a realistic value, leading to converged values for the axial- and tangential induction factor. This will be illustrated in Chapter 3.

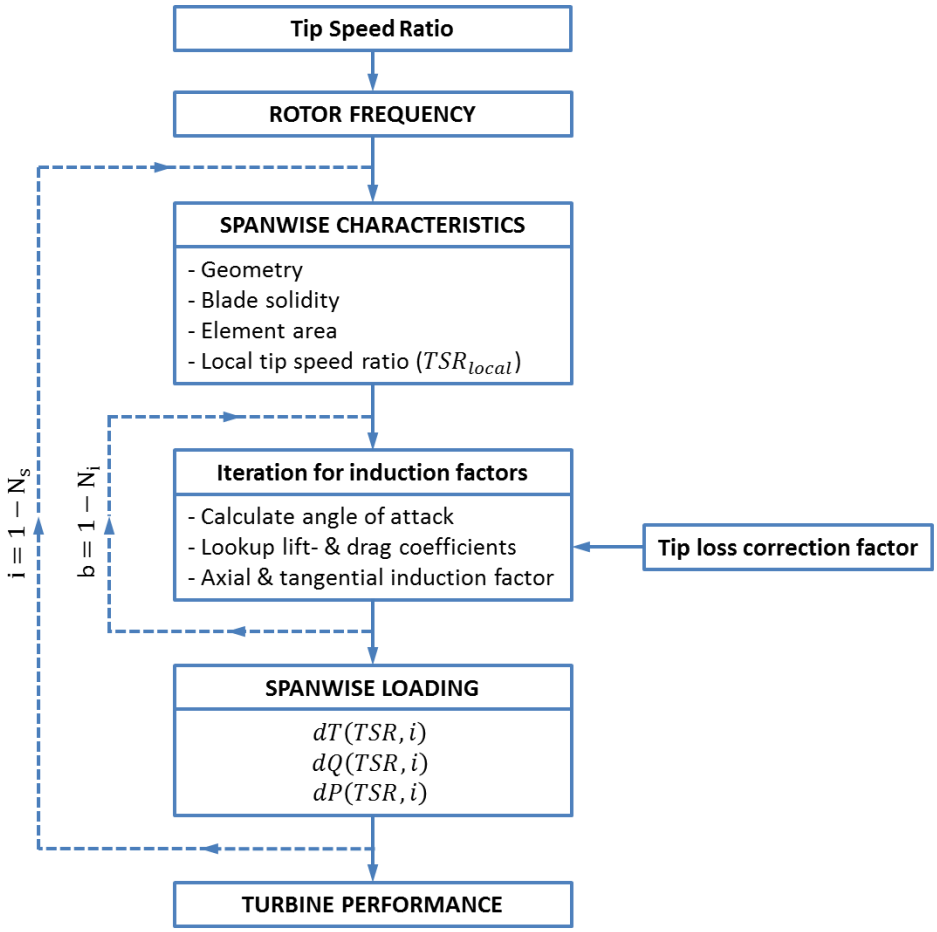

Figure 2-10: Schematic overview of the BEM model

3 Verification & validation of the steady model

A verification & validation study for the numerical model is performed by means of a comparison with data available from literature and model tests. In this chapter the numerical model is verified by a comparison with the academic in-house code SERG - Tidal (8) *and the commercial code GH – Tidal Bladed*[1]*, a validation study is done by a comparison of the numerical model with experimental data presented by Bahaj* (8) *and results obtained from model tests that have been performed by Bluewater with the BlueTEC platform* (9)*.*

Bahaj (8) *has published the results of the development and validation of an academic in-house code and this delivers a very good starting point for the verification and validation of the numerical model with respect to power- and thrust coefficient curves for different pitch angles, these results are discussed in Chapter 3.1. Batten* (10) *continues on this study by also presenting span-wise characteristics of inflow angle, power coefficient and axial and tangential induction factors. The results of the comparison between the numerical model and the results presented in the paper of Batten are presented in Chapter 3.2. Chapter 0 validates the numerical model against experimental data obtained from tests with a model of the BlueTEC platform.*

3.1 Power and thrust curves

The study of Bahaj reports on the development and verification of simulation tools based on blade element momentum theory, a commercial code (GH – Tidal Bladed) and an academic in-house code (SERG – Tidal) (8). Validation of their numerical results is derived from experimental measurements conducted on an 800 mm diameter turbine in a cavitation tunnel and a towing tank. The experimental data includes measurements of shaft power and thrust generated by the turbine for a series of blade pitch settings and speeds.

SERG – Tidal is a relatively simple model, based on the BEM theory and with the introduction of a tip loss factor. GH – Tidal Bladed is a commercial design tool and offers more options with respect to structural design, flow modelling and lay-out. The BEM models used within the papers do not model boundary effects of the seabed and the free surface. The results obtained from the cavitation tunnel and towing tank have been corrected for tunnel blockage in order to present the results for free stream conditions.

3.1.1 2-D characteristics

The same blade geometry as used by Bahaj served as input for the numerical model described in Chapter 2. The 2-D lift and drag coefficient data for the blade elements were derived using performance code XFOIL, as has been described in Chapter 2.3. A Reynolds number of 580.000 is assumed based on the rotor radius, to generate the lift and drag characteristics.

Figure 3-1 shows the comparison between the coefficients used by Bahaj (dotted lines) and in the BEM model (solid lines); only the results for NACA 63-815 and NACA 63-824 are presented here. The drag coefficients show a very good agreement for the range showed. The lift coefficients used by the BEM model show an earlier drop near the stall angle of the foil. This drop is the result of the Viterna extrapolation discussed in Chapter 2.3. Another reason could be that Bahaj used a different Reynolds number for the generation of the lift and drag characteristics. The influence of Reynolds number on the lift and drag coefficients will be discussed later in this report.

[1] www.gl-garradhassan.com

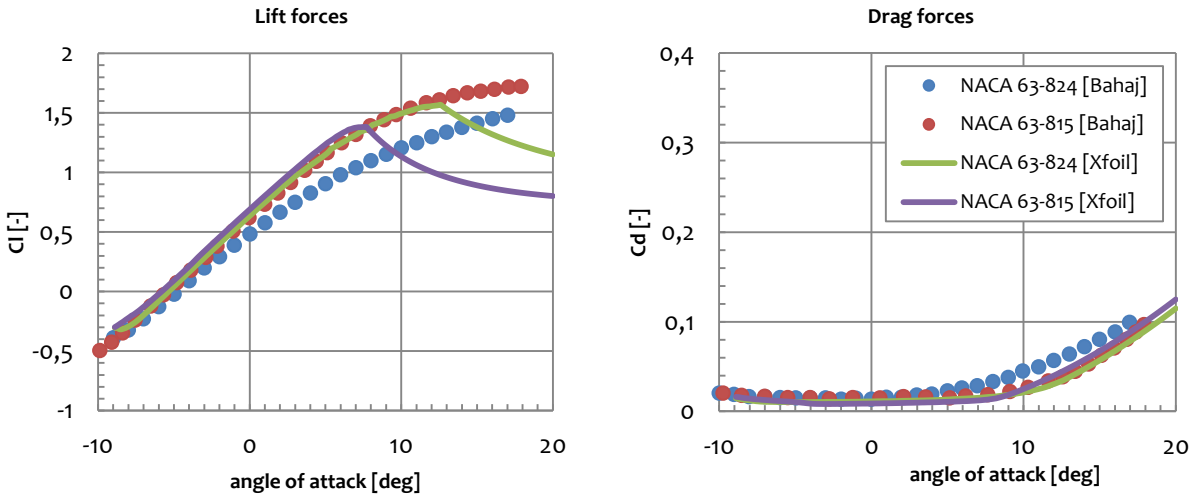

Figure 3-1: Comparisons between 2-D Lift and drag coefficient used by Bahaj and the BEM model

3.1.2 Performance comparison between experiments and theory

Bahaj presents the results of two numerical codes and the data sets of two experimental tests. Combined with the developed BEM model, this gives two numerical codes to act as verification and two data sets to act as a validation. Experiments have been done for set pitch angles of 0°, 5°, 10° and 13° and are shown in power- and thrust coefficients for a range of tip speed ratio's (TSR). The design pitch angle of the rotor is 5°.

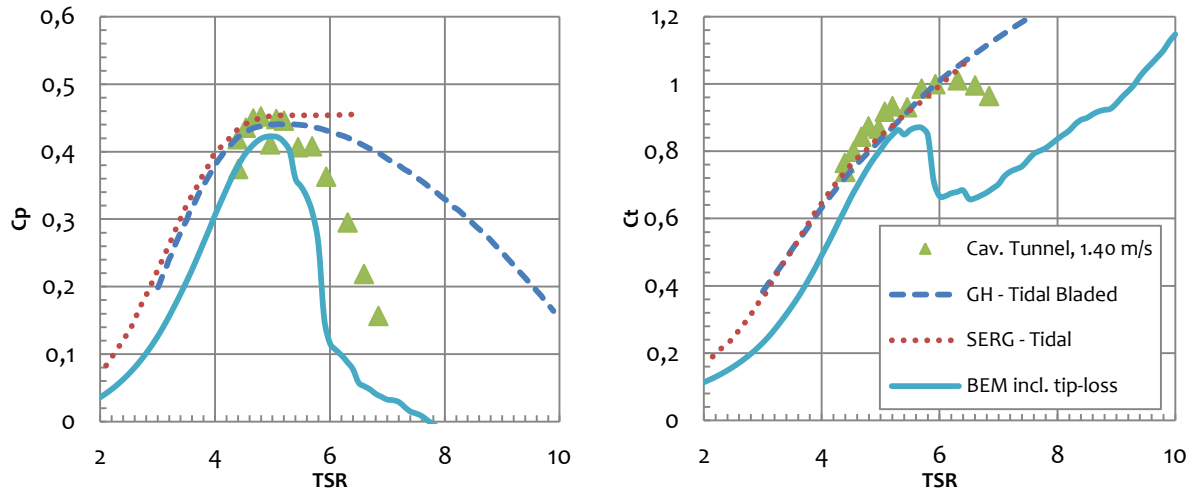

Figure 3-2: Comparisons between experiments and simulations with a 0° set angle

Figure 3-2 shows the first comparison for a set pitch angle of 0°. It clearly shows that the numerical model follows the other models quite well, although the power and thrust coefficient are slightly underestimated for the TSR in range 2-5. What stands out most in the graphs is the immense drop of the power and thrust coefficient around TSR = 5 and the unexpected development for higher values of TSR.

An explanation for this sudden drop is illustrated by the graphs shown in Figure 3-3. Here, the convergence of the axial induction factor is shown for a 0° set angle and different values of TSR. The graph top left shows the convergence of the axial induction factor for TSR = 4, the values of the induction factor are

below 0.5 and the turbine operates in its windmill state where the momentum theory is valid. From TSR = 5 and above it can be seen in the top right and bottom graph that more and more blade sections experience an axial induction factor higher than 0.5 and this indicates the turbine operates in its turbulent wake state. Because a wake correction model is not applied the BEM model is not able to take into account these effects.

The experimental data from the cavitation tunnel do however show a similar drop in power coefficient around TSR = 5 and for the thrust coefficient around TSR = 6. GH – Tidal Bladed and SERG – Tidal both fail to predict this sharp drop. Although wake correction models are applied in these numerical models the sharp drop in the curves is likely caused by stall effects of the hydrofoil which are not taken into account in the numerical modelling of the turbine.

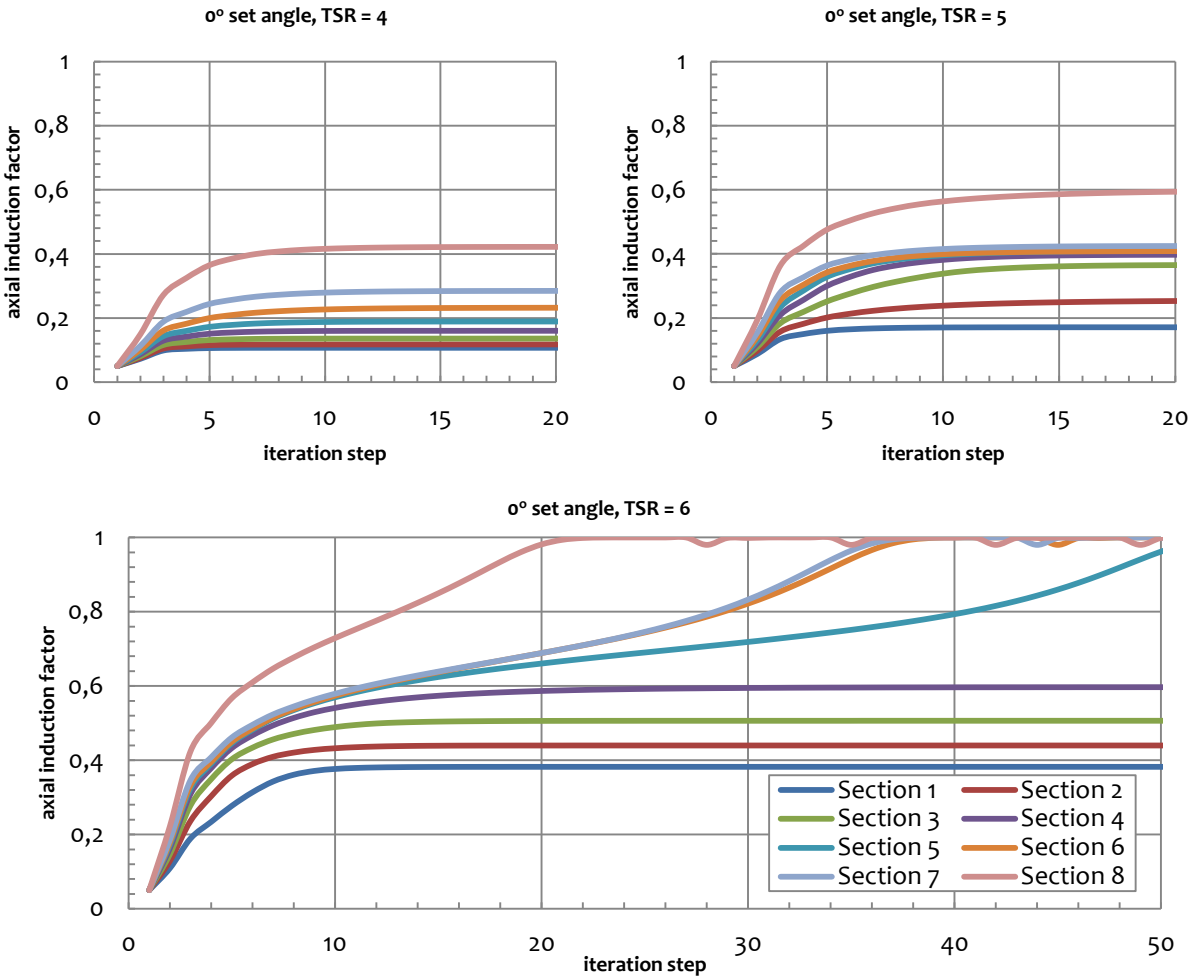

Figure 3-3: Convergence of the axial induction factor for the 0° set angle case, for different values of the tip speed ratio (TSR = 4, top left; TSR = 5, top right; TSR = 6, bottom)

Figure 3-4 shows the results for the design case, a 5° set angle. It show that all numerical models and experimental data show quite good agreement, especially in the range of TSR between 5 and 6. The better performance of the relatively simple BEM model can be explained if Figure 3-5 is considered. This shows that the converged values of the axial induction stay below 0.5 which indicates a wake correction model is not necessary, even for higher values of TSR = 7.

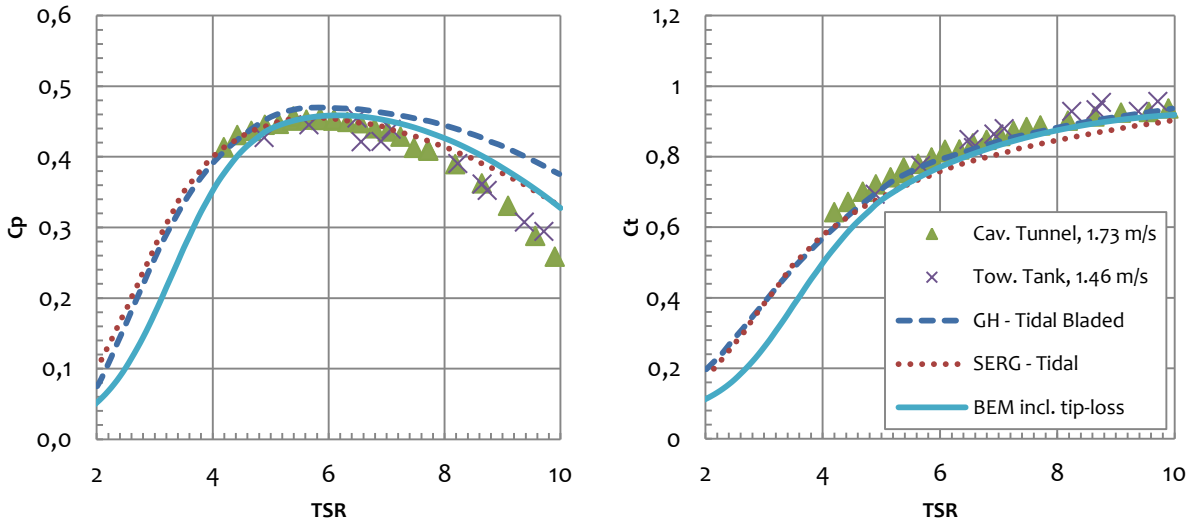

Figure 3-4: Comparisons between experiments and simulations with 5° set angle (the design case)

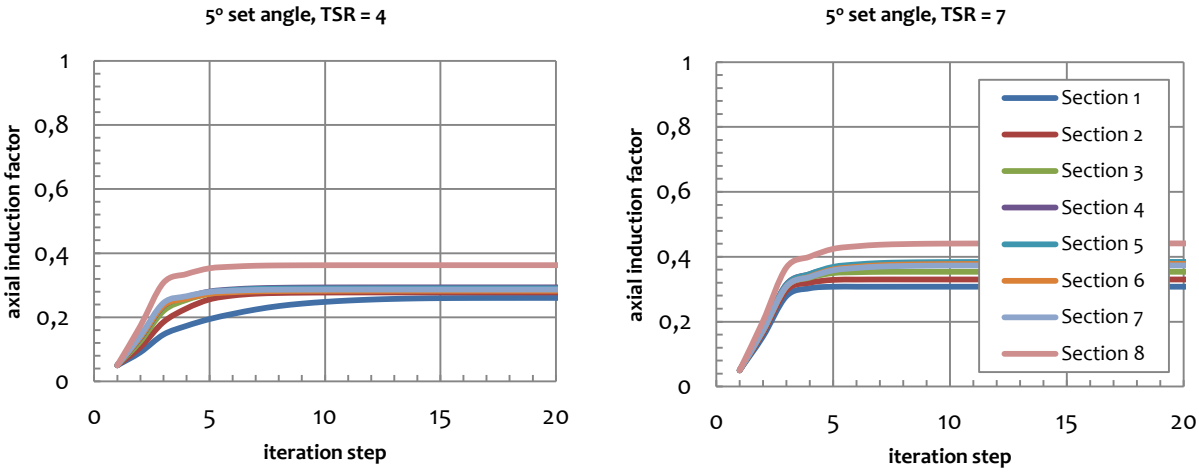

Figure 3-5: Convergence of the axial induction factor for the 5° set angle case, for different values of the tip speed ratio (TSR = 4, left; TSR = 7, right)

Figure 3-6 and Figure 3-7 show the curves for the 10° and 13° set angle. The BEM model shows similar trends as the other numerical models although the predicted values are a little bit lower. The fit with the experimental data seems quite good; the thrust seems to be underestimated a little bit more than the power.

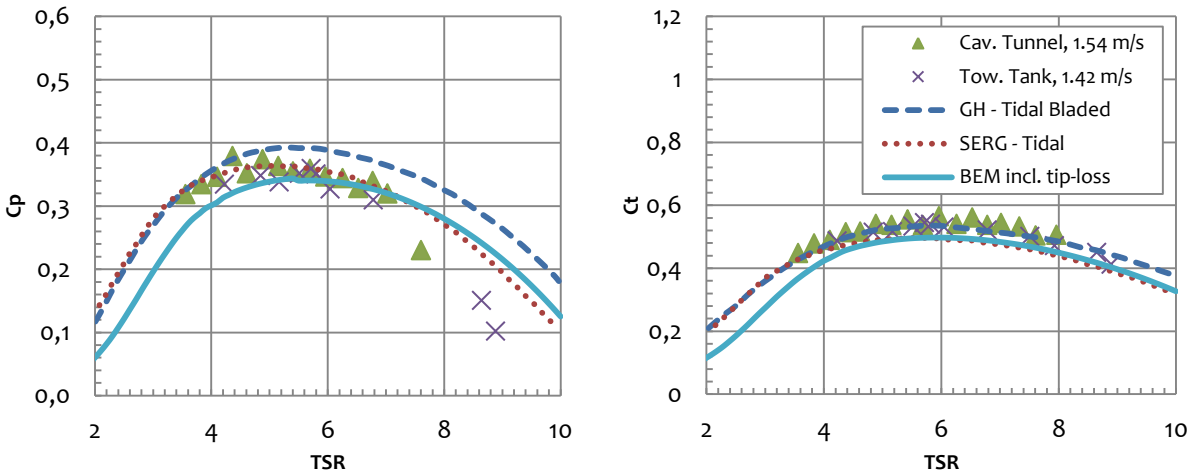

Figure 3-6: Comparisons between experiments and simulations with 10° set angle

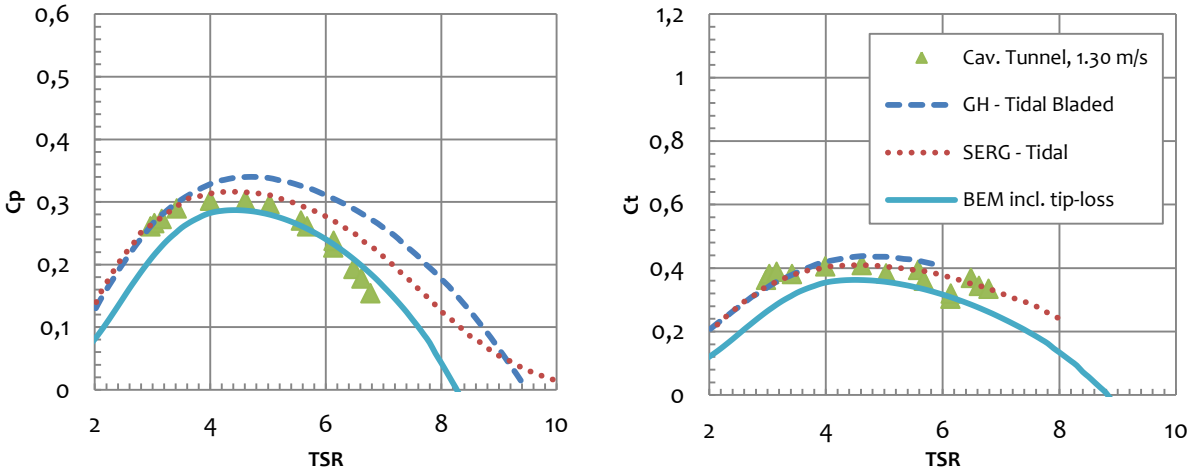

Figure 3-7: Comparisons between experiments and simulations with 13° set angle

Example predictions for a 20 m rotor operating in a tidal stream of 2.5 m/s for the 5° set angle are presented in Table 2. These results show that very good agreement for the power is found around TSR = 6. All numerical models seem to overestimate the power and underestimate the thrust for TSR > 6 in comparison to the experimental data. Either reason may be, due to errors in the large blockage corrections applied to the numerical data or possible different turbulent wake models used.

	Power (MW)			Thrust (kN)		
TSR	4	6	8	4	6	8
Cavitation tunnel	1	1,13	0,99	625	814	901
Towing tank	1	1,13	1,01	598	818	931
SERG - Tidal	1,01	1,14	1,04	584	765	853
GH - Tidal Bladed	0,99	1,18	1,11	571	791	888
BEM - incl. tip loss	0,89	1,15	1,07	502	775	880

Table 2: Comparison of predicted powers and thrusts with a set angle of 5° from spline fits for a 20 m diameter turbine in a 2.5 m/s marine current

3.2 Span-wise characteristics

Batten (10) continues on the paper of Bahaj (8) and uses the same experimental and numerical data as discussed in Chapter 3.1. Batten however presents besides power and thrust coefficient curves more information with respect to the behaviour of the numerical model he used (SERG – Tidal). Figure 3-8 shows the converged span-wise characteristics of the inflow angle, the axial induction factor and the tangential induction factor for two different values of the tip speed ratio.

The values presented by Batten are for a 20° pitch angle while the values for the BEM model shown in the figure below are for the design case, with a set pitch angle of 5°. Therefore, the comparison made in Figure 3-8 is a qualitative one that shows that both numerical models show the same trend in span-wise distribution of the parameters. The higher inflow angles of the BEM model are caused by the lower pitch angle. The axial induction factor shows some different behaviour, especially for the TSR = 4 case. This distribution tends to change for higher pitch angles.

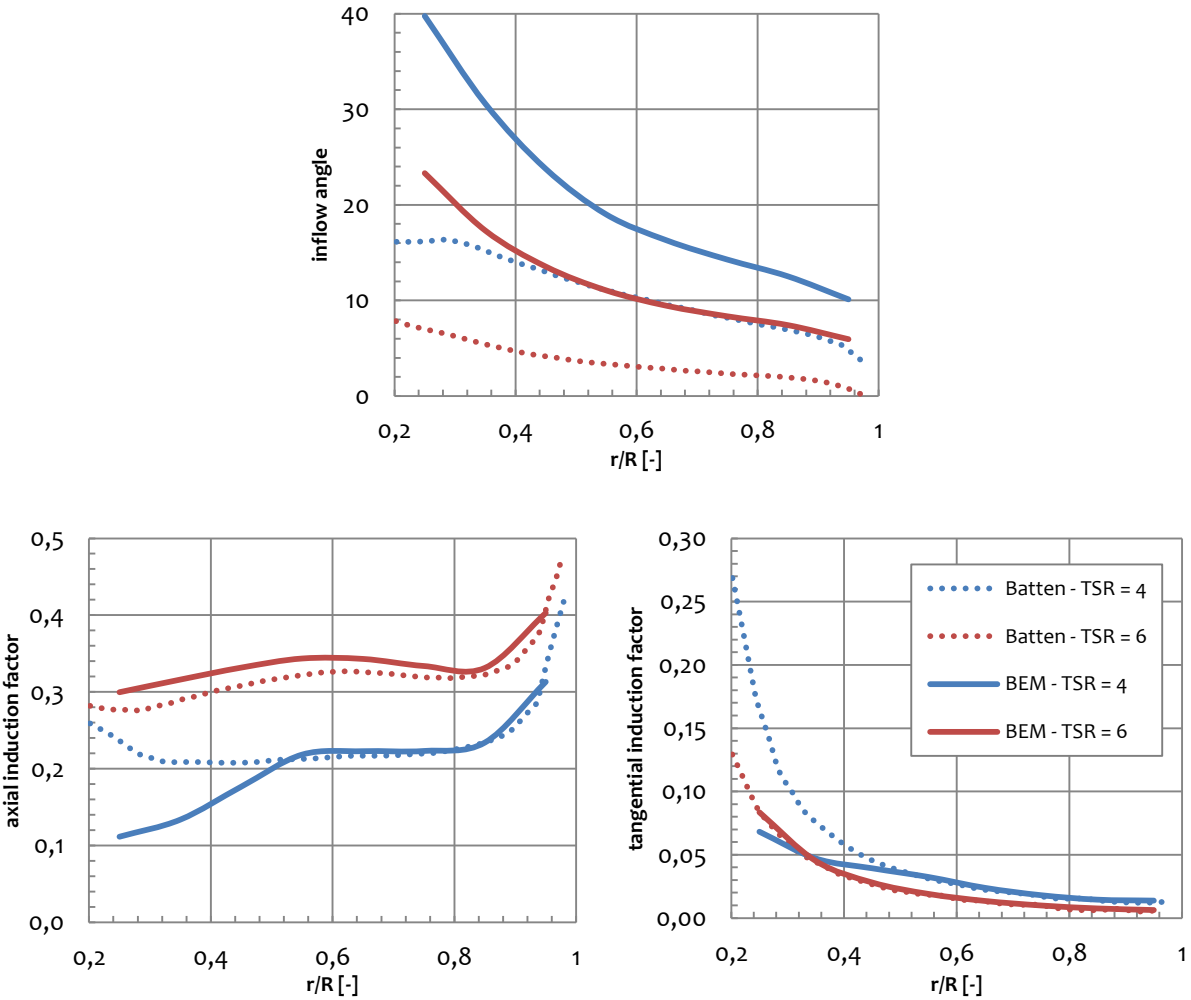

Figure 3-8: Converged values of span-wise characteristics of inflow angle (top), axial induction factor (bottom left) and tangential induction factor (bottom right)

3.3 Experimental data

In January 2013 Bluewater performed extensive model testing on the BlueTEC platform in the circulation tank of IFREMER in Boulogne-sur-Mer (France). Single rotor tests have been performed in current only, and wave-current conditions. The tests are described in detail in an internal technical report of Bluewater (9).

Captive, single rotor tests with current only are observed in this paragraph. This means there are no platform motions, but only current that influences the loading of the turbine. Chapter 3.3.2 analyses the experimental data of the model tests and makes a comparison with the BEM predictions in order to validate the numerical model.

3.3.1 Test set-up

Tests on the BlueTEC platform are performed in two different conditions: a captive and moored platform. During the captive tests the cross beam model was mounted on a load cell fixed to a frame over the tank, simulating static mounted turbines. This set-up is tested for current only and a combination of waves and current. The current only tests are considered in Chapter 3.3.2. The captive tests with combined current and waves will be used in Chapter 5.2 to validate the unsteady flow field simulations. The moored tests are subject in Chapter 5.2, combined with the time domain BEM these are used to analyse the influence of platform motions on the turbine loading.

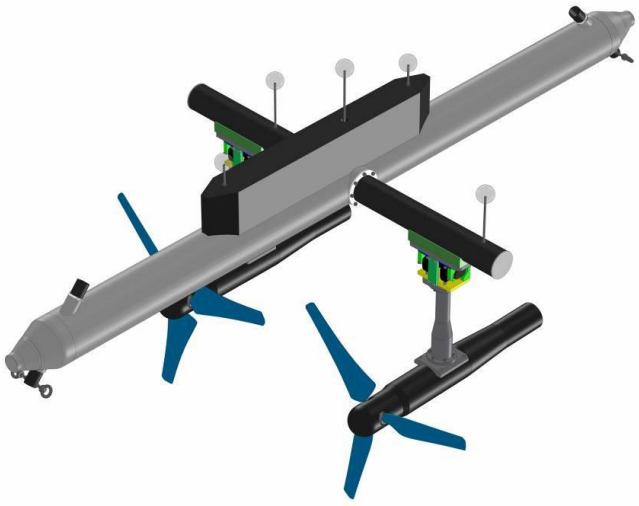

Figure 3-9: 3D-view of the cross beam design

Figure 3-9 shows the 3D – view of the BlueTEC model used in the model tests. A longitudinal main floater is providing buoyancy and supports the cross beam. The cross beam adds stability and forms the connection to the turbines. The turbines are connected to the cross beam by a vertical strut as shown in Figure 3-9 (9). The dimensions of the model are 2.4 meter length by 1.0 meters width approximately. The rotor diameter is 0.70 meter based on the IFREMER-LOMC geometry.

Figure 3-10 shows a schematic 3-D view of the test setup in the circulation tank. The platform is spread moored which are tensioned by springs. The current flow runs from left to right on the figure and a wave maker, positioned upstream of the platform, can generate waves of a set period and amplitude.

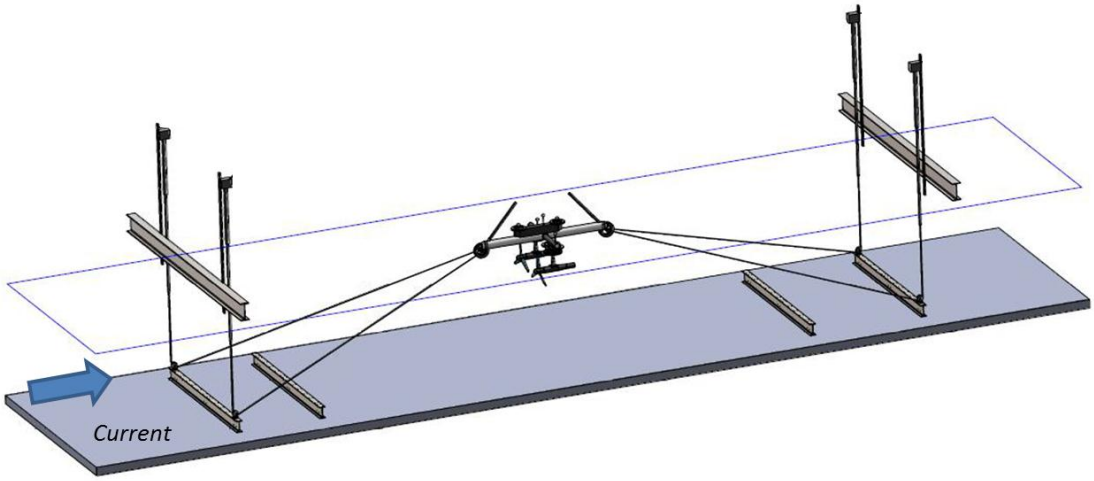

Figure 3-10: Schematic 3D-view of the test setup showing the model and mooring system as positioned in the tank

3.3.2 Validation

Experimental and numerical data is shown in Figure 3-11 till Figure 3-14. They show C_p and C_t curves for different current velocities and different set pitch angles. The BEM predictions are obtained from a very simplified version of the environmental conditions; a uniform current velocity is considered. The differences with the velocity profile in the model tests are quite substantial. The current velocity shear in the circulation tank causes a fluctuating load on each blade and the experimental data is not corrected for blockage. Application of a blockage factor should lower the C_p values a little bit.

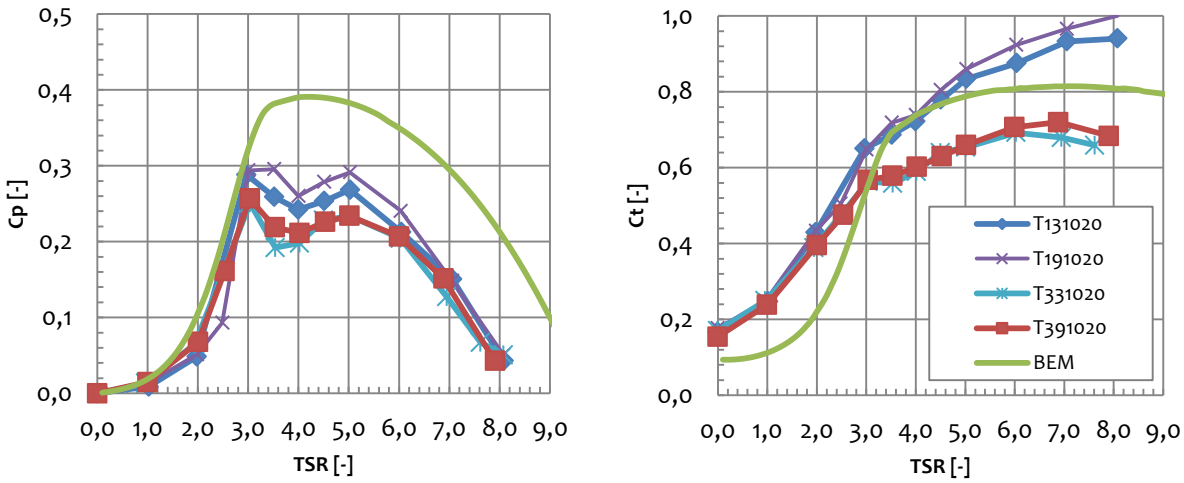

Figure 3-11: Comparison between experimental data and the numerical model for a 0° set pitch angle and free stream current velocity of 2.3 m/s

Figure 3-11 and Figure 3-12 show the results for the 0° set pitch angle (design case) and two different current velocities. The BEM results obviously show the same C_p and C_t curves as results are made dimensionless. The differences between the experimental data sets for the two cases are caused by the design of the turbines blades. The turbine model was initially designed for a current velocity between 0.6 – 1.5 m/s on model scale (9).

The graphs in Figure 3-11 correspond to a velocity on model scale of 0.46 m/s. This explains the differences with the experimental data shown in Figure 3-12 as this velocity lies below the design velocity. At these low velocities, stall of the blades will result in a lower power output. Figure 3-12 shows a very good agreement between experiments and the BEM model. The ascending phase of the C_p curve is predicted exactly by the BEM model and the location of the maximum C_p corresponds very well to the experimental data.

For higher TSR's, larger than 3.5, the BEM model tends to over predict the power coefficients. This is due to higher axial induction factor and the lack of a wake correction model in the numerical model. Furthermore the numerical model represents quite the "ideal world", in which losses and 3-D effects aren't taken into account that do have an effect on the power coefficients obtained from the model tests.

The comparison of thrust coefficients shows a general disagreement between the numerical results and the experimental data. Especially for smaller values of TSR, the numerical model predicts a lower thrust coefficient. This is because the turbine hub is neglected in the numerical model. Introducing a drag correction for the hub and a hub loss correction factor might increase the accuracy of the numerical model here. For higher values of TSR the thrust generation of the blades becomes more dominant and the drag of the hub will have a smaller contribution to the thrust coefficient.

The experimental data shows a clear distinction in the C_t curves. This is caused by the rotors used for the experiments. T131030 and T191030 (the two lines at the top) represent the portside rotors; the small difference in these graphs is caused by the rotational direction of the rotor. T331030 and T391030 (the two lines at the bottom) represent the starboard rotors. The differences between the portside and starboard rotors are likely to be caused by geometry differences.

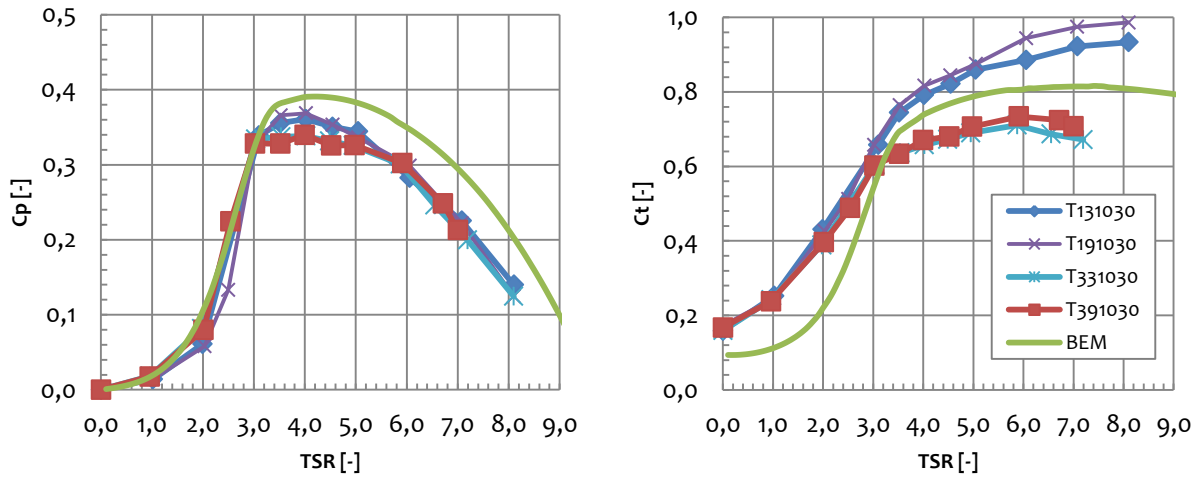

Figure 3-12: Comparison between experimental data and the numerical model for a 0° set pitch angle and free stream current velocity of 3.5 m/s

Figure 3-13 and Figure 3-14 show C_p and C_t curves for higher pitch angles (27° and 15° set pitch angle respectively). These configurations are far from the design case and under these conditions stall of the blades is likely to occur. For the 15° set pitch angle the BEM model is still quite capable of estimating the power coefficients, for the 27° set pitch angle stall is occurring for smaller values of TSR and the numerical BEM model overestimates the power coefficients for this case. In both cases the numerical model does predict the peak of C_p at the same TSR that follows from the model tests.

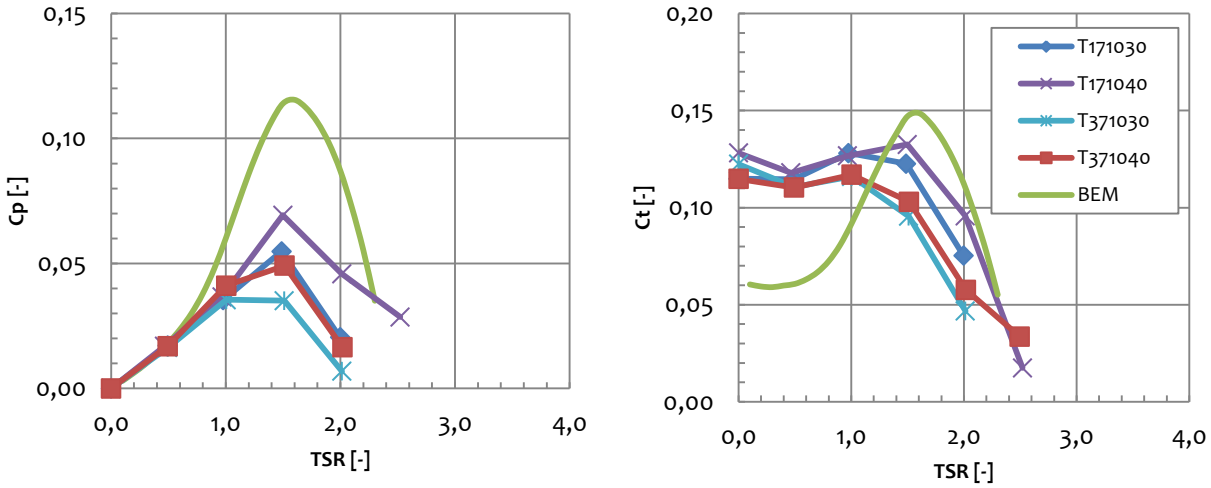

Figure 3-13: Comparison between experimental data and the numerical model for a 27° set pitch angle and free stream current velocity of 3.5 m/s (blue and light blue line) and 5 m/s (purple and red line)

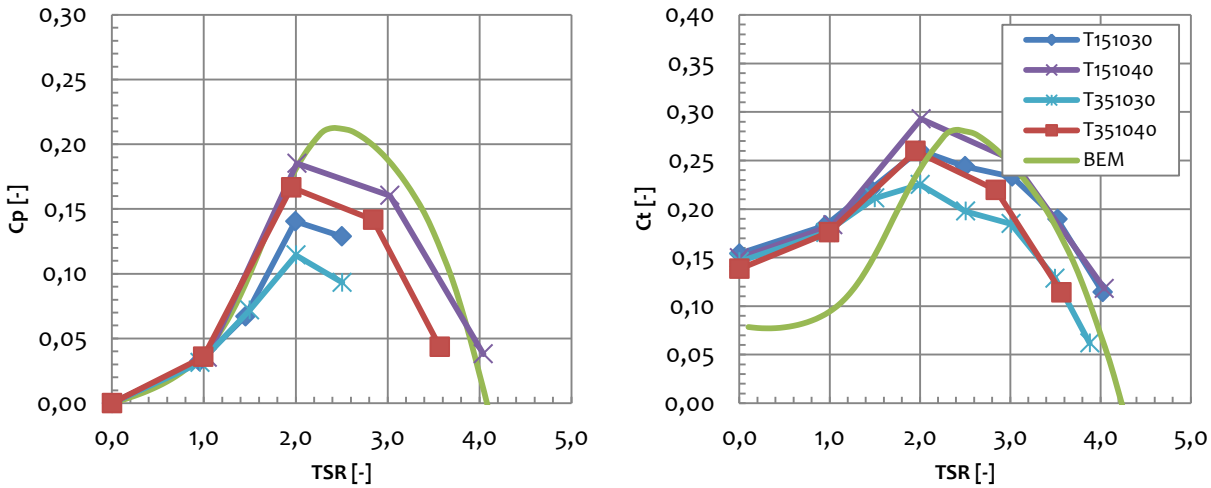

Figure 3-14: Comparison between experimental data and the numerical model for a 15° set pitch angle and free stream current velocity of 3.5 (blue and light blue line) and 5 m/s (purple and red line)

3.4 Discussion

It can be concluded from comparison with both numerical (Chapter 3.1 and 3.2) and experimental data (Chapter 3.3) that a classic BEM model with only a tip loss factor implemented is very good capable of predicting the C_p curves for the *design condition of a turbine*. A slight over prediction of the power coefficient occurs for TSR larger than 4.0.

From the comparison of the single rotor tests in Chapter 3.3 it is shown that the design condition of the 0° set pitch angle and a free stream current velocity of 3.5 m/s delivers the best agreement between numerical and experimental data for a captive, single rotor. To correctly model the configurations with higher pitch angles, additions to the BEM model need to be made.

For the further analysis of the model tests only the 0° set pitch angle with a set current velocity of 3.5 m/s is considered. This implies that lookup tables for the thrust and power coefficients for each segment can be obtained. These lookup tables can be used in the time domain model, which will be described later in Chapter 4, to analyse time series of axial loading and moment around the y-axis of the hub as result of fluctuating relative inflow velocity.

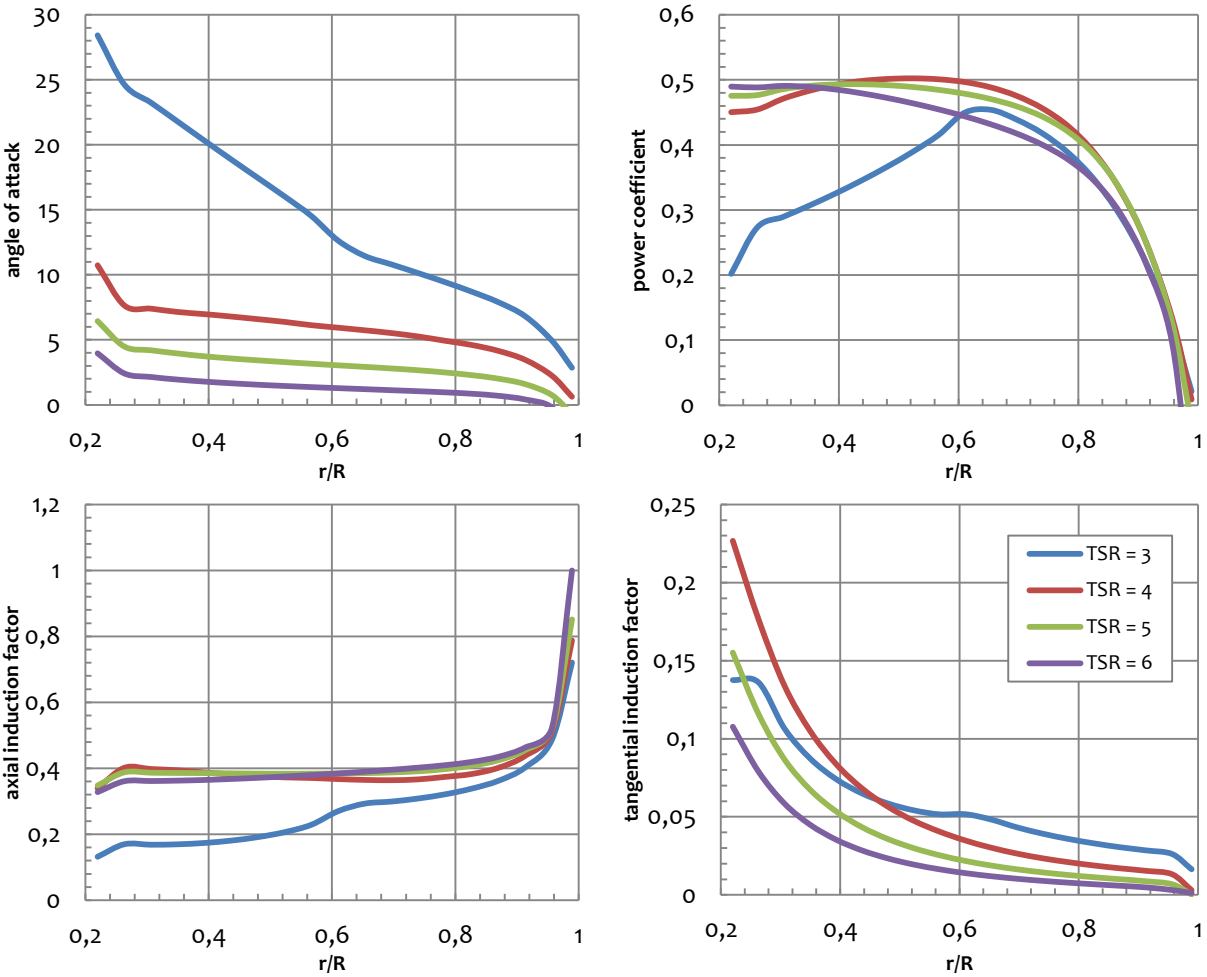

Figure 3-15: Span-wise characteristics of inflow angle (top left), power coefficient (top right), axial induction factor (bottom left) and tangential induction factor (bottom right) for the design condition of the IFREMER-LOMC configuration with 0° set pitch angle and a range of TSR

There are three important observations from the graphs shown in Figure 3-15. The converged angles of attack (α) show that for TSR > 3, the angle of attack has a value lower than 11°. From Chapter 2.3 it is shown that the 2-D lift- and drag characteristics for the different sections all lie in the range of the laminar behaviour of the foil. For TSR = 3 higher angles of attack are obtained, especially for the r/R < 0.6. The 2-D lift- and drag characteristics for this condition are determined by the Viterna extrapolation method, explained in Chapter 2.3.

The other three graphs all show a variant behaviour for TSR = 3. This indicates that the 2-D lift- and drag characteristics in the extrapolated region are likely to give a good approximation, but do not give the correct values.

The C_p curves of the segments show a notable difference for TSR = 3. Because of the higher angles of attack and the 2-D characteristics obtained from the extrapolated region, the curve shows quite a different distribution than the curves for larger TSR. It is striking however that the numerical model does show quite a good fit with the experimental data for this smaller values of TSR. This indicates that BEM is a robust method for the prediction of turbine loads.

4 Unsteady modelling

Chapter 4 continues on Chapter 2 by extending the classical BEM theory with an unsteady inflow field. The numerical results presented in Chapter 3 are based on a uniform inflow field. In order to analyse the influence of platform motions on the hydrodynamic behaviour of the turbine it is necessary to take into account an unsteady inflow field as result of current, waves and platform motions. Chapter 4 describes the implementation of an unsteady inflow field in the BEM theory. The model is verified by numerical results of the steady BEM model and with analytical solutions. Validation is achieved by means of comparing numerical results with measurement data of model tests. Verification and validation of the unsteady model is the topic of Chapter 5.

4.1 Time domain simulations

To analyse the influence of platform motions and varying environmental inflow conditions it is necessary to be able simulate the turbine performance in time domain. Time domain allows for an unsteady inflow field to serve as input for BEM theory and more analytical approach like the actuator disk theory.

An important aspect to take into consideration while analysing the results is that the unsteady flow field is the result of the horizontal components of wave particle velocity, current velocity, and platform induced velocity at the blades. Only the vertical shear of the velocity profile in the x-z plane is considered.

This means that a number of flow effects which will have an influence on turbine performance are not considered in this thesis. These have been extensively discussed in the definition study of this thesis (2).

4.2 Unsteady flow field

The flow field around the BlueTEC is described by the velocity potential. The velocity potential is a mathematical expression which has the property that the velocity component in a point in the fluid in any chosen direction is the derivative of this potential function in that point to that chosen direction. The velocity potential is built up of a number of components and is discussed in Appendix B in more detail. In this chapter the focus only is on the environmental component due to current and waves and a component induced by platform motions. Because test conditions during basin test all were unidirectional along the x-axis, only shear in the x-z plane is considered in this study.

The turbines of the BlueTEC platform are operating near the water surface. Tidal currents form the biggest driver of the turbines, but other velocity components add to the inflow velocity as well. The wave induced particle velocity is an important contributor to the environmental inflow velocity. Especially near the water surface and for higher wave amplitudes this component cannot be ignored.

Current and waves form the environmental part of the relative inflow velocity. The floating platform itself contributes to the relative inflow velocity by adding a component which is the result of platform motions. The moored platform will have certain motion behaviour under the influence of incoming waves, drag forces, mooring loads and loads exceeded on the platform by the turbines. In order to correctly describe the relative inflow velocity these platform motions should be taken into account as well when calculating turbine loads.

4.2.1 Current velocity profile

Tidal currents are under high influence of water depth and the topography of the seabed. The current is not uniform in velocity and direction. Traditionally the current velocity profile is described by a sheared profile according to a 1/7th power law, shown in the left graph of Figure 4-1.

The right graph of Figure 4-1 shows the measured current velocity profiles for the IFREMER circulation tank. These profiles show quite some difference with the theoretical profile described by the power law. The profile which is valid for tests without the wave maker installed shows on average larger current velocities which are the result of blockage in the tank. The velocity profile when the wave maker is installed shows quite some reduction in the current velocity near the water surface. This is the result of turbulence caused by the wave maker.

For a correct validation of the numerical results with the model tests it is important to use the correct velocity profile as input. For validation of current only tests, the velocity profile without wave maker will be used. For validation of current only test with wave maker installed, the profile with wave maker is used. The current velocity at the (vertical) position of the blade element will be generated from a lookup table. Profiles for the conditions of combined current and waves are discussed in Chapter 4.2.3.

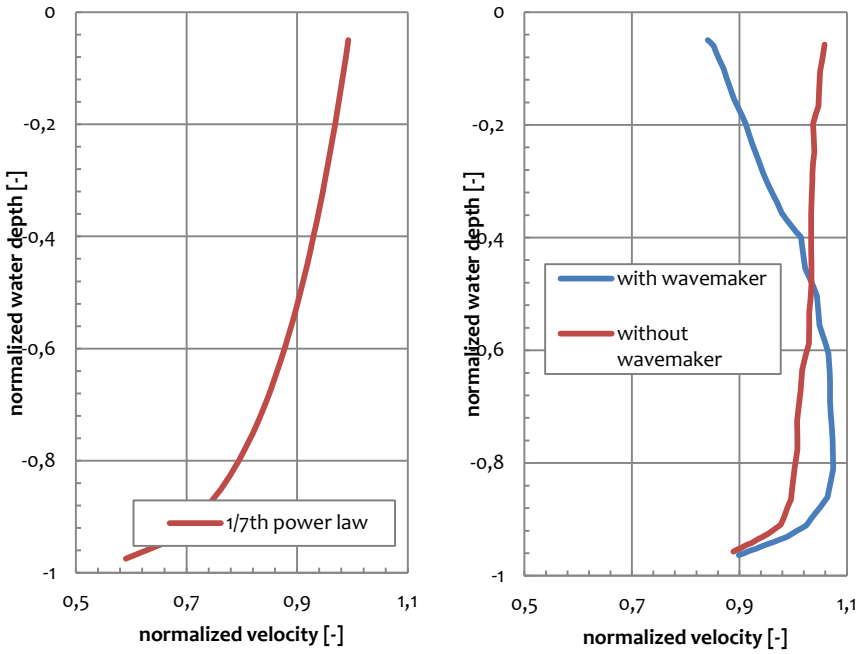

Figure 4-1: Normalized current velocity profile for a 1/7th power law (left graph) and vertical velocity profiles as measured in the IFREMER circulation tank (right graph)

For the sensitivity analysis in Chapter 6 it is of importance to use the correct current profile. This is dependent on many geological factors like seabed geometry, water depth and current direction. The horizontal current induced particle velocity at a depth z is often described according to a 1/7th power law

$$U_{current}(z) = U_{\infty} \cdot \left(\frac{z}{D}\right)^{1/7} \qquad \text{Equation 4-1}$$

In which:

U_{∞} = free stream current velocity (m/s)

z = local depth (m)
D = water depth (m)

4.2.2 Wave induced velocity profile

During model testing the BlueTEC platform is subjected to a propagating harmonic wave, a theoretical representation is shown in Figure 4-2. The wave elevation at location x at time t can be written as;

$$\delta(x,t) = a \cdot \sin(\omega t - kx) \qquad \text{Equation 4-2}$$

In which:

a = amplitude (m)
ω = wave frequency (rad/s)
k = wave number (-)

This wave is propagating in the positive x-direction. The linear wave theory is extensively discussed in for example (11). To implement the wave induced velocity the particle velocities are of interest. These can be derived from the velocity potential; this mathematical expression has the property that the velocity component in a point in the fluid in any chosen direction is the derivative of this potential function in that point to that chosen direction. The velocity potential is given by:

$$\varphi(x,z,t) = \frac{\omega a}{k}\frac{cosh[k(D+z)]}{sinh(kD)}cos(\omega t - kx) \qquad \text{Equation 4-3}$$

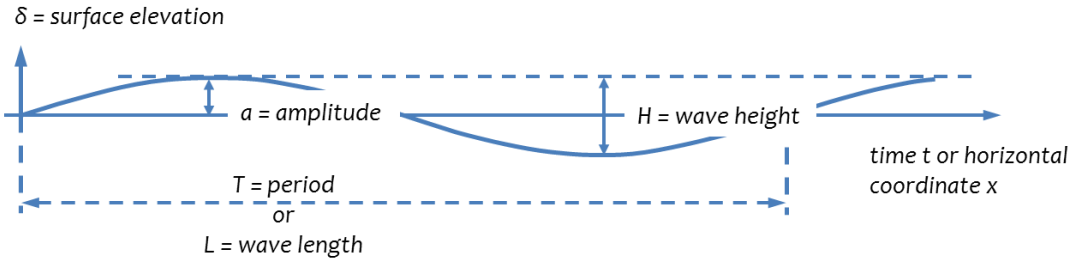

Figure 4-2: The sine wave

The spatial derivatives of φ are the velocity components; $\partial\varphi/\partial x = U_x$ and $\partial\varphi/\partial z = U_z$:

$$U_{x,wave}(x,z,t) = \omega a\frac{cosh(kz)}{sinh(kD)}sin(\omega t - kx) \qquad \text{Equation 4-4}$$

$$U_{z,wave}(x,z,t) = \omega a\frac{sinh(kz)}{sinh(kD)}cos(\omega t - kx) \qquad \text{Equation 4-5}$$

Only velocity components in x-direction are considered in this study, so that;

$$U_{wave}(x,z,t) = \omega a \frac{cosh(kz)}{sinh(kD)} sin(\omega t - kx)$$ Equation 4-6

The velocities are called 'orbital velocities' because they correspond to motions of the particles in circular orbits as shown in Figure 4-3.

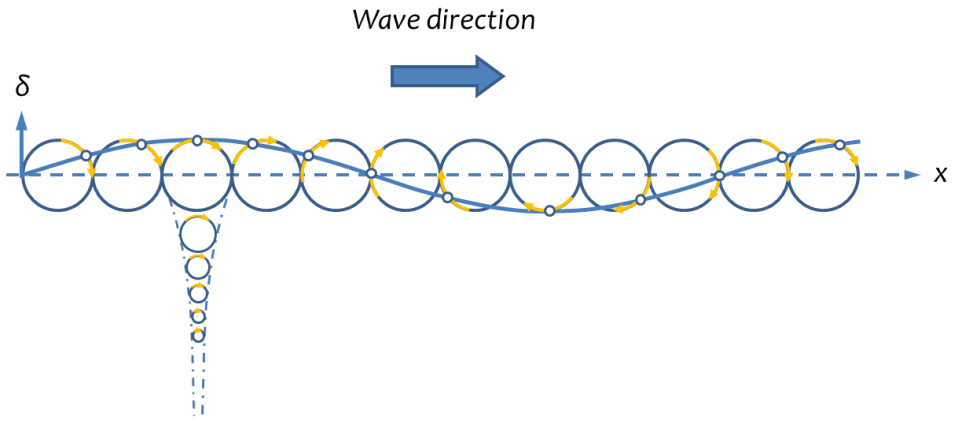

Figure 4-3: The orbital motion of the water particles under a harmonic wave that moves from left to right, shown for deep water

The basin tests are done on a 1/25th scale. The water depth in the circulation tank corresponds to a water depth of 50 meters on full scale. The wave number can be determined by the dispersion relationship. Although 50 meters is relatively shallow water, observations show that the orbital motion in the circulation tank, especially near the bottom of the tank, corresponds better to the dispersion relationship for deep water.

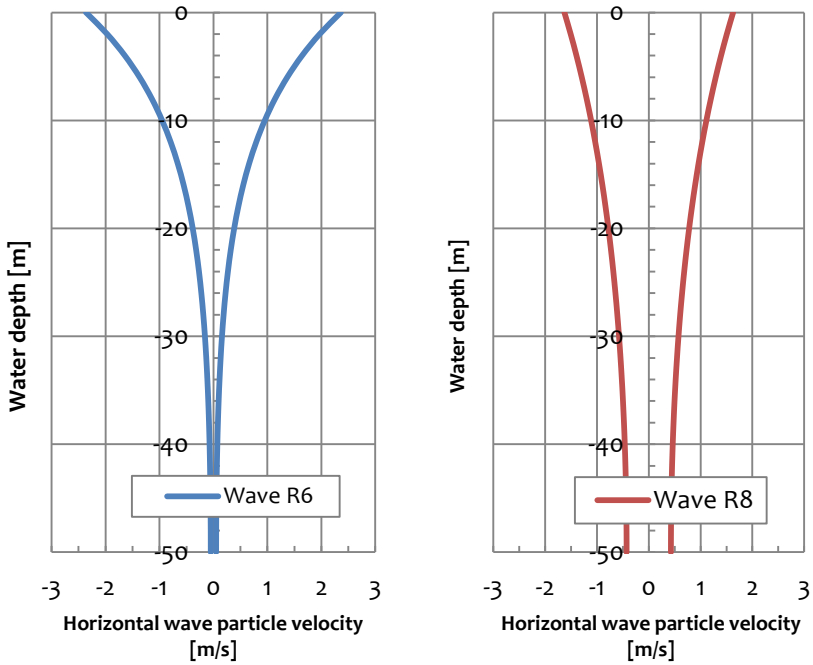

Figure 4-4: Maximum horizontal wave particle velocities in negative and positive x-direction. Wave condition R6 (left); H_s = 5.0 (m) & T_p = 6.67 (s). Wave condition R8 (right); H_s = 5.0 (m) & T_p = 10.0 (s)

The dispersion relationship for deep water is given by;

$$\omega^2 = gk \qquad \text{Equation 4-7}$$

From Equation 4-7 the expression for the wave number for very shallow water is obtained;

$$k = \omega^2/g \qquad \text{Equation 4-8}$$

Using Equation 4-4 and Equation 4-8 the minimum and maximum profiles of the horizontal wave induced particle velocity can be determined. These are shown for two wave conditions in Figure 4-4.

4.2.3 Wave-current interaction

In Chapter 4.2.1 the measured profiles in the circulation tank of IFREMER for the current only condition where presented. These profiles are published for the combined current and wave condition too (12) and are presented in Figure 4-5 and Figure 4-6 for two different current velocities. In both graphs the predicted horizontal wave particle velocities by linear wave theory are plotted. It is shown that this prediction does not coincide with the measurement. The theoretical profile can be tweaked in such a way that the velocities near the water surface are a little bit smaller by introducing a tweaking factor (C_{tweak}) in the cosine hyperbolic term in Equation 4-4;

$$U_{x,wave}(x,z,t) = \omega a \frac{cosh(C_{tweak} \cdot kz)}{sinh(kD)} sin(\omega t - kx) \qquad \text{Equation 4-9}$$

The tweaked profiles are shown in Figure 4-5 and Figure 4-6. For the 2 m/s current a tweaking coefficient of 0.94 gives a good fit with the measured velocity, for the 3 m/s current a coefficient of 0.90 seems to do the job. Validation of the numerical model is done against basin test for a 3.5 m/s current. If the tweaking coefficient is extrapolated a factor of 0.88 can be used to model the orbital velocity in the numerical model that comes close to the values measured in the circulation tank.

The downside of the approach is that the current- and wave profiles are given for a different wave condition than the wave conditions that have been used for testing the BlueTEC platform. During the model tests the amplitude of the waves is higher, and the periods are 6.67 s. and 10.0 s. for the relevant wave conditions. Because there is nothing known on the wave-current interaction for these environmental conditions, the best guess is to use the IFREMER profiles as presented in the figures below; a tweaking factor of 0.88 for the orbital velocities and the dimensionless current velocity which is given for the 3 m/s current case.

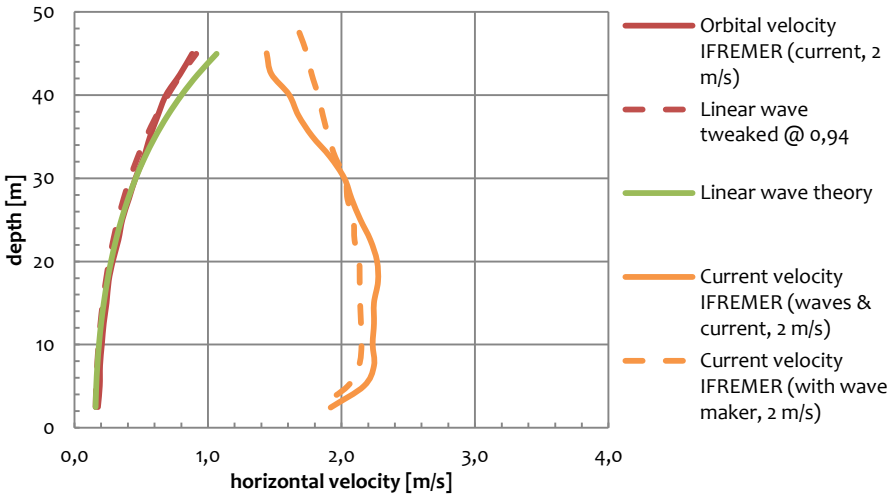

Figure 4-5: Velocity profiles for 2 m/s current & 1.875 m. wave amplitude @ 8.33 s. peak period

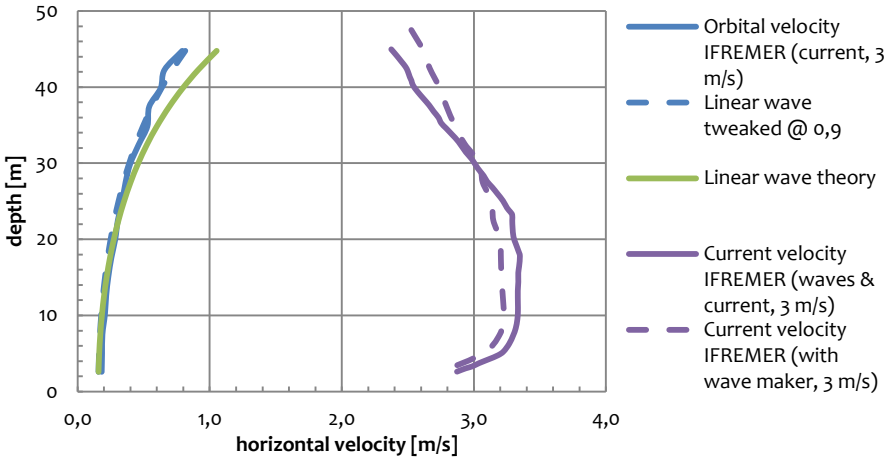

Figure 4-6: Velocity profiles for 3 m/s current & 1.875 m. wave amplitude @ 8.33 s. peak period

4.2.4 Platform motions

Figure 4-7 shows photos of the BlueTEC platform during the basin tests in the circulation tank. Eight images are shown, all indicating a different moment of one cycle of the hub motion. The location of the hub is indicated by the yellow dot, this dot lies on a small pink circle which indicates the motion path of the hub. This shows that the vertical hub motion can be described according to a sinusoidal motion. The waves and current travel from left to right.

Together with the hub motion, the motion of the water particles is indicated by white dots. The orbital motion as explained in Chapter 4.2.2 and Figure 4-3 is here shown as well by the red circles. A rough approximation of the wave elevation is indicated by the thin blue line.

In Figure 4-8 the 6 DoF of the platform are monitored. As the platform is subjected to regular longitudinal waves it is assumed that the platform only has a surge-, heave- and pitch motion. The position of the hub can be expressed related to the surge-, heave- and pitch motion of the platform; this is illustrated by Figure 4-9.

Figure 4-7: One period of the hub motion of the BlueTEC platform under the influence of current and waves during basin tests

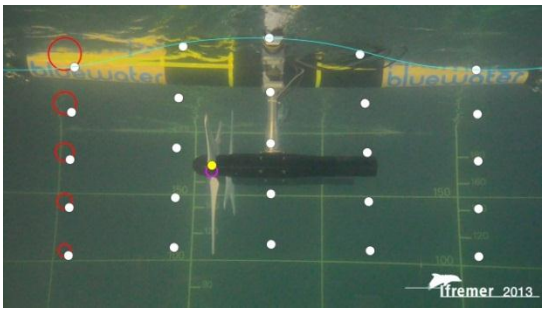

Frame 1

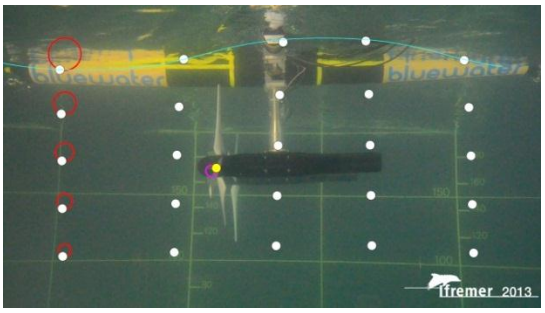

Frame 2

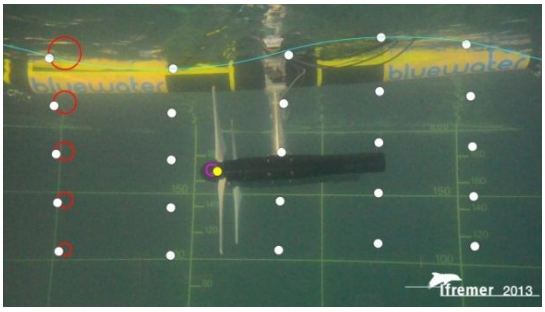

Frame 3

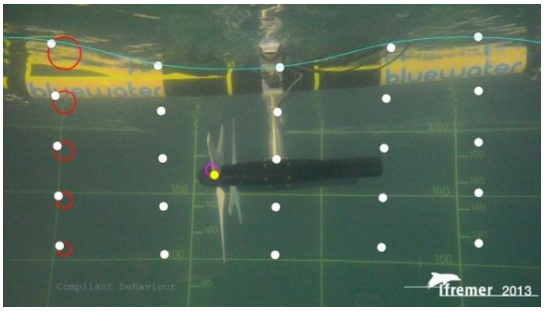

Frame 4

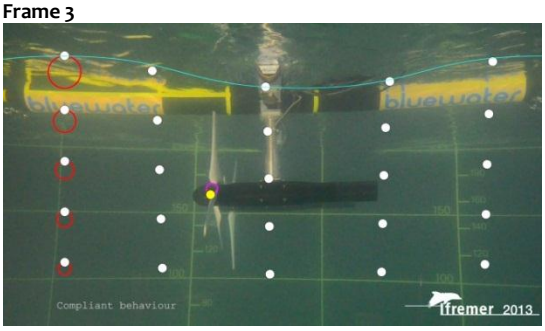

Frame 5

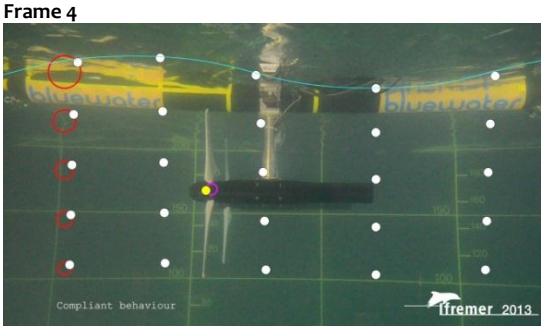

Frame 6

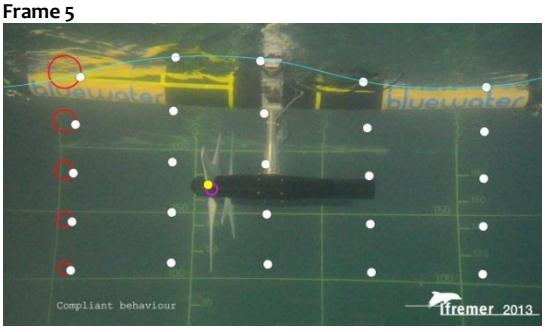

Frame 7

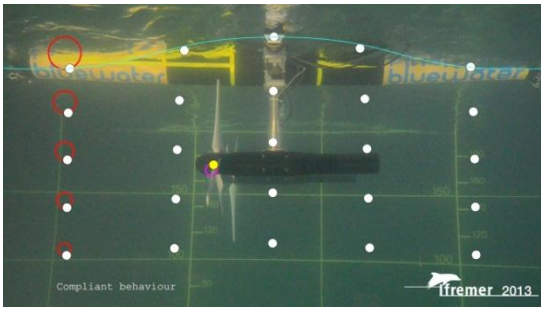

Frame 8

For the calculation of the relative inflow velocity the hub velocity component needs to be taken into account. Depending on platform motions, the hub will move towards the current, thus increasing the inflow velocity of move in the direction of the current and thus decreasing the inflow velocity. Focussing on the yellow dot in Figure 4-7 is shown that frame 1 starts at the wave crest. Here the platform starts to move in the same direction as the wave and current. This is continued to somewhere between frame 2 and 3 and during these steps; the platform motions induce a hub motion which reduces the relative inflow velocity. In frame 3 to frame 6 the opposite happens. Platform motions induce a hub motion which adds a component to the relative inflow velocity. Frame 7 and 8 shows a platform moving in the same direction of wave and current and thus reducing the relative inflow velocity at the blades.

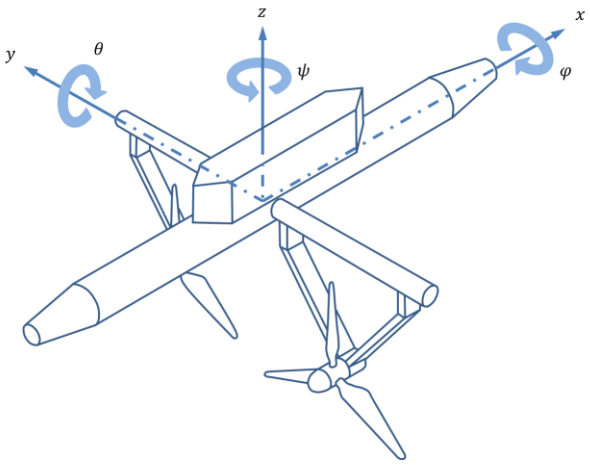

Figure 4-8: Definition of the platform coordinate system

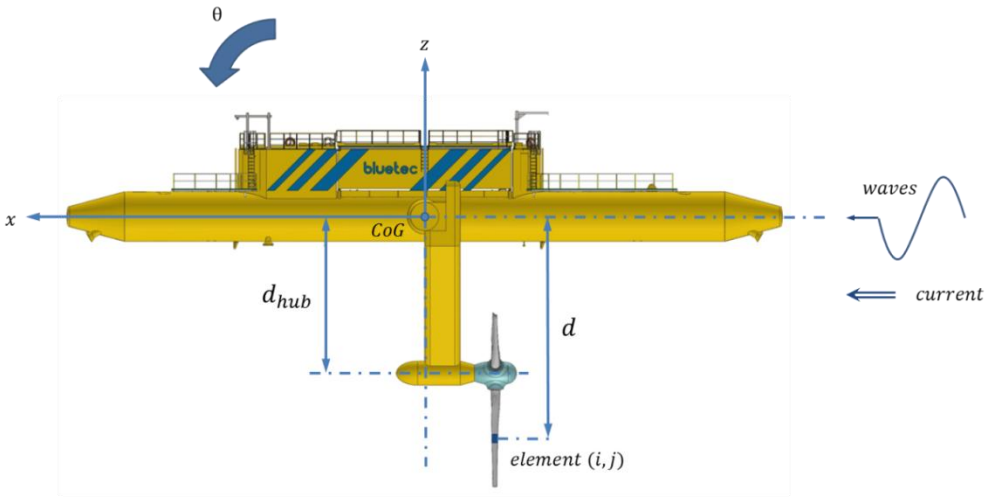

Figure 4-9: Position of the hub related to the CoG of the platform

During the basin tests the surge, heave and pitch motions are monitored for each time step. The velocities in surge and heave direction and the angular velocity can be calculated from these measurements by considering two consecutive points of the relative DoF;

$$\dot{x}_{platform}(t) = \frac{x_{platform}(t) - x_{platform}(t - dt)}{dt}$$ Equation 4-10

$$\dot{\theta}_{platform}(t) = \frac{\theta_{platform}(t) - \theta_{platform}(t - dt)}{dt}$$ Equation 4-11

In time domain simulations the inflow velocity at each blade element is considered separately. The vertical location of a blade element is dependent on time and the frequency of the turbine. Current- and wave induced horizontal particle velocities are already calculated as function of the vertical position in the water column. The hub induced horizontal velocity can be determined from the platform motions. The hub velocity component is determined by the surge velocity and angular velocity of the pitch motion; see Equation 4-12.

$$U_{platform}(t,i,j) = -\dot{x}_{platform}(t) + d(t,i,j) \cdot \dot{\theta}_{platform}(t)$$ Equation 4-12

In which d is the vertical distance between the CoG of the platform the midpoint of the blade element. The distance from the CoG of the platform and the centre of an element is given by;

$$d(t,i,j) = d_{hub} - d_{i,j}(t)$$ Equation 4-13

In which d_{hub} is the distance between the CoG of the platform and the centreline of the hub and $d_{i,j}(t)$ is the vertical position of a blade element relative to the hub at time t. This position is dependent on the local radius of the element, the tip speed ratio, the blade and the time.

$$d_{i,j}(t) = r(i) \cdot \cos(\omega t + \varepsilon_{blade}(j))$$ Equation 4-14

The phase angles of the blades are given by;

$$\varepsilon_{blade}(1) = 0\ [rad]$$

$$\varepsilon_{blade}(2) = 2/3\pi\ [rad]$$

$$\varepsilon_{blade}(3) = 4/3\pi\ [rad]$$

The dimensionless vertical position of a blade element relative to the hub is given in Figure 4-10. Shown are the positions for the same element on each blade for one period. The lines correspond to elements indicated in Figure 4-11. The rotation direction of the rotor is indicated by Ω.

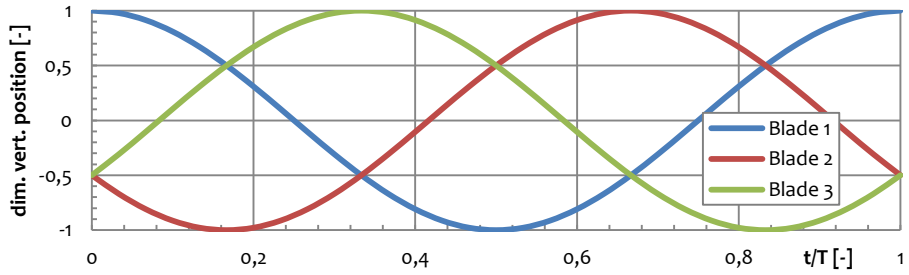

Figure 4-10: Dimensionless vertical position relative to the hub position for a blade element during revolution of the turbine. The blades refer to Figure 4-11 where the blade elements are colour indicated and the rotation direction is shown.

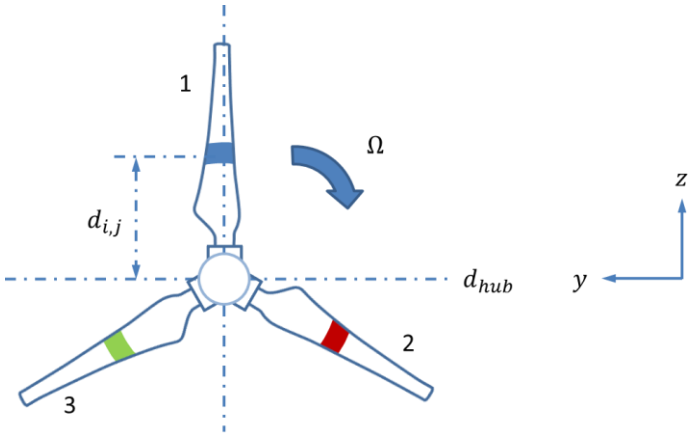

Figure 4-11: Vertical location of blade elements and rotation direction, position of the rotor shown at t = 0.

4.2.5 Relative inflow velocity

The relative inflow velocity is the result of current, waves and platform motions. Figure 4-12 shows the maximum and minimum values for a 3.5 m/s free stream velocity distributed according to a $1/7^{th}$ power law combined with the horizontal wave induced particle velocity for a wave of 5.0 meter significant wave height and a 6.67 second peak period.

The minima and maxima are indicated by the blue lines. The dotted red lines give the upper and lower boundaries of the turbine in captive condition. The vertical green line forms a representation of the current velocity as if when the velocity profile is considered as a uniform profile with a velocity equal to the free stream velocity. The sheared profiles show that the combination of waves and current gives a complete different inflow profile from a simple uniform profile. The profile shown is the result of waves and current only. As illustrated in

Figure 4-7 the platform motions result in hub motions to. Translated to the figure shown below, this means the rotor will move from left to right and this will add to the vertical velocity shear. The resulting inflow velocity in x-direction is described by Equation 4-15.

$$U_{rel}(t,i,j) = U_{wave}(x,z,t) + U_{current}(z) + U_{platform}(t,i,j) \qquad \text{Equation 4-15}$$

The x- and z-coordinate of element (i,j) to calculate $U_{wave}(x,z,t)$ and $U_{current}(z)$ are calculated according to;

$$x(t,i,j) = x_0 + x_{platform}(t) + d(t,i,j) \cdot \theta_{platform}(t) \qquad \text{Equation 4-16}$$

$$z(t,i,j) = z_0 + z_{platform}(t) + d(t,i,j) \qquad \text{Equation 4-17}$$

4.3 Unsteady flow field & turbine performance

Most available theories to analyse the performance of a turbine are based on a uniform inflow. Figure 4-12 shows that for a specific combination of current and waves the real inflow velocities on the rotor can differ quite a lot from the free stream velocity and that there can be quite some shear over the height of the rotor. This unsteady flow field causes fluctuating loads on the rotor and results in varying power outputs. To correctly analyse turbine performance the fluctuating inflow velocity cannot be neglected and should be taken into account for the analysis of turbine performance.

The purpose for the correct prediction of turbine performance in an unsteady flow field is to analyse the effect of fluctuating inflow as result of environmental conditions and platform motions on turbine performance. There are a number of approaches which can be used to analyse turbine performance, but all are normally used in a uniform inflow field and so they simplify real life.

The blade element momentum theory as it is described in Chapter 2.1 can be adjusted in such a way that an unsteady inflow field can be taken into account. Different approaches will be described in Chapter 4.4 and Chapter 4.5, based on actuator disk theory and BEM theory. For every approach a numerical model is developed which allows a time domain simulation of the axial loading of a tidal turbine in an unsteady inflow as result of current, waves and platform motions. Simulations of the unsteady BEM approaches are verified with the steady BEM model and validated against measurements from basin tests in Chapter 5.

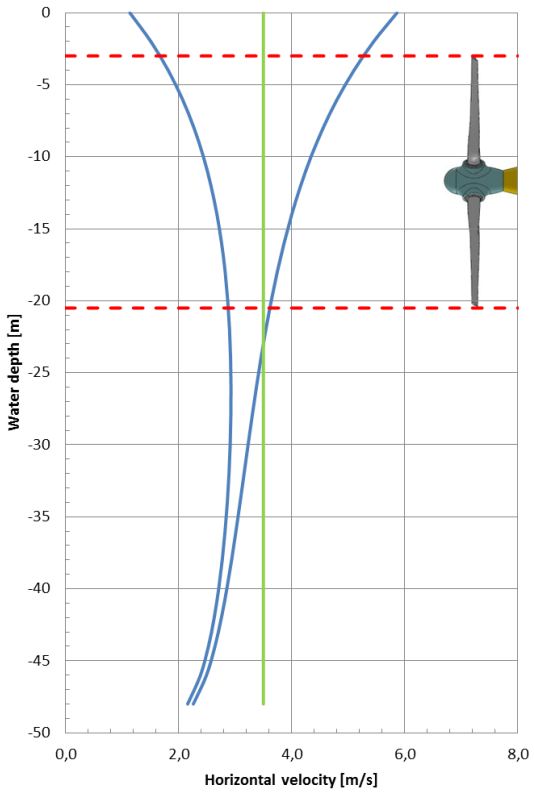

Figure 4-12: Environmental inflow velocity profiles of combined current and waves. 3.5 m/s free stream and wave condition R6

4.4 Actuator disk theory

Currently the actuator disk theory is used to estimate the drag load on the turbine. The theory of the actuator disk has been discussed in the definition study leading to this thesis (2). In this approach the

turbine is represented by a disk with radius R. The drag coefficient of the disk is assumed to be equal to 0.8; this value is based on earlier analytical calculations performed by Bluewater. This value will be used for further analysis.

The drag load on the disk is calculated according to Equation 4-18;

$$F_{drag} = 0.5 \cdot \rho \cdot V^2 \cdot \pi \cdot R^2 \cdot C_D \qquad \text{Equation 4-18}$$

Equation 4-18 assumes a constant inflow velocity (V) for the whole disk. As Figure 4-12 illustrated this is not the reality. A simple way to take into account sheared inflow in the x-z plane is by dividing the disk in a number of strips, as illustrated in Figure 4-13. The drag load per strip is calculated according to Equation 4-18, but now the relative inflow velocity at the centre of the strip and its respective area are taken into account. Summation of the drag loads on the different strips gives the total drag. This approach also enables to make a rough estimation of the moment around the y-axis of the hub.

Instead of dividing the disk in a number of strips and taking into account the relative inflow velocity at each centre, another approach would be to simply calculate the average inflow velocity over the height of the disk. For the calculation of the drag load this would make no difference, it would be a faster solution. However, the strip approach does allow us to make an estimation of the moment around the hub which is not possible if the average inflow velocity is applied to the whole disk.

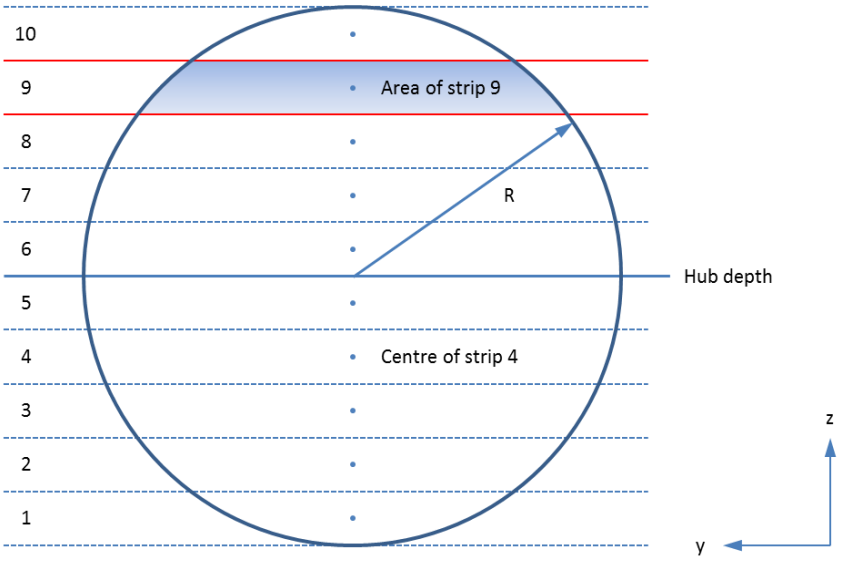

Figure 4-13: Actuator disk approach, disk divided by ten strips of equal height

The drag load per strip (n) is calculated according to Equation 4-19;

$$F_x(t,n) = 0.5 \cdot \rho \cdot U_{rel}(t,n)^2 \cdot A(n) \cdot C_D \qquad \text{Equation 4-19}$$

The relative inflow velocity on each strip is the result of waves, current and platform motions and given by Equation 4-20;

$$U_{rel}(t,n) = U_{wave}(x,z,t) + U_{current}(z) + U_{platform}(t,n) \quad \text{Equation 4-20}$$

The platform induced velocity on a strip is given by Equation 4-21;

$$U_{platform}(t,n) = -\dot{x}_{platform}(t) + d(n) \cdot \dot{\theta}_{platform}(t) \quad \text{Equation 4-21}$$

In which $d(n)$, the distance from the CoG of the platform to the centre of strip (n) is given by Equation 4-22 and Equation 4-23;

$$d(n) = d_{hub} - \frac{1}{2} \cdot R + \left(-\frac{1}{2} + n\right) \cdot dn \quad \text{Equation 4-22}$$

$$dn = (2 \cdot R)/N \quad \text{Equation 4-23}$$

The x- and z-coordinate of strip (n) to calculate $U_{wave}(x,z,t)$ and $U_{current}(z)$ are calculated according to;

$$x(t,n) = x_0 + x_{platform}(t) + d(n) \cdot \theta_{platform}(t) \quad \text{Equation 4-24}$$

$$z(t,n) = z_0 + z_{platform}(t) + d(n) \quad \text{Equation 4-25}$$

The total drag load of the disk, taking into account a sheared velocity profile, is calculated according to Equation 4-26. The moment around the y-axis of the hub is calculated according to Equation 4-27.

$$F_x(t) = \sum_n F_x(t,n) \quad \text{Equation 4-26}$$

$$M_y(t) = \sum_n [z(t,n) \cdot F_x(t,n)] \quad \text{Equation 4-27}$$

Reflection on the approach

The actuator disk theory is a very simple way to estimate the loads on the turbine. It allows for fast calculations, only one drag coefficient is used for the complete disk and there is no need for intensive iterations to determine the induction factor. No lookup tables are used. The choice for the value of the drag coefficient however needs to be done with care and highly influence the results of the method.

4.5 Unsteady flow field & BEM theory

The BEM theory is discussed in Chapter 2. In this theory the rotor is assumed to be built up of a number of ring elements. Each ring element experiences the same inflow velocity, equal to the free stream current velocity. This is illustrated in Figure 4-14. The vertical shear of the velocity profile results in a different inflow velocity at each blade element (illustrated as dark blue trapezoids in the figures below). The illustration shown in Figure 4-15 approaches the situation in real life. Every element on each blade experiences a different relative inflow velocity which results in different loading across one ring element.

To take into account the vertical shear of the velocity profile the steady BEM theory is modified in such a way to make it possible to analyse the effect of an unsteady flow on the turbine performance. These approaches are discussed in Chapter 4.5.1 and Chapter 4.5.2.

4.5.1 1/3 ring elements

One approach is to consider a separate inflow velocity for 1/3 part of a ring element. In traditional BEM theory the force coefficients are determined per ring element. Each ring spans the three blades and as is shown in Figure 4-15 the blade elements in one ring will experience a different inflow velocity due to the velocity shear. In order to make a distinction between these three different inflow velocities and taking into account a sheared velocity profile a method is used proposed in (1).

In this approach, each blade element spans 1/3 of the area of the ring element, as illustrated in Figure 4-16. Using this area, the thrust and torque forces resulting from the inflow velocity for that element is calculated. For each ring, the three separate forces are summed. The sum of all forces over all the rings then determines the total thrust and torque force on the rotor.

This approach allows calculating the thrust force and the moment around the y-axis of the hub of the rotor. The method is based on lookup tables for the normal coefficients. From this, the force the turbine produces in x-direction (F_x), and the moment around the hub can be calculated (M_y).

$$F_x(t,i,j) = 0.5 \cdot \rho \cdot U_{rel}(t,i,j)^2 \cdot c_n(i) \cdot 1/3 \cdot A(i,j) \qquad \text{Equation 4-28}$$

The total force in x-direction and the moment around the hub is calculated by first summing for one ring element, and then summing all ring elements so that the complete rotor is covered;

$$F_x(t) = \sum_{i=1}^{N_s} \sum_{j=1}^{N_b} F_x(t,i,j) \qquad \text{Equation 4-29}$$

$$M_y(t) = \sum_{i=1}^{N_s} \sum_{j=1}^{N_b} [z(t,i,j) \cdot F_x(t,i,j)] \qquad \text{Equation 4-30}$$

Reflection on the approach

The approach of 1/3 ring elements has one major flaw; the method is not consistent with the classical blade element momentum theory. The lookup tables for the axial force coefficient that are created by applying the classical BEM theory (Chapter 2) are based on a uniform inflow and the area of one complete ring

element. The inflow velocity is constant across the area of the element. In Equation 4-28 this coefficient is accordingly used for only 1/3 of the area and a varying inflow velocity U_{rel}.

This varying velocity over one complete ring element means that for each blade element different induction factor should be used. Herein lays the inconsistency of this approach; despite different inflow velocities across a ring element, the coefficients in the lookup tables are based on an inflow velocity which is constant across a ring element.

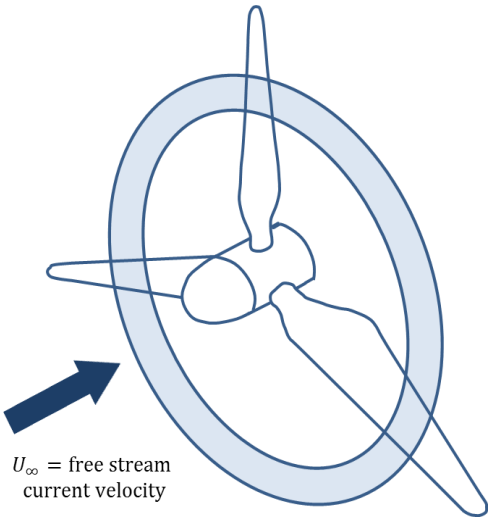

Figure 4-14: Traditional BEM approach, same uniform inflow velocity on each ring element

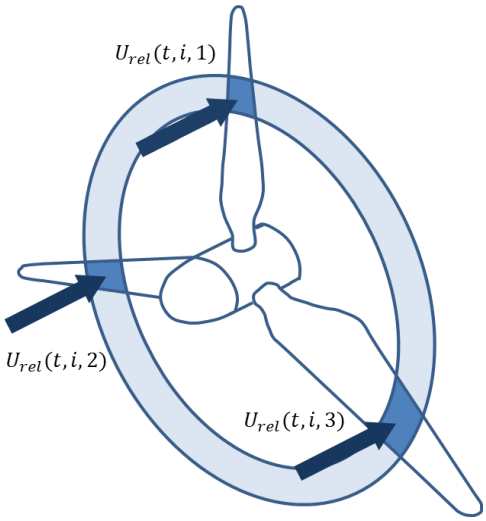

Figure 4-15: Representation of different local inflow velocities on each blade element

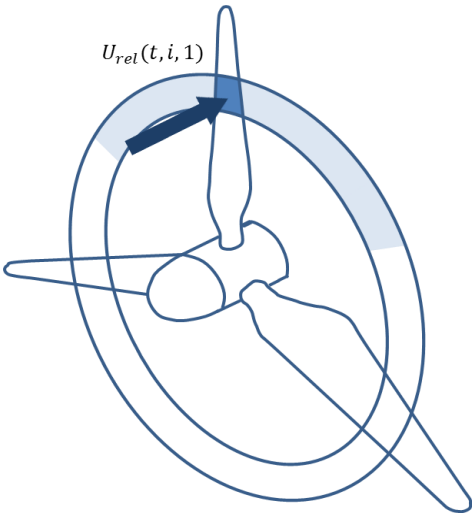

Figure 4-16: Considering a sheared velocity profile by dividing the ring element in three equal parts and using local inflow velocities

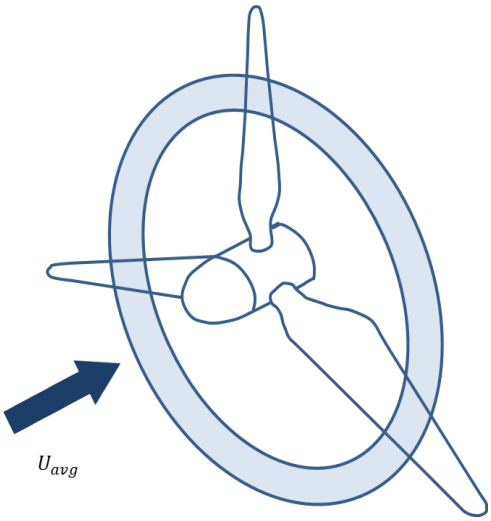

Figure 4-17: Considering a sheared velocity profile by using the average velocity over the blade elements illustrated in Figure 4-15

4.5.2 Averaged inflow velocities

This approach differs from the approach of 1/3 ring elements in that the same relative inflow velocity for one complete ring element is taken into account, as is illustrated in Figure 4-17. The vertical shear of the velocity profile is accounted for by taking the average of the relative inflow velocities at the blade elements according to Equation 4-31;

$$U_{avg}(t,i) = \frac{U_{rel}(t,i,1) + U_{rel}(t,i,2) + U_{rel}(t,i,2)}{3}$$ Equation 4-31

Now, the load in x-direction is calculated for each ring element according to Equation 4-32;

$$F_x(t,i) = 0.5 \cdot \rho \cdot U_{avg}(t,i)^2 \cdot c_n(i) \cdot A(i)$$ Equation 4-32

The total load, exerted by the turbine on the platform is given by summation of Equation 4-32 over the total number of ring elements, this gives Equation 4-33;

$$F_x(t) = \sum_{i=1}^{N_s} F_x(t,i)$$ Equation 4-33

Reflection on the approach

This approach is a more consistent method, in line with the BEM theory. In this method the analysis of the turbine loading is kept the same as in the original BEM theory, the adjustment with respect to the unsteady inflow is in the part of the velocity calculation instead of in the part of the performance calculation. Here, the unsteady inflow velocity is dealt with differently; in the previous BEM approach the part of turbine performance is adjusted.

The downside of this approach that is does not allow for analysis of hub moments, because one averaged velocity is considered for one complete ring element.

5 Verification & validation of the unsteady model

Chapter 5 deals with the verification and validation of the time domain approaches that have been discussed in Chapter 4. The goal of the analysis is to draw conclusions about which approach is suitable to predict the turbine performance in an unsteady inflow field. The unsteady inflow field is the results of current, waves and platform motions. This theory was described in Chapter 4. Time series of turbine loading have been obtained from basis tests performed by Bluewater at the IFREMER circulation tank. These datasets will serve as validation data for the unsteady model.

5.1 Verification with the steady BEM model

Results from the steady BEM model, presented in Chapter 3 will serve as verification of the unsteady model in Chapter 5.1. Only the uniform inflow field in the unsteady model can be verified by the steady BEM results (Chapter 5.1.1). An unsteady inflow field is verified by analytical results in Chapter 5.1.2.

5.1.1 Uniform inflow condition

Figure 3-12 presented the power and thrust coefficients for the design condition. The design condition is the zero degree pitch angle and a 3.5 m/s current velocity. The inflow field considered for the BEM simulations in Chapter 3 is a uniform inflow field. The unsteady model is based on lookup tables which have been generated by the steady BEM model. This implies that when a uniform inflow field is considered in the unsteady (BEM approach) models, the curves for the power and thrust coefficients should coincide with the one obtained from steady BEM. The goal of the verification is to check if the calculation of the element location and the calculation of the relative inflow velocities due to current at the element location are correctly implemented. When results coincide, this also means that the lookup tables are correctly implemented.

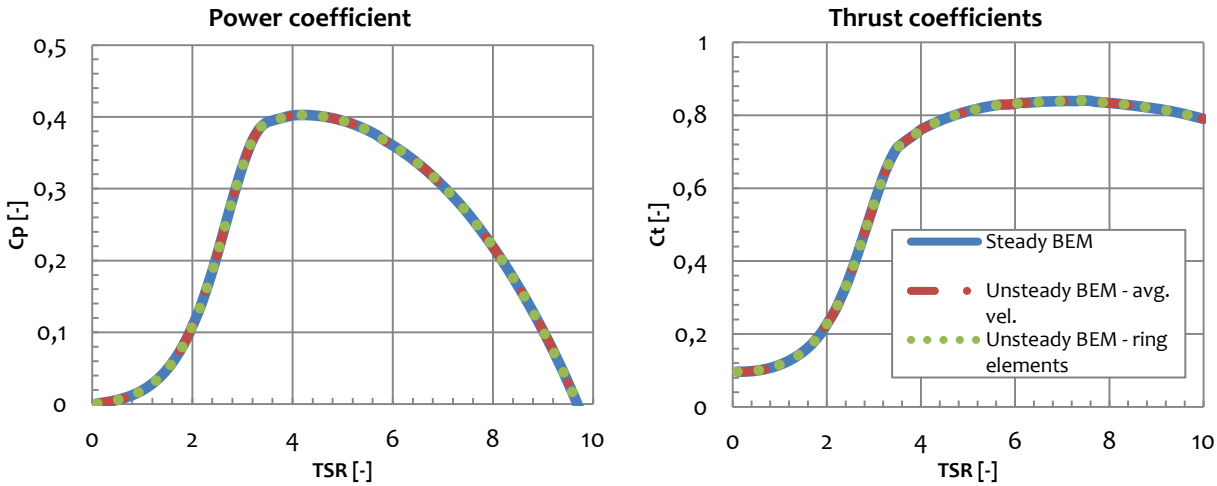

Figure 5-1: Comparison between numerical result of the steady BEM model and the two approaches of the unsteady BEM model with a uniform flow field for design condition

Figure 5-1 shows the comparison between the numerical result of the steady BEM model and the two approaches of the unsteady BEM model with a uniform flow field for the design condition. It is very clear that both approaches show exactly similar results to the steady BEM model, as expected.

This means that the lookup tables are correctly implemented and that the correct inflow velocities are calculated at the blade element locations. This however is still quite a simplified case. An analytical check of the calculated inflow velocities in the numerical model can provide with more confidence in the correct implementation of the unsteady inflow field.

5.1.2 Analytical results

For the analytical check of the unsteady flow field a number of conditions are considered. The relative inflow velocity will be calculated at different water depths with the unsteady model and by means of hand calculations according to the equations presented in Chapter 4. The current only condition, waves and current and the moored condition will be evaluated. For the moored condition a sinusoidal behaviour of the surge, heave and pitch motion is assumed with a phase lag respective to the incoming wave. As *reference* for the hub depth, a value of 17.5 meters below mean water level is chosen.

Current only condition

The right graph of Figure 4-1 shows the two current profiles as measured in the circulation tank of IFREMER. The profile is shown for the situation of current only (without the wave maker installed) and for the condition of waves and current (with the wave maker installed, or lowered).

The correct horizontal particle velocity due to current is determined by means of lookup tables. From the graphs presented in (12) and discussed in Chapter 4.2, the dimensionless current velocity is determined for a number of random water depths and these are stored in lookup tables. The unsteady model calculates the vertical position of a blade element for each time step according to Equation 4-17 for the two BEM approaches and according to Equation 4-25 for the actuator disk approach. With this location the correct horizontal current velocity is determined from the lookup tables by means of linear interpolation. This showed to be a robust method to determine the correct horizontal particle velocity due to current.

Waves & current

For this condition the current velocity for the design condition $(3.5\ \mathrm{m/s\ free\ stream})$ of the turbine is considered and a wave with 5.0 meter significant wave height (H_s) and a peak period of 6.67 seconds, also referred to as wave "R6". The platform is held captive, this means the relative inflow velocity is a combination of the horizontal current- and wave induced particle velocity.

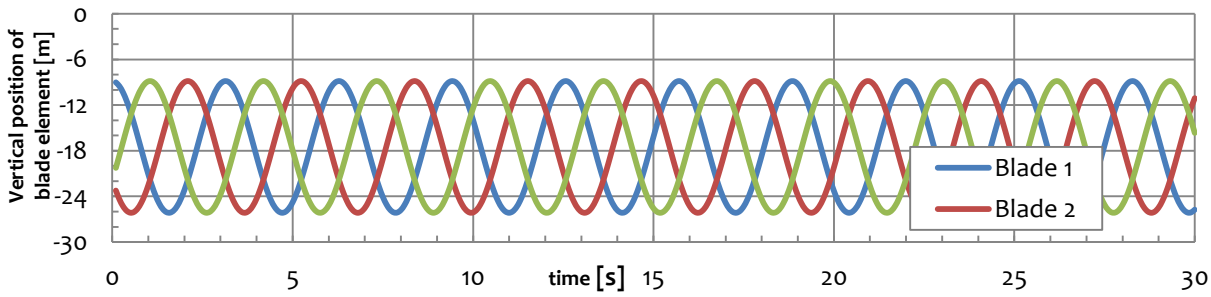

Figure 5-2: Time series of the vertical location of the most outward elements on all three blades, presented for TSR = 5.0 and a captive platform

From the unsteady model a time series of the vertical position can be generated for a blade element (i, j). These are presented in Figure 5-2 for the element closest to the tip of the blades for all blades j. The tip speed ratio is chosen to be equal to 5.0. Note that Equation 4-13 gives the absolute distance between the CoG of the platform and the centre of the blade element. The figure below gives the distance from the centre of the blade element relative to the water surface.

Figure 4-12 showed the combined vertical velocity profile for a 3.5 m/s free stream velocity and wave "R6". The vertical current velocity profile in this figure was distributed according to a 1/7th power law but the figure makes clear that the horizontal velocity fluctuating in the upper layer of the water column is larger than at larger water depth. This can be checked for the vertical positions of the blade elements shown in Figure 5-2 by generating time series of the relative inflow velocity on the blade elements calculated by Equation 4-15, these time series are presented in Figure 5-3.

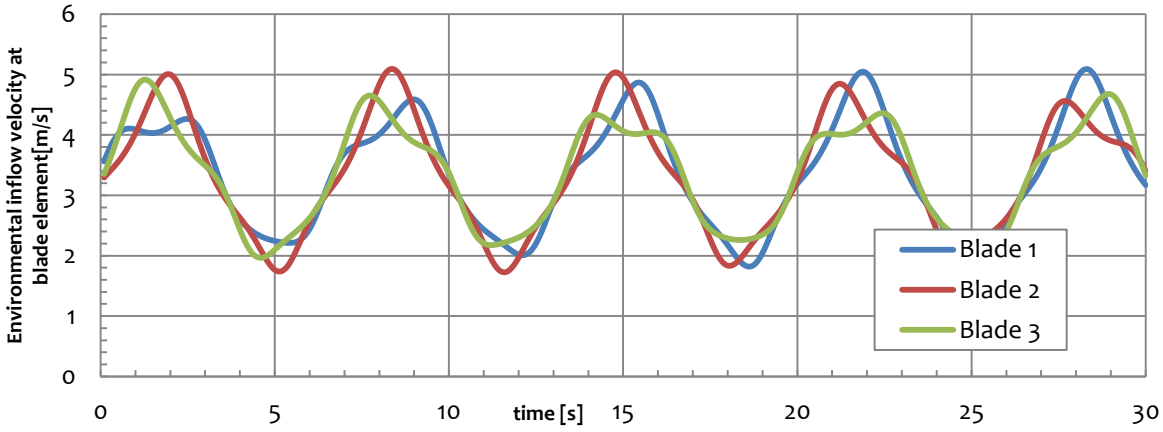

Figure 5-3: Time series of the relative inflow velocity on the most outward elements on all three blades, presented for TSR = 5.0 and a captive platform

From Figure 5-2 and Figure 5-3 it is observed that the vertical position of the blade element does not have such a big effect on the environmental inflow velocity it experiences. The environmental inflow velocity is mainly dominated by the wave particle velocity as it is clear that the periods of the relative inflow velocities at the blade elements are approximately similar to the wave period of 6.67 seconds.

The numerical results presented in Figure 5-2 and Figure 5-3 can be checked by hand calculations, according to the theory discussed in Chapter 4. For a number of points in Figure 5-2, the environmental inflow velocity can be obtained from Figure 5-3. These numerical results are compared with the results from hand calculations in Table 3.

The relevant equations from Chapter 4 are repeated below. The vertical distance between the CoG of the platform and the centre of the blade element is given by Equation 5-1 and Equation 5-2;

$$d(t, i, j) = d_{hub} - d_{i,j}(t) \qquad \text{Equation 5-1}$$

$$d_{i,j}(t) = r(i) \cdot \cos(\omega_{turb} t + \varepsilon_{blade}(j)) \qquad \text{Equation 5-2}$$

The platform is held captive, which implies platform motions equal zero and the vertical position of a blade element is only the result of the rotating turbine given by Equation 5-1. Also, the x-location of the blade element is constant and can be left out. Equation 4-17 becomes;

$$z(t,i,j) = d(t,i,j)$$ Equation 5-3

The relative environmental inflow velocity is now only the function of the wave particle velocity and current particle velocity at depth z. Equation 4-15 becomes;

$$U_{rel}(t,i,j) = U_{wave}(z,t) + U_{current}(z)$$ Equation 5-4

$U_{wave}(z,t)$ follows from Equation 4-6 and then becomes;

$$U_{wave}(z,t) = \omega_{wave} a \frac{\cosh\big(k \cdot (D-z)\big)}{sinh(kD)} sin(\omega_{wave} t)$$ Equation 5-5

$U_{current}(z)$ is given by a 1/7th power law, according to Equation 4-1;

$$U_{current}(z) = U_{\infty} \cdot \left(\frac{(D-z)}{D}\right)^{1/7}$$ Equation 5-6

Equation 5-3 and Equation 5-4 can be used to calculate the relative inflow velocity at a blade element analytically. These can be compared with the numerical results of Figure 5-2 and Figure 5-3 to check the implementation of theory in the numerical model.

Applying these for element 19, on blade 1, for $t = 10\ (s)$ gives;

$$z(10,19,1) = 17.5 - (8.665 \cdot \cos(2 \cdot 10 + 0)) = 13.96\ (m)$$

$$U_{wave}(13.96,10) = 0.942 \cdot 2.5 \cdot \frac{cosh\big(0.0425 \cdot (50 - 13.96)\big)}{sinh(0.0425 \cdot 50)} sin(0.942 \cdot 10) = 0.0066\ (m/s)$$

$$U_{current}(13.96) = 3.5 \cdot \left(\frac{(50 - 13.96)}{50}\right)^{\frac{1}{7}} = 3.34\ (m/s)$$

$$U_{rel}(10,19,1) = U_{wave}(13.96,10) + U_{current}(13.96) = 0.0066 + 3.34 = 3.35\ (m/s)$$

If this is done in a similar way for other points in time and for other blades Table 3 can be constructed. This shows that the hand calculations give the same results as the numerical model and it can be concluded that the theory is correctly implemented.

		Analytical result		Numerical result	
time (t)	blade (j)	$z(t,19,j)$ (m)	$U_{rel}(t,19,j)$ (m/s)	$z(t,19,j)$ (m)	$U_{rel}(t,19,j)$ (m/s)
10	1	13.96	3.35	13.9680	3.3465
20	2	20.20	3.24	20.1988	3.2403
30	3	15.66	3.34	15.6631	3.3353

Table 3: Analytical results for the captive platform

Moored condition

In moored condition the platform will get an excitation under the influence of incoming waves. To verify the numerical model for this condition, theoretical platform motions will serve as input for the numerical model. Time series of the displacements in surge- ($x_{platform}$), heave- ($z_{platform}$), and pitch-direction ($\theta_{platform}$), are needed, as well as the velocities in surge- ($\dot{x}_{platform}$) and pitch-direction ($\dot{\theta}_{platform}$). These time series can be represented by a sinusoidal function, with certain amplitude, frequency equal to the wave frequency and a certain phase shift with the wave surface elevation. Then a time series for the displacement in heave direction could look like the graph presented in Figure 5-4.

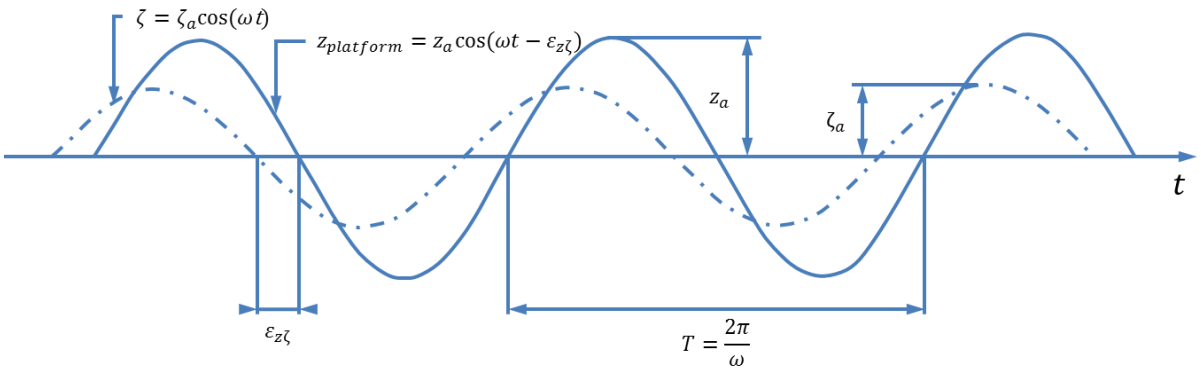

Figure 5-4: Harmonic wave and heave signal

Again, the results are verified by hand calculation to check if the theory is correctly implemented in the numerical model. For the waves & current condition is it concluded that these are correctly modelled, the addition of platform motions needs to be checked. Again a 3.5 m/s free stream current velocity is considered, distributed over the water depth according to a 1/7th power law, combined with wave condition "R6". This gives the following equation for the wave surface;

$$\zeta(t) = \zeta_a \cdot \cos(\omega_{wave} \cdot t) \qquad \text{Equation 5-7}$$

In this verification theoretical values are considered for the amplitudes of the surge-, heave- and pitch motion and their according phase angles. These are shown in the table below.

	Amplitude			Phase angle		
DoF	symbol	value		symbol	value	
surge	x_a	1.0	(m)	$\varepsilon_{x\zeta}$	$\pi/10$	(rad)
heave	z_a	1.25	(m)	$\varepsilon_{z\zeta}$	$\pi/10$	(rad)
pitch	θ_a	$\pi/90$	(rad)	$\varepsilon_{\theta\zeta}$	$\pi/10$	(rad)

Table 4: Theoretical platform motions

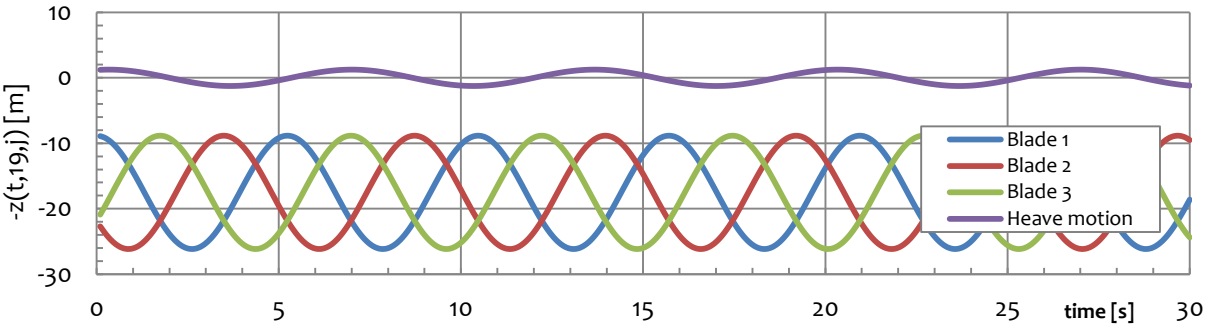

Figure 5-5: Time series of the vertical location of the most outward elements on all three blades, presented for TSR = 3.0 and a captive platform

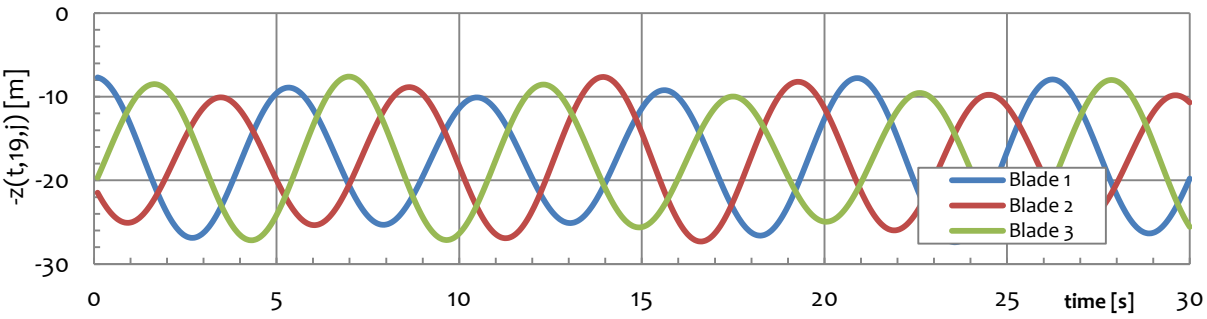

Figure 5-6: Time series of the vertical location of the most outward elements on all three blades, presented for TSR = 3.0 and a moored platform

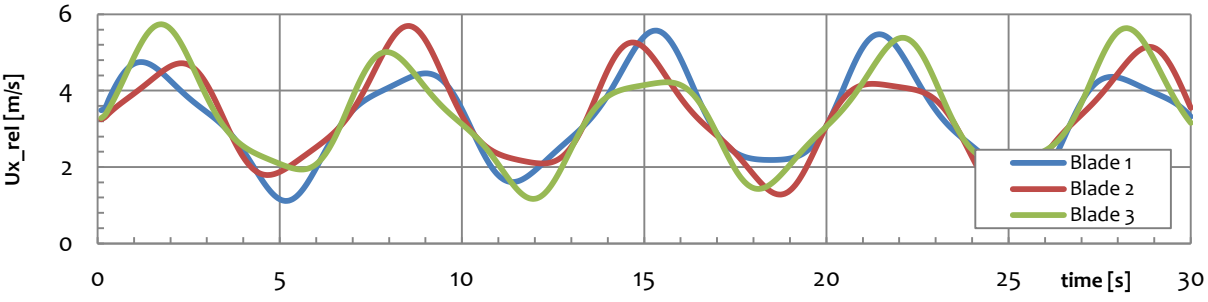

Figure 5-7: Time series of the relative inflow velocity on the most outward elements on all three blades, presented for TSR =3.0 and a moored platform

The vertical distance between a blade element and the still water level is calculated according to;

$$z(t,i,j) = z_0 + z_{platform}(t) + d(t,i,j) \qquad \text{Equation 5-8}$$

The vertical position of the CoG of the platform (z_0) is assumed to lie on the mean water level. On $t = 10\ s$. the vertical position of the CoG of the platform is given by;

$$z_{platform}(10) = 1.25 \cdot \cos(0.942 \cdot 10 - \pi/10) = -1.187\ (m)$$

The vertical distance between a blade element and the CoG of the platform is given by;

$$d(10,19,1) = 17.5 - (8.665 \cdot \cos(1.2 \cdot 10 + 0)) = 10.188\ (m)$$

Substituting this value in Equation 5-8 then for $(10,19,1)$;

$$\begin{aligned} z(10,19,1) &= -z_{platform}(10) + d(10,19,1) = 1.187 + 10.188 \\ &= 11.38\ (m) \end{aligned}$$

The relative inflow velocity at a blade element is a combination of waves, current and platform motions;

$$U_{rel}(t,i,j) = U_{wave}(x,z,t) + U_{current}(z) + U_{platform}(t,i,j) \qquad \text{Equation 5-9}$$

The horizontal location of a blade element is given by;

$$x(t,i,j) = x_0 + x_{platform}(t) + d(t,i,j) \cdot \theta_{platform}(t) \qquad \text{Equation 5-10}$$

The horizontal position of the CoG of the platform (x_0) is assumed to lie in the origin and is equal to zero. On $t = 10\ s$. the horizontal position of the CoG of the platform is given by;

$$\begin{aligned} x(10,19,1) &= 1.0 \cdot \cos(0.942 \cdot 10 - \pi/10) \\ &+ 10.188 \cdot \pi/90 \cdot \cos(0.942 \cdot 10 - \pi/10) \\ &= -1.287\ (m) \end{aligned} \qquad \text{Equation 5-11}$$

Now, the wave induced horizontal particle velocity can be calculated;

$$\begin{aligned} U_{wave}(-1.287,11.38,10) &= 0.942 \cdot 2.5 \\ &\cdot \frac{cosh\big(0.0425 \cdot (50 - 11.38)\big)}{sinh(0.0425 \cdot 50)} sin(0.942 \cdot 10 \\ &- 0.0425 \cdot -1.287) = -0.076\ (m/s) \end{aligned}$$

The current induced horizontal particle velocity is given by;

$$U_{current}(11.38) = 3.5 \cdot \left(\frac{(50 - 11.38)}{50}\right)^{\frac{1}{7}} = 3.373\ (m/s)$$

The surge- and pitch velocities of the CoG of the platform are needed to calculate the horizontal element velocity;

$$\dot{x}_{platform}(10) = \frac{\left(-0.9496 - (-0.9159)\right)}{0.1} = -0.337\ (m/s)$$

$$\dot{\theta}_{platform}(10) = \frac{\left(-0.0331 - (-0.0320)\right)}{0.1} = -0.011\ (rad/s)$$

The horizontal element velocity due to platform motions is calculated by;

$$U_{element}(10,19,1) = 0.337 + 10.188 \cdot -0.011 = 0.225\ (m/s)$$

Summing the three separate components gives the relative inflow velocity at the blade element;

$$U_{rel}(10,19,1) = -0.076 + 3.373 + 0.225 = 3.52\ (m/s)$$

These hand calculations can be done in a similar way for blade at other moments in time. The results are presented in Table 5 and show that the numerical results agree with the analytical results. This leads to the conclusion that the addition of platform motions has been correctly implemented in the numerical model.

		Analytical results		Numerical results	
time ($\boldsymbol{t}$)	blade (j)	$z(t,19,j)$ (m)	$U_{rel}(t,19,j)$ (m/s)	$z(t,19,j)$ (m)	$U_{rel}(t,19,j)$ (m/s)
10	1	11.38	3.52	11.3833	3.5138
20	2	11.36	3.08	11.3627	3.0788
30	3	25.57	3.16	25.5635	3.1565

Table 5: Analytical results for the moored platform

5.1.3 Conclusions

From Figure 5-1 it is concluded that the simulations with the unsteady BEM approaches gives the exact same results as for the steady model. This means the implementation of the lookup tables and the calculation of the vertical position of the blade element is correctly done.

A more extensive check of the position calculation and the calculation of the inflow velocities by the numerical model is done in Chapter 5.1.2. Analytical platform motions are used as input for the calculations and a check by hand calculations showed that the analytical solutions exactly match the numerical

solutions, see Table 3 and Table 5. From this we can say the unsteady model is successfully verified and implementation of the lookup tables and unsteady inflow field is correctly done.

5.2 Validation with basin tests

A validation study of the unsteady model is done by an analysis of numerical results with measurements obtained from basin tests. The basin tests are described in Appendix A.

In this validation study the different approaches of the numerical model are compared with results of basin tests;

- Approach 1: Actuator disk approach
- Approach 2: BEM – averaged velocities over the three blade elements
- Approach 3: BEM – ring elements divided in three parts

The goal is to validate the numerical code and see how it performs against measurements from basin tests with respect to validity, accuracy and applicability. This should lead to a recommendation on which approach is most suitable to model a tidal turbine connected to a floating platform in an unsteady flow. Different environmental conditions and test configurations will be looked at.

The environmental conditions are a combination of different wave conditions and different current profiles. The test configurations are briefly described in Chapter 5.2.2.

5.2.1 Turbine loads

While in Chapter 3 the validation of the steady BEM model is done by comparing power- and thrust coefficient curves for the numerical simulations and the results obtained from the basin tests, the validation of the unsteady model will be done by comparing time series on the axial load (F_x) of the turbine.

As discussed in the introduction of this report, the floating platform represents a coupled system. Because the full scale platform will have the hub at the distance of 10-12 meters below the still water level, the axial load from the turbine will be an important factor in the external loading on the platform and will influence the motion behaviour of the platform. In this chapter the effect of platform motions on the axial load of the turbine is investigated by comparison between captive and moored configurations and a comparison between two configurations of which one shows drastically different motion behaviour with respect to the other.

The basin tests are done for different values of the tip speed ratio. In this study only the TSR is considered which delivers maximum power output. Looking at the power-coefficient curves presented in Chapter 0 it shows that for the 0° set pitch angle a maximum value of C_p is achieved for TSR = 4.0 (for the steady, numerical model). For a set pitch angle of 15° a maximum is achieved for TSR= 2.5.

During the basins tests, the loads on the turbine are recorded by a load cell. See Appendix A for more information. The load cell directly records the axial load. To calculate the axial load exerted by the turbine, the registered load needs to be corrected for the axial load (drag load) on the turbine strut. The moment around the y-axis of the hub, exerted by the rotor, is calculated by correcting the moment around the y-axis at the load cell by the moment exerted by the turbine strut and the moment exerted by the axial load on the turbine.

$$F_x = F_{x,loadcell} - F_{d,strut}$$ Equation 5-12

The drag force of the strut is described by (9);

$$F_{d,strut} = 1/2 \cdot \rho \cdot A \cdot U^2 \cdot C_{d,strut}$$ Equation 5-13

Where $C_{d,strut}$ is the drag coefficient of the strut and A the frontal area of the strut. The inflow velocity (U) is the only changing variable of the drag force and the drag is proportional to the velocity squared means a correction term for the turbine can be defined;

$$F_{d,strut} \sim U^2$$

$$correction\ term = 1/2 \cdot \rho \cdot A \cdot C_{d,strut}$$ Equation 5-14

The correction term for the starboard and port side turbine has been determined from drag measurements of the floater without rotors, performed by Bluewater (9). This validation study considers the starboard turbine and the correction term for the starboard turbine strut is given by;

$$correction\ term = -8.1702$$

This gives for the drag force on the strut;

$$F_{d,strut} = -8.1702 \cdot U^2$$ Equation 5-15

5.2.2 Test conditions

Two different configurations have been tested during the basin tests. Different ideas lie behind these changes in configurations but due to confidentiality only the main differences are discussed here, only those which are important for correctly modelling the turbine performance for a specific configuration.

- Single rotor: hub depth of 11.75 meters
- Configuration 1: hub depth of 11.75 meters
- Configuration 2: hub depth of 10.00 meters

Configuration 2 showed a much better motion behaviour under the influence of turbine loads, waves, current and mooring loads. Table 6 gives an overview of the different test that will be analysed in the following paragraphs. Test id. 134030, 134036 and 134038 are presented in Appendix C.

configuration		pitch (deg)	TSR	wave maker	wave	$H_s\ (m)$	$T_P\ (s)$	test id.
single rotor	captive	0	4.0	no				131030
single rotor	captive	0	4.0	yes	R0	0	0	134030
single rotor	captive	0	4.0	yes	R6	5.0	6.67	134036
single rotor	captive	0	4.0	yes	R8	5.0	10.0	134038
1	captive	0	4.0	yes	R0	0	0	144030

1	captive	0	4.0	yes	R6	5.0	6.67	144036
1	captive	0	4.0	yes	R8	5.0	10.0	144038
1	moored	0	4.0	yes	R0	0	0	244030
1	moored	15	2.5	yes	R0	0	0	264030
1	moored	15	2.5	yes	R6	5.0	6.67	264036
2	moored	0	4.0	yes	R6	5.0	6.67	944036

Table 6: Test conditions

5.2.3 Current only condition

131030: captive, single rotor (SB – A1), 3.5 m/s current, beta = 0 (TSR = 4.0)

For the current only condition, test id. 131030 was used to validate the numerical models. This is a single rotor test where only one turbine (starboard) is tested under a captive platform in configuration 1 for a 3.5 m/s current velocity. In Figure 5-8, Figure 5-9 and Figure 5-10 the axial load from measurements is presented as the blue graph, the others represent predictions by the numerical models for different current profiles.

Although the platform is held captive and the current is set at a constant velocity the measurement show quite some fluctuations. A larger sinusoidal trend is observed in the measurements as well a smaller periodical fluctuation which is also observed in the numerical predictions by the BEM approach. These fluctuations are explained by the rotation of the turbine blade and the fluctuating loading because of this. Taking into account the sheared velocity profile this means that a sheared inflow does have a small influence on the loading output, but its resulting amplitude on the loading is small compared to the larger fluctuation which is observed.

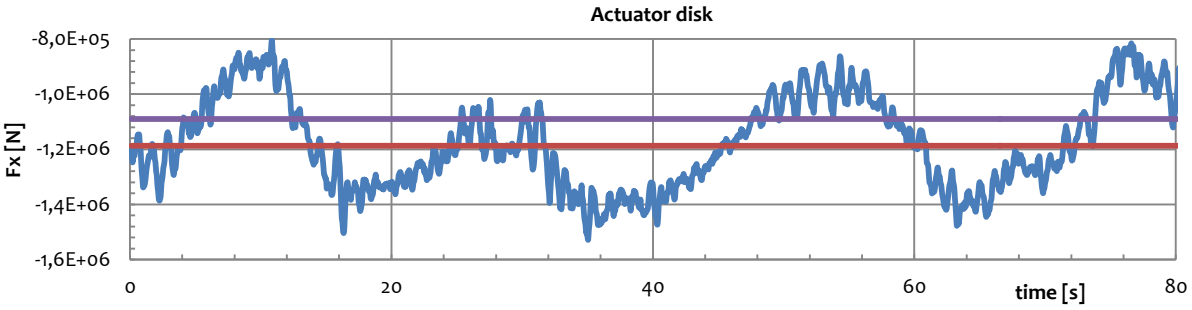

Figure 5-8: Validation of axial load predictions for actuator disk approach, 131030

The predictions by the numerical models for a $1/7^{th}$ power law current profile all are quite close to the mean of the measurements. The profile with wave maker gives higher values in general. It is not exactly known where this current profile is measured in the circulation tank. It could be close to the wave maker or at a distance further away from the wave maker. The platform is positioned at a distance of 2.06 meter from the wave maker. If this profile is measured close to the wave maker it could mean that a not correct velocity profile is used as input for the numerical model and that a $1/7^{th}$ power law profile better suits the real velocity profile in the circulation tank.

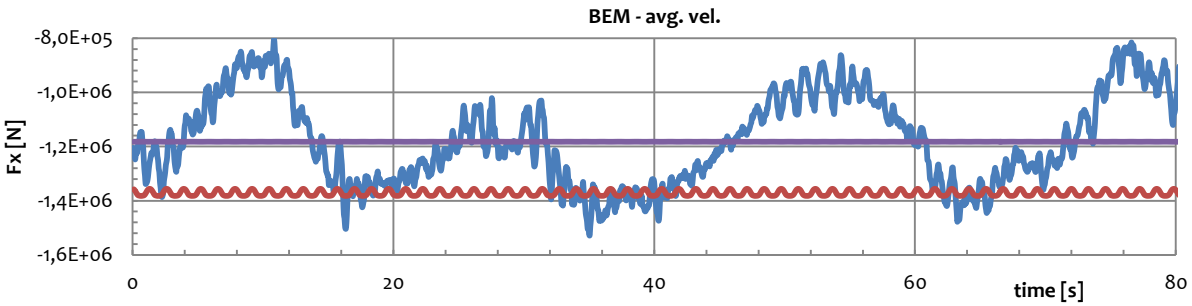

Figure 5-9: Validation of axial load predictions for BEM – averaged velocities approach, 131030

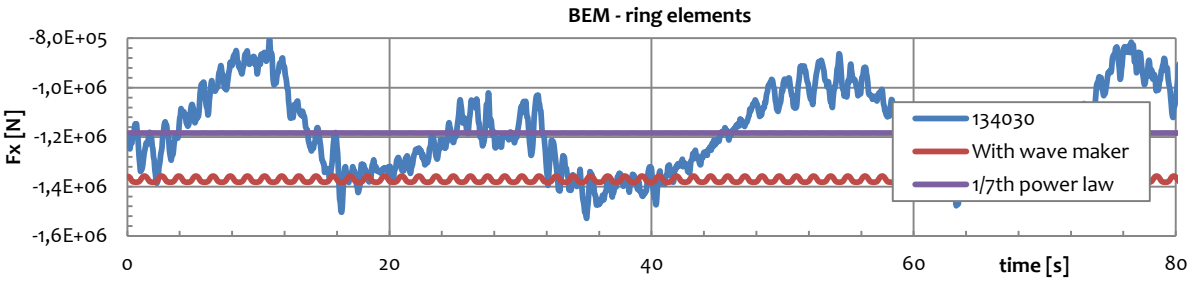

Figure 5-10: Validation of axial load predictions for BEM – ring elements approach, 131030

5.2.4 Waves and current

A number of tests for a captive platform in configuration 1 have been performed in a combined current and waves. No platform motions are present and three different wave conditions are used: R0, R6 and R8;

Wave	Hs (m)	Tp (s)
R0	0	0
R6	5,0	6,67
R8	5,0	10,00

Table 7: Wave conditions

For the R0 wave conditions, two different current profiles are tested; according to a $1/7^{th}$ power law and the profile measured by IFREMER with the wave make installed.

For the R6 and R8 wave condition the IFREMER profiles are used for the combined current and wave condition as described in Chapter 4.2.3.

144030: captive platform, configuration 1, 3.5 m/s current, R0 wave, beta = 0 (TSR = 4.0)

Figure 5-11 and Figure 5-12 show the validation against test id. 144030. This test condition is exactly similar to test id. 133030.

Here, the results are shown for each current velocity profile so that the different approaches can be compared more easily. It is shown that both BEM approaches show very similar results. This is presented in Figure 5-13.

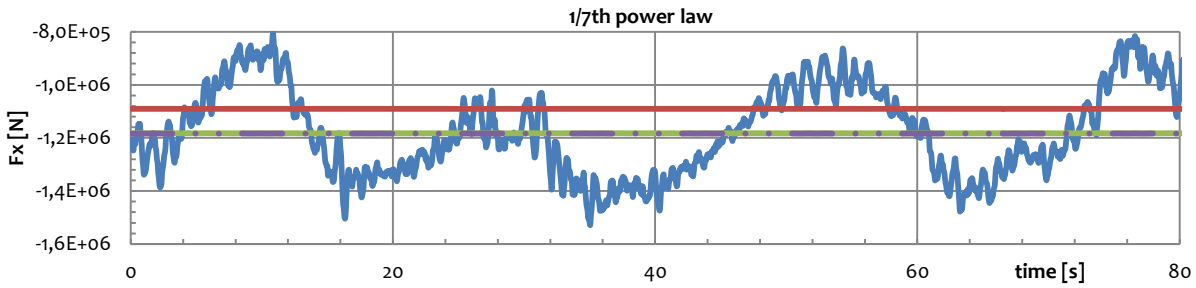

Figure 5-11: Validation of axial load predictions in 1/7th power law current field, 144030

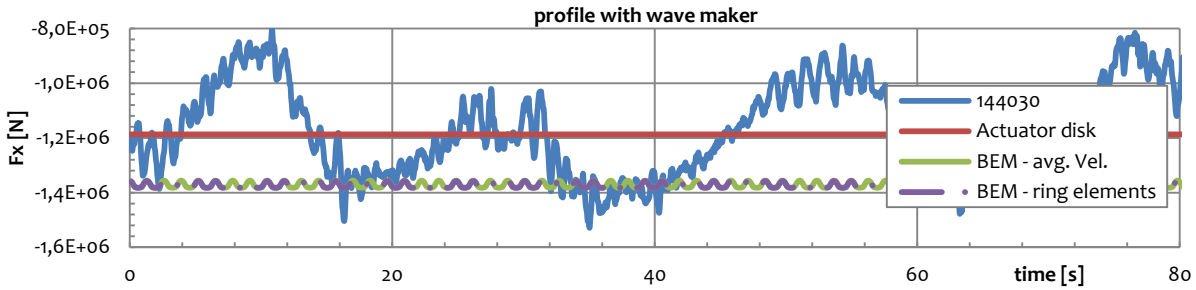

Figure 5-12: Validation of axial load predictions for current profile with wave maker, 144030

Figure 5-13 shows an enlarged part of Figure 5-12. It is clear that the differences between the two BEM approaches are very small. Near the bottom of the graphs the predictions are quite similar, near the maxima of the graphs it is shown that the BEM approach according to averaged velocities gives a little bit smaller values. The different approaches thus give quite similar results but as was discussed in the reflection of Chapter 4.5.1, the BEM approach according to 1/3 ring elements does not show a consisted approach with respect to the classical BEM theory.

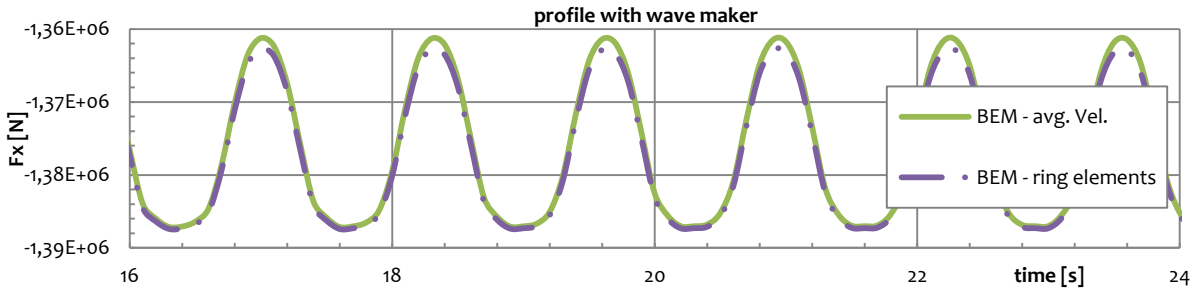

Figure 5-13: Comparison between BEM approaches

Combining the lack of consistency in the BEM approach with ring elements and the similar predictions with respect to the BEM approach according to the averaged velocities, further validation is only done for the BEM approach with averaged inflow velocities.

144036: captive platform, configuration 1, 3.5 m/s current, R6 wave, beta = 0 (TSR = 4.0)

Figure 5-14 and Figure 5-15 show the results of the validation for combined current and waves. Simulations are performed for a wave with 5.0 meter significant wave height and 6.67 seconds peak period. Different

profiles are used to model the current velocity profile; profile with wave maker, a 1/7th power law and the IFREMER profiles which represent the wave-current interaction.

Figure 5-14 shows the validation for the actuator disk approach and the different current profiles. The method shows a nice agreement with the measurements. The mean value of the numerical model fits the mean value of the measurements and the same periodical behaviour is observed for the measurement signal and the numerical predictions, this shows that a drag coefficient of 0.8 is a good value for the turbine under these conditions. The period is equal to the peak period of the waves and is completely caused by the wave loading. The amplitude of the numerical predictions is slightly higher than the amplitude of the measured signal. The amplitude is caused by the fluctuating inflow velocity due to the combined current and waves and the theory seems to give higher fluctuations in velocity than those that occur during the basin test. The lower inflow velocities in the basin test could be the result of turbulence as well, an effect that is not modelled in the numerical simulations.

The 1/7th power law current profile delivers the best fit with the measurement data. The profiles measured in the circulation tank result in higher axial loading. The two profiles from the circulation tank, the one with wave maker and the "IFREMER" profiles give quite similar results.

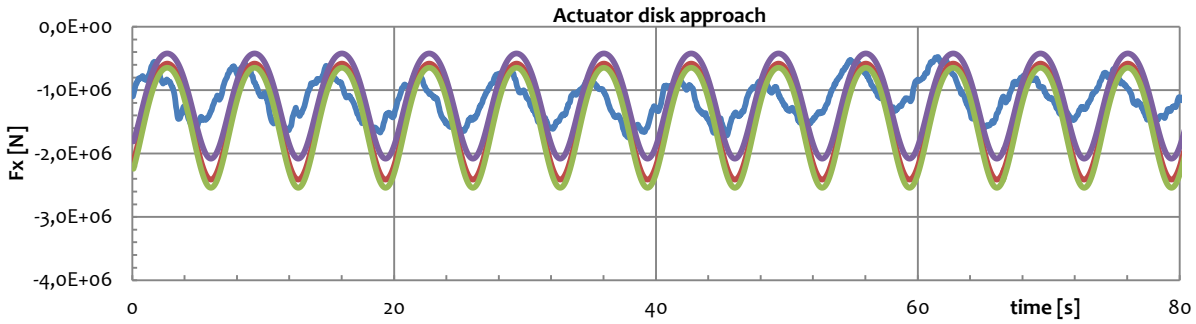

Figure 5-14: Validation of axial load predictions for the actuator disk approach, 144036

Figure 5-15 shows the validation of the BEM approach with the averaged velocities. Again the same periodical behaviour is observed, but this approach also shows much larger fluctuations in the axial load. The mean value for the axial load is much higher for the BEM approach, something that was observed for the current only condition too. The same trend as with the actuator disk approach appears with respect to the results for the current velocity profiles.

The cause of higher amplitudes in axial loading for the BEM approach could be in the generation of the lookup tables by the steady BEM model, normal force coefficient can be over-predicted. But from the validation in Chapter 3 the steady BEM model showed quite good agreement for TSR = 4.0. It is very likely the effects that occur around the model during the basin test cause a reduction in axial load fluctuation, effects that are not taken into account for in the numerical model.

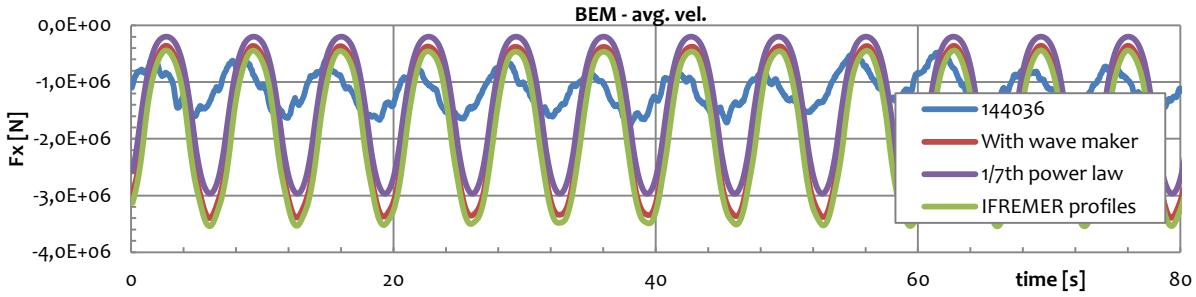

Figure 5-15: Validation of axial load predictions for BEM – averaged velocities approach, 144036

134038: captive, single rotor (SB – A1), 3.5 m/s current, R8 wave, beta = 0 (TSR = 4.0)

The same validation is done for a different wave condition, a wave with the same amplitude as described above but with a different peak period of 10.0 seconds. Again the actuator disk approach shows a good agreement with the measurements, the amplitudes of the predictions are similar to the amplitude of the measurements. For the BEM approach a same trend is observed as for the wave condition R6, although the differences between the amplitudes of the BEM predictions are closer to the amplitude of the measurement.

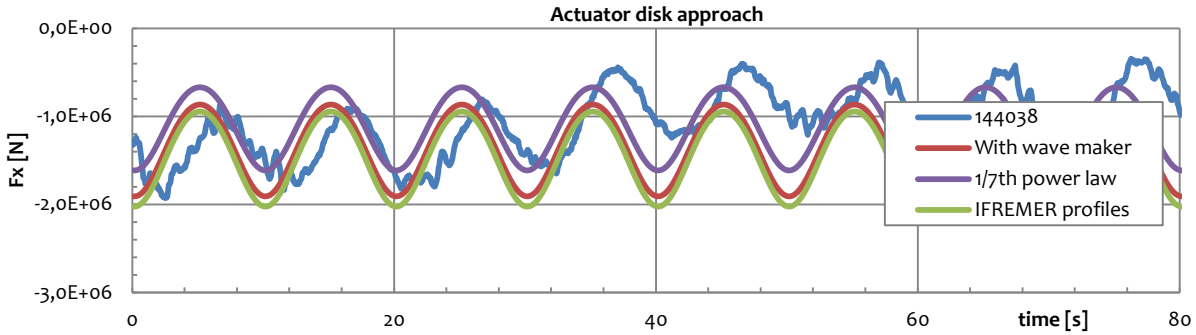

Figure 5-16: Validation of axial load predictions for the actuator disk approach, 144038

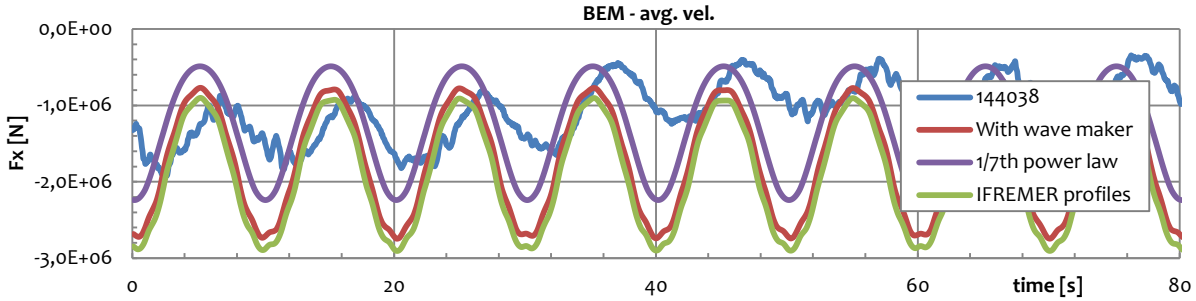

Figure 5-17: Validation of axial load predictions for BEM – averaged velocities approach, 144038

5.2.5 Moored tests

Chapter 5.2.5 discusses the validation of numerical simulations for a moored platform. Simulations with configuration 1 and 2 are both compared to measurement data and different pitch angles are looked at. For the 15° set pitch angle different lookup tables are generated from the steady BEM model. Two current velocity profiles are considered, the 1/7th power law and the IFREMER profiles for combined current and waves. For wave condition R0, the current velocity profile with wave maker is used. For the 15° set pitch angle a TSR of 2.5 is used, for this value the highest value of C_p was obtained, see Figure 3-14.

244030: moored platform, configuration 1, 3.5 m/s current only, beta = 0 (TSR = 4.0)

Figure 5-18 and Figure 5-19 show the results for test id. 244030; the current only condition for the moored platform in configuration 1 and an 0° set pitch angle. Used current velocity profiles are a 1/7th power law and the current profile with wave maker installed.

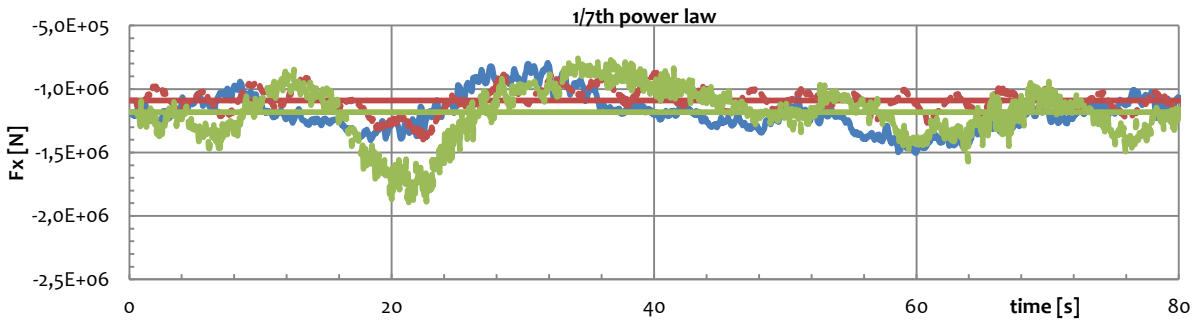

Figure 5-18: Validation of axial load predictions in 1/7th power law current field, 244030

The influence of platform motions is illustrated by plotting the numerical predictions for a moored platform and a captive platform, for both approaches and both current profiles. Figure 5-18 shows quite a good agreement between both numerical approaches and the measurements. The BEM approach seems to responds with a wider margin on the platform motions around t = 20 seconds, but generally the trend of the measurements is followed pretty well. The mean values for the captive platform are close to the mean of the measurements.

Figure 5-19 show the validation of the numerical approaches for the current profile with wave maker. A larger spread between the results is observed and generally the axial loading prediction is a bit higher than the measured values. This is the same trend as was observed for the current only tests.

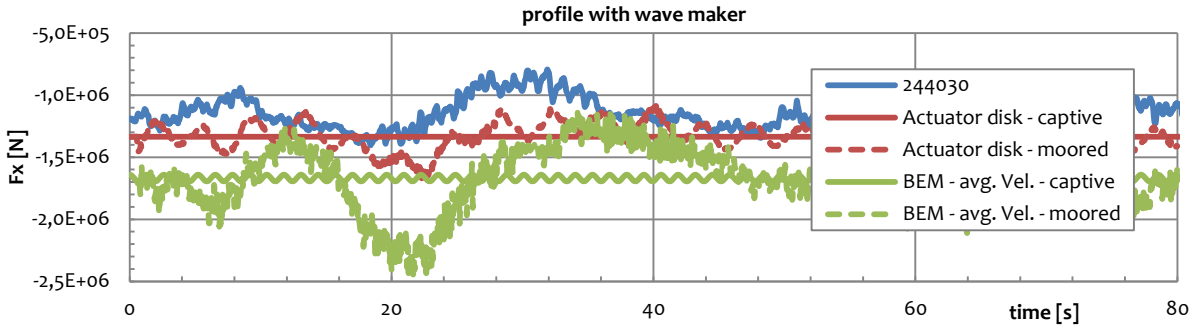

Figure 5-19: Validation of axial load predictions for current profile with wave maker, 244030

264030: moored platform, configuration 1, 3.5 m/s current only, beta = 15 (TSR = 2.5)

The previous test is repeated for a 15° set pitch angle. Again numerical predictions are all quite close to each other but bigger differences are observed with the measurement data. Again the profile with wave maker shows a larger spread. In Chapter 3 it was concluded that the steady BEM model delivered good results for the design condition of 0° set pitch angle and a 3.5 m/s current velocity. The results shown below are for an off design condition of the turbine and the steady BEM model delivered less accurate results for this condition. This explains the larger offset with the measurement data as is observed for the 0° set pitch angle, as the results of the steady BEM model were not as accurate for the 15° set pitch angle.

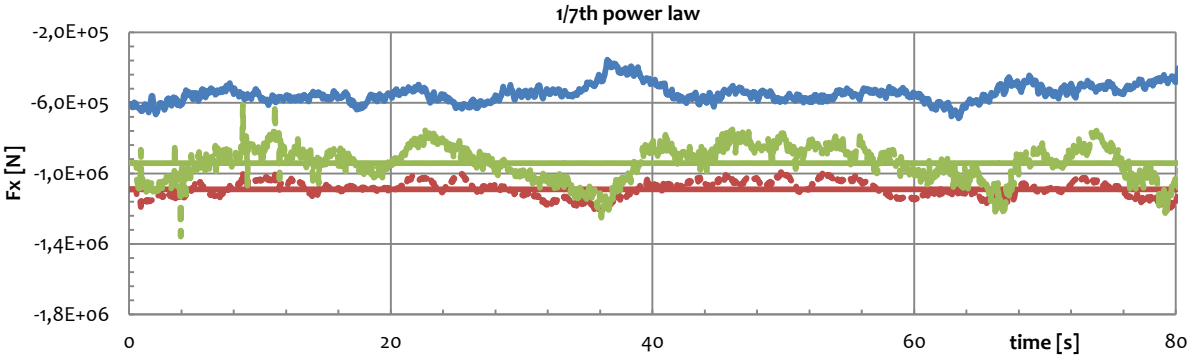

Figure 5-20: Validation of axial load predictions in 1/7th power law current field, 264030

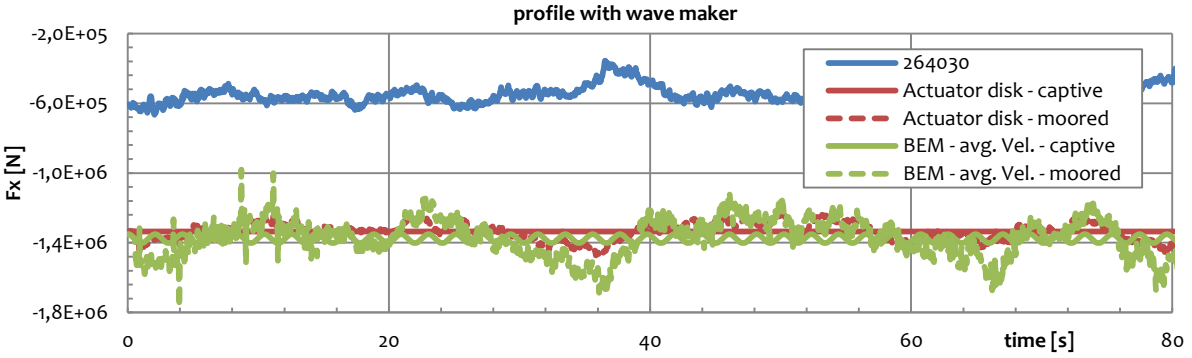

Figure 5-21: Validation of axial load predictions for current profile with wave maker, 264030

944036: moored platform, configuration 2, 3.5 m/s current, R6 wave, beta = 0 (TSR = 4.0)

The figures below show the results of the validation for combined current and wave condition. Predictions and measurement are show for a moored platform in configuration 2, with the shallow hub depth. The turbine is operating in its design condition; incoming waves have 2.5 meter amplitude and a peak period of 6.67 seconds.

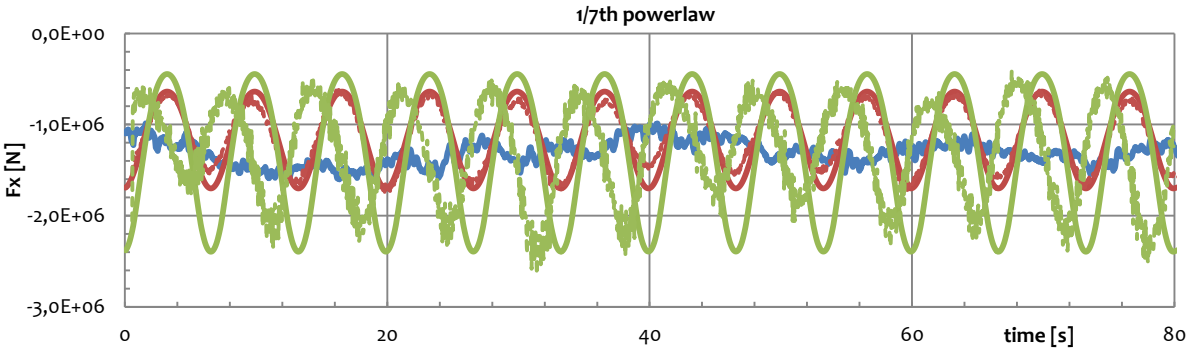

Figure 5-22: Validation of axial load predictions in 1/7th power law current field, 944036

To illustrate the effect of platform motions, again a simulation is performed for captive platform as well as a moored platform. For both conditions the numerical results show the same frequency in the axial loading as the wave frequency. For a moored platform however the amplitude of the loading is more affected by the platform motions and shows a more irregular line, the amplitude for the captive platform is quite constant in time.

Observing Figure 5-22 and Figure 5-23 we must conclude that for a moored platform the numerical models do not seem to be able to predict the general behaviour what is shown in the results of the basin tests. While for the captive current only tests and the captive tests under influence of waves and current the response on wave loading could be observed in the numerical predictions as well as in the measurements, the analysis of the moored tests does not show this effect.

From these results we can conclude that the one-way approach; the effect of platform motions on turbine loading (Figure 1-3), is relatively small. The irregularity observed in the numerical predictions in Figure 5-22 and Figure 5-23 show a small effect, but not a big as illustrated by the measurement.

The measured axial load shows quite a constant loading over time, even though the platform is subjected to a high fluctuating wave loading and resulting platform motions. For the captive platform it was shown that this wave loading could be observed in the measurements as well. This leads to the conclusion that the presence of platform motions removes the peaks from the turbine loading.

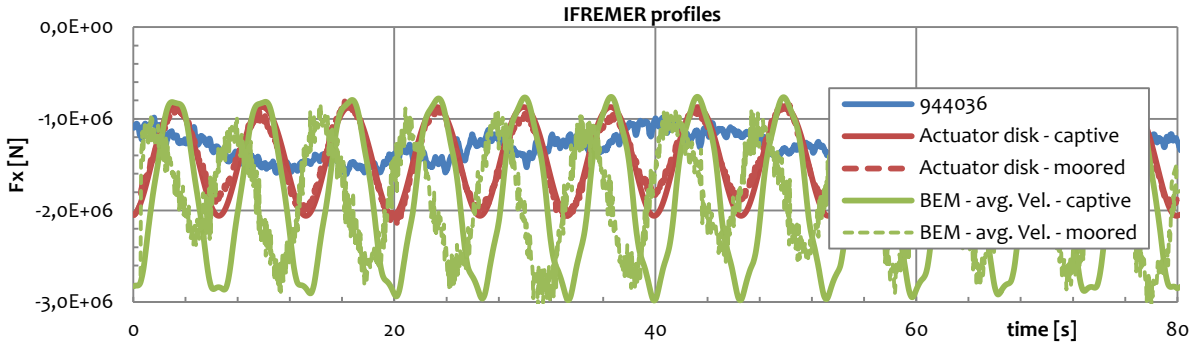

Figure 5-23: Validation of axial load predictions for IFREMER profiles, 944036

5.3 Discussion

From the validation study presented in the previous paragraph we can conclude that in general the numerical models are quite good capable of prediction the axial load output for captive tests in the current only condition and current and wave condition. The actuator disk approach looks to be better capable of approaching the mean value and amplitude of the axial load measured during basin tests. The BEM approach over predicts this mean and shows a higher amplitude.

A current velocity profile that is distributed according to a $1/7^{th}$ power law delivers a better result in all cases than other current velocity profiles (with wave maker, IFREMER profiles).

6 Analysis of the effects of platform motions

In Chapter 6 a number of comparisons will be made between different tests in the circulation tank. Because Chapter 5 concluded that the numerical approaches were not able to correctly predict loading behaviour for a moored platform, this chapter focuses on the analysis of the measurement data and a link is made between the platform motions and the registered axial turbine loading.

Chapter 6.1 presents different comparisons to point out the effects of platform motions on the axial loading of the turbine. Chapter 6.2 shows the effect of platform motions on the (calculated) relative inflow velocity.

6.1 Analysis of basin tests

Three comparisons are made, all pointing out different areas of interest.

1. Captive vs. moored platform, configuration 1 for the current only condition;
2. Captive (configuration 1) vs. moored (configuration 2), current and waves (C3 & R6);
3. Moored, configuration 1 vs. configuration 2, current and waves (C3 & R6).

These 3 cases are discussed in the following 3 sub-paragraphs.

6.1.1 Effect of moored platform

Figure 6-1 shows the time registrations of the axial load for two different test cases. Both graphs give the axial load for configuration 1, but one is shown for a captive platform while the other is in moored condition. The platform is subjected to current only. Figure 6-2 shows the registered platform motions and velocities for the moored platform.

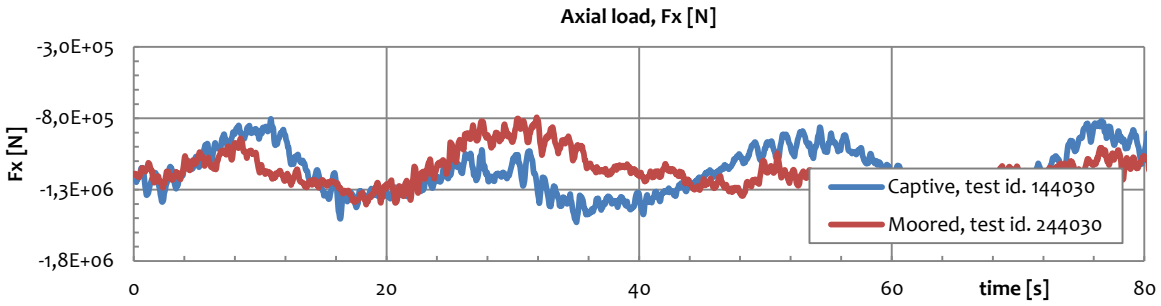

Figure 6-1: Effect of moored platform on axial turbine load in current only condition

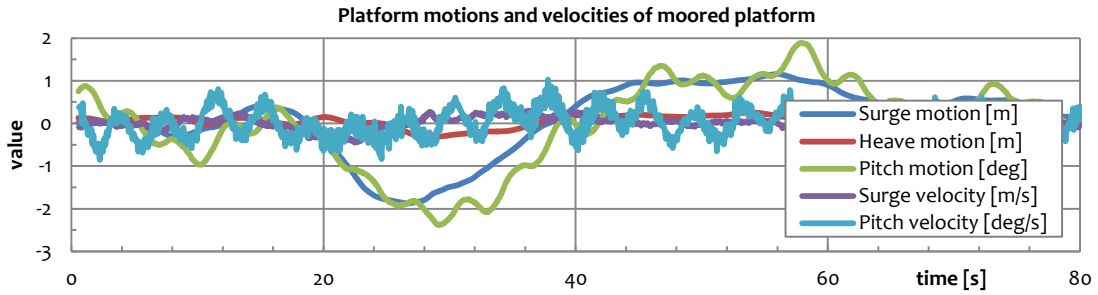

Figure 6-2: Platform motions and velocities of a moored platform in current only conditions

It is observed that for the current only condition there is no big difference between a captive and moored platform with respect to the axial load on the turbine. This is illustrated by the time registration of the platform motions and velocities of the moored platform. These all shown very small fluctuations which results in close to zero contribution to the relative inflow velocity. This explains why in Figure 6-1 the graphs for the captive and moored platform show the same mean, maximum and minimum values for the axial load.

6.1.2 Effect of waves on captive & moored platform

In Figure 6-3 the axial load for the same configurations is presented as in the previous paragraphs, but now the platforms are subjected to waves as well. The wave condition is R6; 5.0 meter significant wave height and a peak period of 6.67 seconds.

For the captive test, configuration 1 platform, the same behaviour is observed as in the previous chapter, where the axial load shows a sinusoidal behaviour with the same frequency as the wave frequency. The mean is almost equal to the mean observed for the current only conditions which means that the fluctuating behaviour and the magnitude of the amplitude is determined by the varying inflow velocity caused by the orbital motion due to the presence of waves.

The moored test is done for a configuration 2 platform. The same trend is observed as for the moored test of configuration 1, only the mean value is a little bit higher. Figure 6-4 shows the platform motions and velocities for test id. 944036 and there are especially big excitations observed for the pitch motion and velocity. Other degrees of freedom show very low excitations which are the result of the hull geometry of configuration 1. For each DoF presented in Figure 6-4 the wave frequency is recognized.

The most important conclusion from Figure 6-3 is that the presence of platform motions on a moored platform removes the peaks from the loading which are caused by the wave loading for a captive platform. This was already noticed in the validation study of the unsteady model. The numerical models were not able to predict this behaviour because the coupling from turbine loading to platform motions is not accounted for in the numerical model.

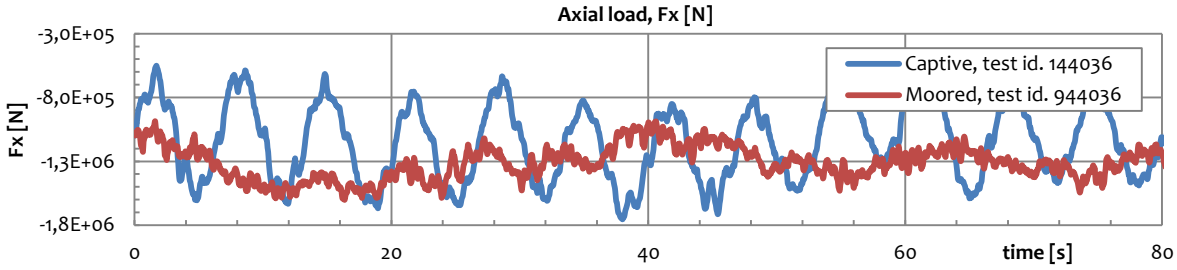

Figure 6-3: Effect of moored platform on axial turbine load under influence of combined current and waves

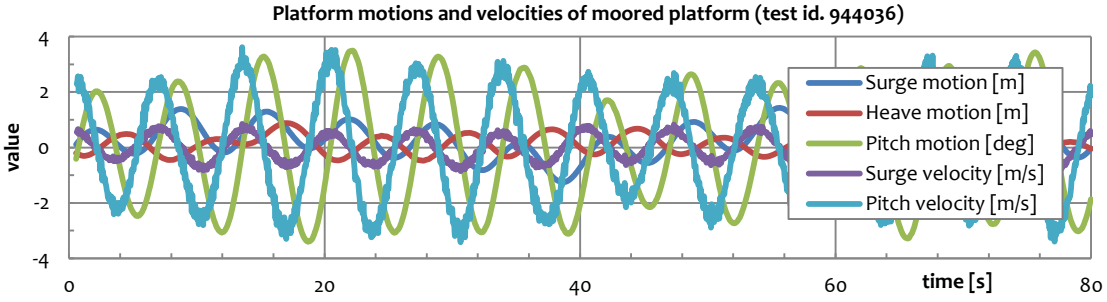

Figure 6-4: Platform motion and velocities for test id. 944036

Comparing the general behaviour of the axial load for a moored platform in configuration 2 with configuration 1 shows that platform motions, in this case pitch behaviour, does not influence the turbine loading in big effect. It is more likely that the higher means values for configuration 2 are caused by higher average inflow velocities. These are the result of the lower hub depth for configuration 2, resulting in higher inflow velocity due to wave because of larger orbital motions and a higher current velocity closer to the water surface.

6.1.3 Effect of waves on moored platform

Figure 6-5 shows the influence of hub depth and different motion behaviour on the axial loading of a turbine. The platform motions and velocities are shown in Figure 6-6 for configuration 1 (left) and configuration 2 (right). The axial load outputs do not show very large differences between the two configurations. What was observed earlier is shown here again, configuration 2 seems to result in a fraction higher mean loading.

Interesting is the comparison of the motion behaviour of the two configurations and the behaviour of the axial loading. While there is a significant difference for especially the pitch behaviour of the two configurations, this does not seem to affect the axial load of the turbine. The surge motion shows quite the same behaviour. Heave motion, pitch motion and – velocity show much lower values for configuration 2, but this does not result in lower axial loading. Again, platform motions do not really influence turbine loading in a large manner, the magnitude of the loading is mostly affected by the vertical location of the turbine in the water column.

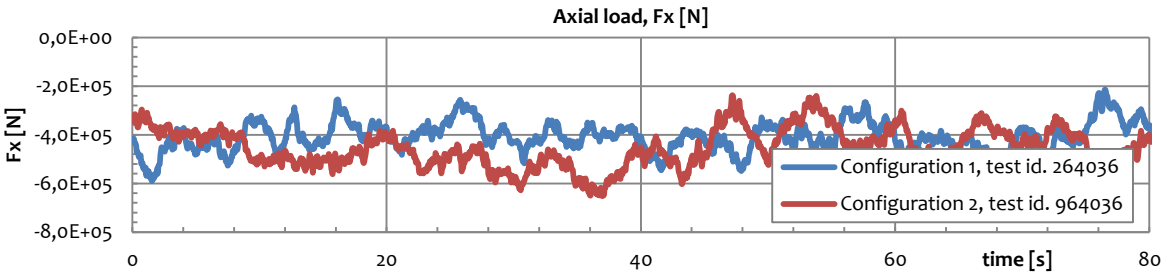

Figure 6-5: Effect of combined current and waves on a moored platform

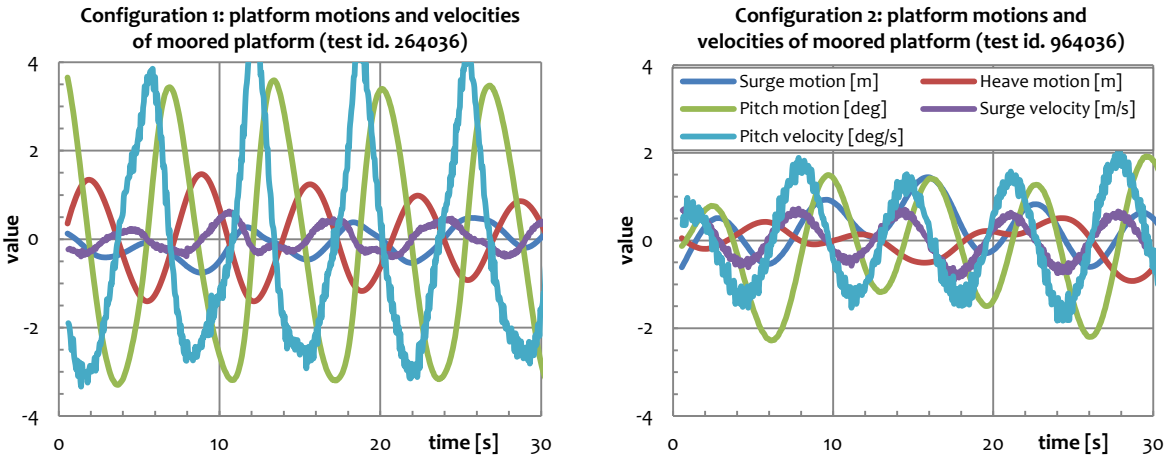

Figure 6-6: Comparison of platform motions and velocities for configuration 1 & 2 under influence of current and waves

6.2 Platform motions and the unsteady flow field

Chapter 6.2 discusses the effects of platform motions on the unsteady flow field. In previous comparisons it was shown that platform motions result in a more constant loading characteristic of the turbine. Platform motions seem to even out the peaks in the axial loading that are observed when a captive platform is subjected to combined current and wave loading. A more constant loading implies that the relative inflow velocity on the turbine is more constant too.

Figure 6-7 shows the axial load for a moored platform, configuration 1 under combined current and wave loading (C3 & R6). Set pitch angle in this specific case was 15°, and results are shown for a tip speed ratio of 2.5. Numerical predictions are shown for both a captive and moored platform according to the actuator disk approach. This approach produced results most close to the measured data in Chapter 5.

It shows that the predictions for the moored platform (dotted red line) actually show larger amplitude than the predictions for the captive platform (straight red line).

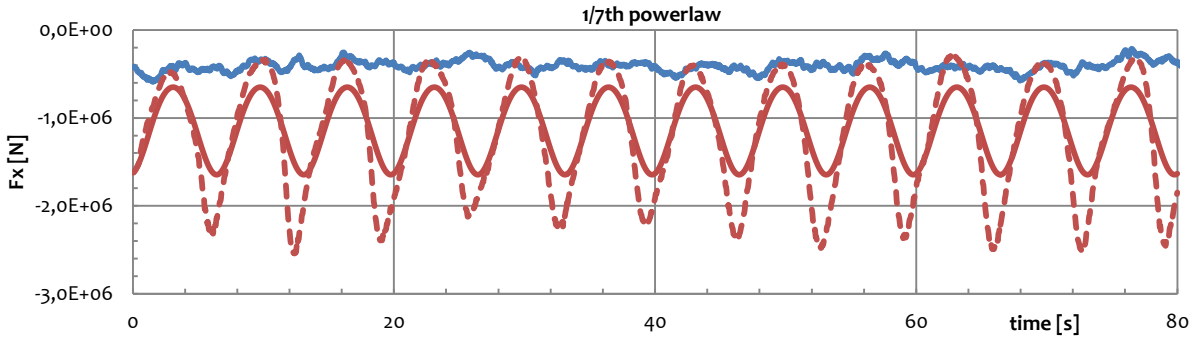

Figure 6-7: Comparison of axial load predictions in 1/7th power law current field and test id. 264036

Figure 6-8 and Figure 6-9 show the platform motions and velocities respectively of the moored platform. A graph of the wave elevation is shown as well. These again are time registrations of the basin tests and the pitch motion and –velocity shown the larger amplitudes.

Figure 6-10 shows the vertical distance between the centre of the most outward blade element on blade 1 and the mean water surface for the captive and moored platform. This shows this distance is not that much influenced but that does result in higher relative inflow velocities, which are presented in Figure 6-11. These larger (theoretical) inflow velocities for the moored platform explain the increasing amplitudes of the prediction loading for the moored platform in Figure 6-7.

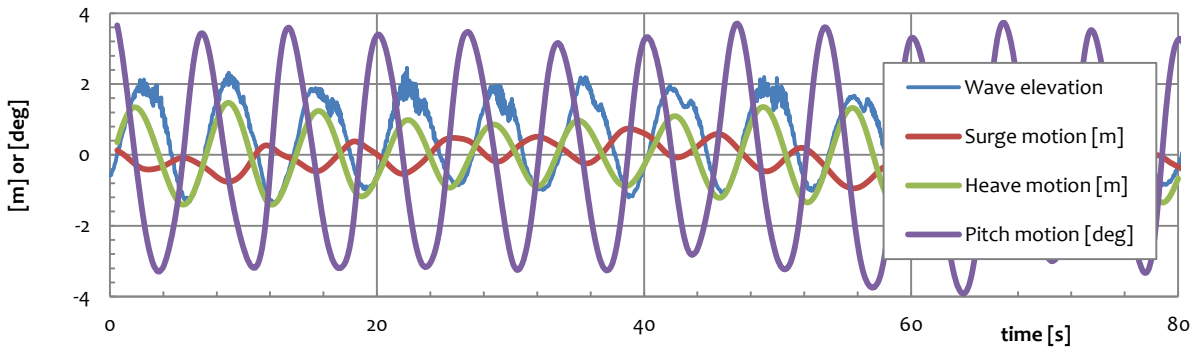

Figure 6-8: Wave elevation and surge-, heave- and pitch motion for test id. 264036

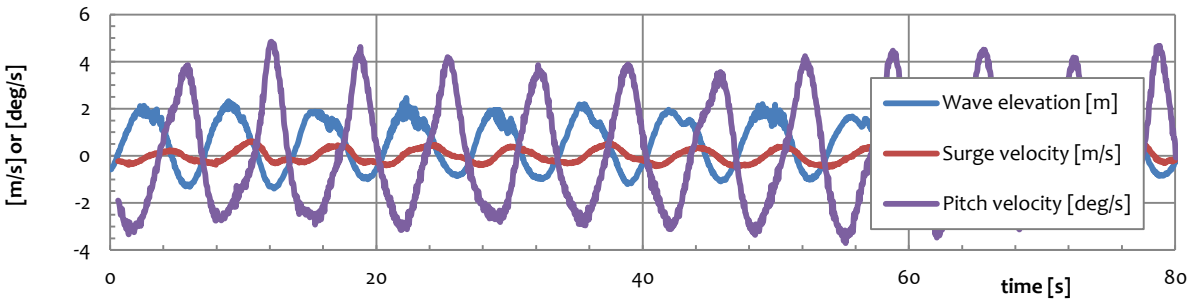

Figure 6-9: Wave elevation and surge- and pitch velocity for test id. 264036

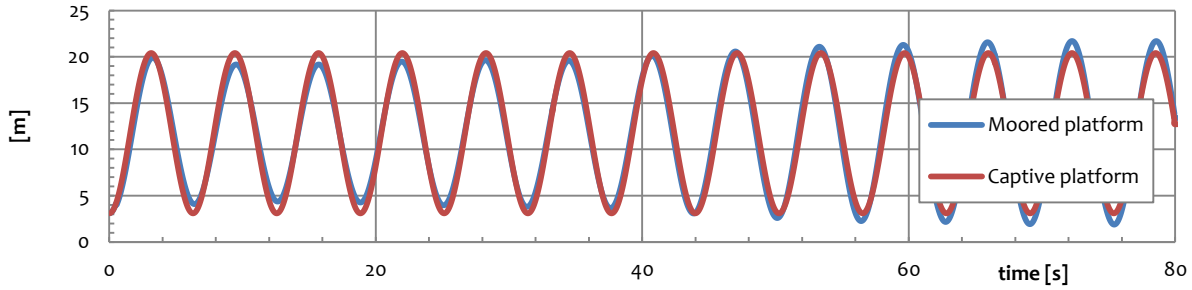

Figure 6-10: Comparison of distance of the centre to mean water surface for a captive and moored platform (blade 1, most outward blade element, configuration 1)

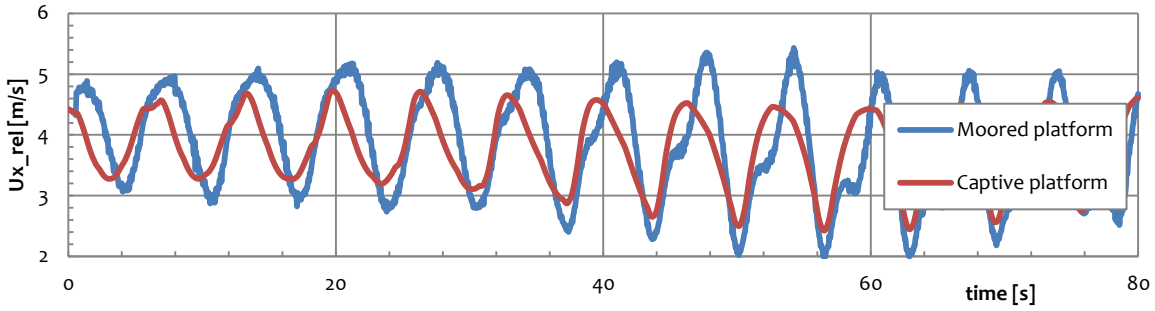

Figure 6-11: Comparison of relative inflow velocities for a captive and moored platform (blade 1, most outward blade element, configuration 1)

6.3 Discussion

Comparison of time registrations of axial loading and platform motions show that lower platform motions do not necessarily result in lower turbine loadings. Platform motions do increase the relative inflow velocity on a blade element and this result in larger amplitude for the predictions axial load for a moored platform.

Measurements show however that peaks in axial loading that occur for a captive platform under influence of combined current and waves even out in moored configuration under the same conditions. This effect is not predicted by the numerical model. A possible explanation could be the phase shift between the platform motions and –velocities and the wave elevation. There is an uncertainty in the time registration of these data points. Instead of amplifying the predictions for the captive platform this could result in a more constant loading for the moored configurations.

7 Conclusions

This thesis focused on the influence of the motion behaviour of the platform on the characteristics of the turbine. The aim of the study was to develop a model which is able to calculate the forces on the turbine as a result of environmental inflow fluctuations and platform motions. The objective was to analyse the hydrodynamics associated with a turbine connected to a floating platform and to gain knowledge about the platform motion behaviour under specific environmental conditions.

First, a BEM model has been developed for the steady situation, i.e. uniform inflow across the turbine. This steady BEM model is verified with results of numerical models that are published in literature. In this same literature, results from basin tests are presented. This data combined with data acquired by Bluewater during basin test on a model of BlueTEC served as validation data for the steady BEM model.

An unsteady inflow field is developed as the result of current- and wave velocities and platform motions. The steady BEM model has been expanded so it could be used in an unsteady inflow field. As a comparison the actuator disk theory is applied as well. With these numerical models several simulations have been done in time domain. These time domain predictions of axial loading of the turbine are validated against measurement data from model tests on the BlueTEC model for different configurations of the platform and under different environmental conditions.

7.1 Steady BEM model

The theory of the steady BEM model is discussed in Chapter 2. Chapter 3 discussed the verification and validation of the steady BEM model. The steady BEM model is verified by comparing C_p- and C_t - curves with two numerical models presented by Bahaj (8). 2-D lift- and drag characteristics for the geometry used by Bahaj have been generated according to the method described in Chapter 2. The Viterna extrapolation method resulted in similar characteristics as used by Bahaj for small angles of attack. The extrapolation method however resulted in a smaller stall angle for the different foil geometries. This can cause some discrepancies with the results obtained by Bahaj.

For the design case the steady BEM model showed results that agreed very well with the values published by Bahaj, especially around operating values for the tip speed ratio of 5-7. In general, the steady BEM model showed a little bit lower values than the other numerical models and this difference increased for higher pitch angles. This is probably the result of underestimating lift- and drag characteristics for the lower range of angle of attack. Fairly good agreement was found with the data obtained in the cavitation tests.

For smaller tip speed ratio's the steady BEM model shows noticeable differences with the numerical models presented by Bahaj. These models are more complex than only simple BEMT, more corrections are implemented such a wake correction factor and hub loss correction factor. For these lower values of TSR, higher values for the inflow angle are calculated by BEM, as was shown in Figure 3-8. In Figure 3-1 is was shown that for higher angles of attack the lift- and drag characteristics extrapolated by the Viterna method resulted in lower values for lift than were used by Bahaj. This is illustrated by the design case, were for lower tip speed ratio's the power- and thrust coefficient are under estimated, while for higher values of TSR a quite good agreement is found with the other numerical predictions.

The results of the validation with the single rotor test with the BlueTEC platform were presented in Chapter 0. It showed good agreement for the power coefficient curve for the design condition of the turbine, slightly over estimating the coefficients for higher values of TSR. The reason for over predicting the performance of a model test is mainly written to the fact that the numerical model represents the idealized case; only tip losses are accounted for while during model test effects of the hub come in to play, blockage

effects and turbulence effects with are difficult to model in a relatively simple approach like BEM theory is. Striking is the really good fit with the power coefficients curves of the tests for lower values of TSR, while the verification with the numerical models of Bahaj showed an under estimation in this region. The used 2-D lift- and drag characteristics for the IFREMER-LOMC turbine might be really close for the real characteristics of the turbine blade under the conditions for smaller values of TSR.

Looking at the validation of the thrust coefficients with the single rotor test it is observed that thrust is under predicted for lower values of TSR. In this region the drag of the hub might be of influence on the total thrust delivered by the turbine and this is not accounted for in the numerical predictions. For higher values of TSR the predictions fit in-between the measurements. Differences in these measurements are caused by the turbine, rotating in clockwise or anti-clockwise direction, and the position and presence of the platform. These factors influence the flow field the turbine experiences, different axial- and tangential inflow velocities, and cause the differences in turbine performance.

7.2 Unsteady modelling

Chapter 4 discussed the unsteady inflow field as result of current- and orbital velocities combined with hub motions induced by the platform motions. A 2-dimensional flow is assumed with only a vertical shear in the x-z plane. From the platform motions only the surge-, heave- and pitch motion are taken into account. Sway-, roll- and yaw motions are neglected because the data to validate the numerical model is obtained from tests in a unidirectional environment; current and wave direction are aligned with the longitudinal direction of the floater and other DoF are small compared to surge-, heave- and pitch.

The steady BEM model from Chapter 2 has been altered to incorporate this unsteady flow field in the BEM theory; this is explained in Chapter 0. Attention is also given to an approach based on the actuator disk method. In this approach the disk is assumed to be divided in a number of horizontal strips to take into account the vertical velocity shear. This approach is added to the comparison in order to figure out to what extend it is necessary to model a tidal turbine in an extensive manner such as the BEM theory, to investigate the effect of platform motions on turbine loading.

In Chapter 5 the numerical models in an unsteady flow field are validated against time series of axial loading of the turbine that have been obtained during model tests on the BlueTEC platform. Chapter 7.2.1 discusses the results of the actuator disk approach while Chapter 7.2.2 goes further into the two BEM approaches that have been discussed in Chapter 4.5.

7.2.1 Unsteady actuator disk approach

For the actuator disk approach a drag coefficient of 0.8 was chosen for the disk. This value is based on what is used in earlier analysis by Bluewater on the BlueTEC platform. In Chapter 5.2 the validation of numerical predictions with the basin tests is discussed. Simulations with the actuator disk approach have been done to generate time series of the axial load on the turbine under different conditions of the platform and different environmental conditions. It was shown that the actuator disk showed quite good results for the captive platform. The mean values of the axial load are well predicted and for the condition with waves the amplitude of the loading predicted by the numerical approach is of the same order of magnitude as is registered during testing, but still slightly over estimated. It was explained that this is mainly caused by the higher velocity fluctuations calculated in the unsteady modelling of the inflow field.

Comparison with the moored tests showed a less satisfying result. As where in the registrations of the axial loading during model test it is observed that the peaks caused by wave loading look to be damped by the platform motions, the numerical approaches showed actually larger amplitudes than for the captive

platform. The effect that the turbine loading has on platform motions is not accounted for and this might be the reason this more constant output is not predicted by the numerical approaches.

All in all the actuator disk approach looks to be a very simple and fast approach to predict axial loading on the turbine for a captive platform in current only conditions and under combined current and wave loading. Incorporating a more accurate flow field and better estimates for the drag coefficient will improve results. This is a much less computational demanding method than BEMT and by extending the approach is a good solution for modelling the effect of turbine loads on platform motions. This is further discussed in Chapter 8.

7.2.2 Unsteady BEM approach

Two BEMT based approaches are described in Chapter 4.5 and both are validated in Chapter 5.2 just as the actuator disk approach. Comparisons for the captive platform in current only condition showed that the load predictions between the two models barely differed. Based on the inconsistency in the calculation method of the BEM approach according to the 1/3 ring elements, discussed in Chapter 4.5.1, further validation only is done for the BEM approach based on averaged velocities over the blade elements covered by the same ring element, see Figure 4-17.

The same trend as for the actuator disk approach is observed for the BEM approach as well. For the captive platform time series are predicted that are sort of similar to the registrations made during basin test. In general slightly higher mean values and amplitudes are observed.

For the moored platform under current only quite good results were obtained, just as for the actuator disk approach. Especially the current velocity profile according to a $1/7^{th}$ power law delivered a very nice fit with the measurements. Simulation of the moored platform under combined current and wave loading showed the same trend as for the actuator disk approach. Addition of the platform motions in the relative inflow velocity adds the same irregularity in the axial loading as is observed for the measurements. The numerical model fails however to show the more constant output, still the axial loading follows a sinusoidal curve with frequency equal to the wave frequency.

7.3 Effect of platform motions

In Chapter 6 the effect of platform motions on axial loading of the turbine is analysed by comparing differences that occur between a captive and moored platform for different environmental conditions. It was showed in Chapter 6.1.1 that for the current only condition, which is more or less a constant velocity on the turbine, does not show big differences between the moored and captive platform.

When waves are added, the loading on a captive platform clearly shows peaks with the same frequency as the wave frequency. A moored platform will move along with the wave when it hits, thus reduced relative inflow velocity and vice versa when the wave passes. This behaviour causes the peaks in the loading to disappear and result in a more constant loading.

Comparison of time registrations of axial loading and platform motions show that lower platform motions do not necessarily result in lower turbine loadings. Platform motions do increase the relative inflow velocity on a blade element and this result in larger amplitude for the predictions axial load for a moored platform.

Measurements show however the peaks in axial loading that occur for a captive platform under influence of combined current and waves even out in moored configuration under the same conditions. This effect is not predicted by the numerical model. A possible explanation could be the phase shift between the platform motions and –velocities and the wave elevation. There is an uncertainty in the time registration of

these data points. Instead of amplifying the predictions for the captive platform this could result in a more constant loading for the moored configurations.

The effect of only platform motions on the axial is shown by the numerical predictions. However this only translates into small irregularities. The bigger picture is the coupling effect from turbine loading to platform motions is likely to be of bigger influence when observing the numerical predictions where only the effect of platform motions on turbine loading is accounted for. This method failed to correctly predict the axial loading for a moored platform under influence of current and wave loading.

8 Recommendations

For the analysis of turbine performance, BEMT showed to be a good method for a static turbine in a uniform flow field. Time series of power and torque should be compared to see if this is valid for an unsteady approach as well. From the model tests a lot of uncertainties however are present in the calculation of the power output, especially with respect to the exact inflow velocity at the turbine. Time domain simulations for the captive tests in current only condition showed to be sensitive to the current velocity profile. Using the correct velocity profile therefore is of big importance, because small changes already have big influence on the mean value of the predictions.

When the effects of platform motions on turbine loading need to be addressed, a coupled model is necessary. Looking only at the coupling between platform motions and turbine loading (axial load), the actuator disk approach is likely to produce a relative reliable, simple and fast method. A one-way approach as used in this study showed to unable to take into account the effects of turbine loading on platform motions. These showed to be of significant influence.

The actuator disk approach could be incorporated in the coupled model where platform motions are calculated by OrcaFlex and turbine loading is calculated by an external function, as was discussed in (1). This method would only allow for the analysis of the coupling between turbine loading and platform motions, it does not allow for the analysis of turbine performance.

Dividing the disk in smaller elements, also in the vertical direction, allows for calculating moments around the hub in y- and z-direction and allows for taking into account sheared inflow in the horizontal plane. More accurate drag coefficients can be obtained from static drag tests of the turbine. This should be done for different environmental conditions to check if this influences the drag of the turbine disk. Incorporating these more accurate coefficients in the actuator disk approach allows for more accurate predictions.

The BEM approach showed to be a good approach to analyse the turbine performance. Power- and thrust coefficients are well predicted but extending the numerical model by corrections for hub drag, wake corrections and hub loss factor are likely to improve results for higher values of TSR in case of power coefficients and lower values of TSR for thrust coefficients predictions.

The strength though lies in the simplicity of the model; the coupled system is already complex enough. Correct modelling of the flow field around the turbines and platform is of big importance for the correct calculation of the loads and performance. The BEMT itself is quite robust, but is was shown that both the actuator disk approach as well as the BEM approach respond very sensitive to already small changes in the velocity profile that is chosen for the current velocity. Addition of turbulence in the flow field to the calculation of the inflow velocities should be considered as well.

Analysis of the moment around the hub can provide information on the importance of modelling a sheared, unsteady inflow field. A complete uniform inflow field will result in a moment around the hub close to zero, when averaged over time. When a sheared inflow is of big influence, and a sheared inflow is considered as presented in Figure 4-12, it will result in a fluctuating moment. A varying moment around the y-axis of the hub could cause issues with respect to fatigue of the turbine blades.

9 Literature

1. *Hydrodynamic interaction of horizontal axis turbines on a floating offshore tidal energy converter.* **M. Oud.**

2. *The hydrodynamic behaviour of two connected horizontal axis tidal turbines. Definition study of the MSc.thesis: "The effect of platform motions on turbine performance".* **P.C.A. van der Plas.**

3. *Blade element momentum theory in modelling tidal stream turbines.* **H.C. Buckland, I. Masters, J.C. Chapman, J.A.C. Orme.**

4. *Aerodynamics of wind turbines.* **Hansen, Martin O.L.**

5. http://web.mit.edu/drela/Public/web/xfoil/. [Online]

6. *Wind turbine post-stall airfoil performance characteristics guidelines for blade element momentum methods.* **J. Tangler, J. David Kocurek.**

7. *Numerical simulation of the wake of marine current turbines with a particle method.* **G. Pinon, P. Mycek, G. Germain, E. Rivoalen.**

8. *Experimental verfications of numerical predictions for the hydrodynamic performance of horizontal axis marine current turbines.* **A.S. Bahaj, W.M.J. Batten, G. McCann.**

9. *Model tests of Bluetec horizontal axis turbines at IFREMER-Marinet.* **Bluewater Energy Services.**

10. *The prediction of the hydrodynamic performance of marine current turbines.* **W.M.J. Batten, A.S. Bahaj, A.F. Molland, J.R. Chaplin.**

11. *Waves in oceanic and coastal waters.* **Leo H. Holthuijsen.**

12. *Surface buoy effects on F32 deflector.* **IFREMER.**

13. *Theoretical manual of strip theory program "Seaway for Windows".* **J.M.J. Jounée, L.J.M. Adegeest.**

14. *Flow characteristic effects on marine current turbine behaviour and on its wake properties.* **F. Maganga, G. Germain, J. King, G. Pinon, E. Rivoalen.**

Appendix A: The basin tests

Many references are made to measurement data that has been obtained during basin test the BlueTEC platform. The report of these tests (9), gives a very broad insight in the goals, methods and results of these test. The goals and methods will be described shortly in this appendix. The information in this appendix is directly obtained from the report of the model tests (9).

The aim of the tests was to study the concept of the BlueTEC platform in combination with horizontal axis turbines concentrating on turbine performance, mooring loads and platform motions and behaviour in current and waves. During tests, turbine data is collected on power output and forces to investigate the effects of rotating turbines on floating devices and identify differences compared to fixed structures. The general test set-up and a 3-D view of the platform were presented in Chapter 3.3.1. A number of pictures are shown below.

Figure A-1: Model of the turbine mounted on the vertical strut and load cell

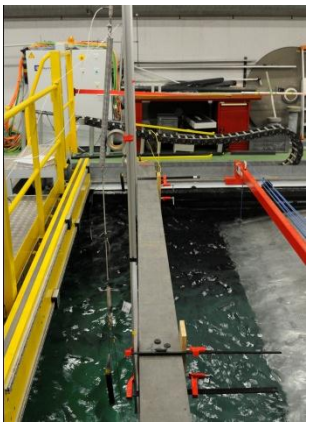

Figure A-2: Picture of the spring assembly to model the mooring lines stiffness

Figure A-3: Picture of the circulation tank with waves

Different quantities are measured during testing such as; wave height, mooring loads, turbine loads, platform motions and turbine performance.

Different configurations are tested:

- Captive platform, configuration 1;
- Moored platform, configuration 1;
- Moored platform, configuration 2.

Multiple rotor configurations were available with different blade pitch angles. Mainly two input parameters are varied: the current velocity and wave height and period. For each test a range of TSR is measured in separate measurements. The test runs could be divided into four categories:

- Current only condition;
- Wave only condition;
- Current & regular waves;
- Current & irregular waves.

Appendix B: The velocity potential

The velocity potential is mentioned in Chapter 4.2. The velocity potential is a mathematical expression which has the property that the velocity component in a point in the fluid in any chosen direction is the derivative of this potential function in that point to that chosen direction. The velocity potential is built up of a number of components and is discussed in here in more detail. Extensive background information can be found in for example (13)

Consider a rigid body, floating in an ideal fluid with harmonic waves. The water depth is assumed to be finite. The time-averaged speed op the body is zero in all directions. The x-axis is coincident with the undisturbed still water free surface and the z-axis and z_0-axis are positive upwards.

The linear fluid velocity potential can be split into three parts:

$$\phi(x, y, z, t) = \phi_r + \phi_w + \phi_d \qquad \text{Equation B-1}$$

In which:

ϕ_r	radiation potential for the oscillatory motion of the body in still water
ϕ_w	incident undisturbed wave potential
ϕ_d	diffraction potential of the waves about the restrained body

In Chapter 4.2.2 the wave velocity has been discussed. The contribution of the radiation and the diffraction potential are considered to be small and are neglected in the calculation of the fluid particle velocities. Besides the potential described above, turbulence is an occurring effect around the platform which adds to the velocity potential. This is effect is neglected as well, but is likely to be of big influence of the total velocity potential. Especially when incoming flow is not unidirectional, or even reversed so that the struts of the turbine are upstream of the rotors. High irregularity of waves will add increase turbulence effects, because the turbine operates closely to the water surface.

From the definition of a velocity potential ϕ follows the velocity of the water particles in the three translation directions:

$$U_x = \frac{\partial \phi}{\partial x} \qquad \text{Equation B-2}$$

$$U_y = \frac{\partial \phi}{\partial y} \qquad \text{Equation B-3}$$

$$U_z = \frac{\partial \phi}{\partial z} \qquad \text{Equation B-4}$$

Appendix C: Test conditions

134030: captive, single rotor (SB – A1), 3.5 m/s current, R0 wave, beta = 0 (TSR = 4.0)

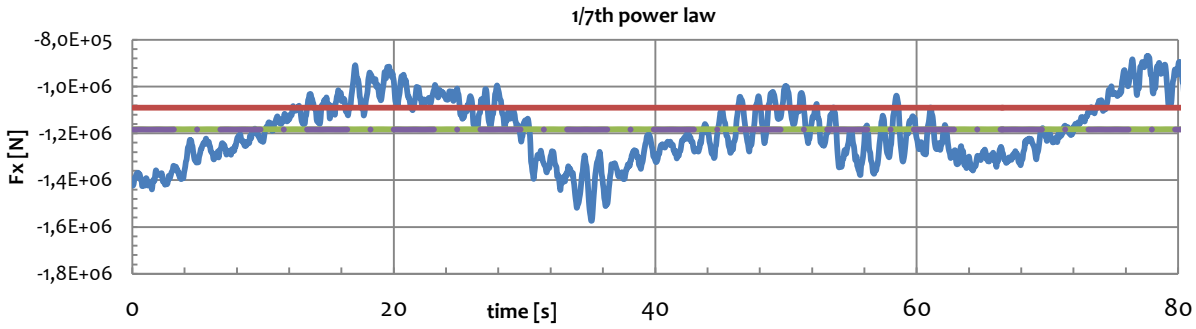

Figure D-1: Validation of axial load predictions in 1/7th power law current field, 134030

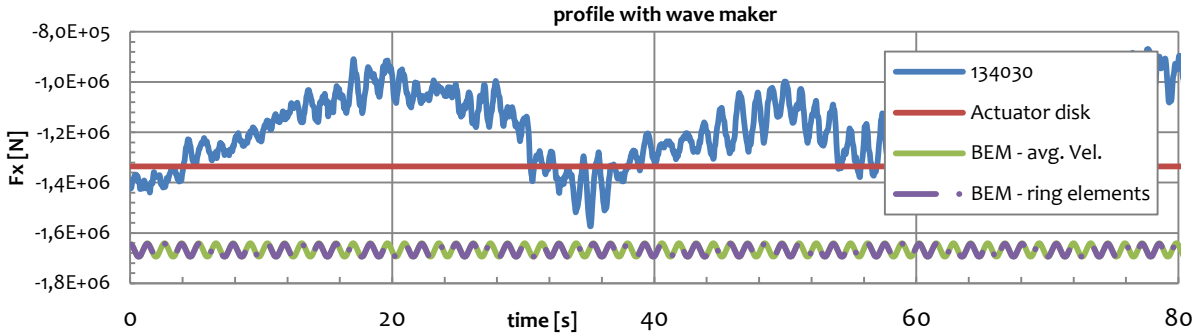

Figure D-2: Validation of axial load predictions for current profile with wave maker, 134030

134036: captive, single rotor (SB – A1), 3.5 m/s current, R6 wave, beta = 0 (TSR = 4.0)

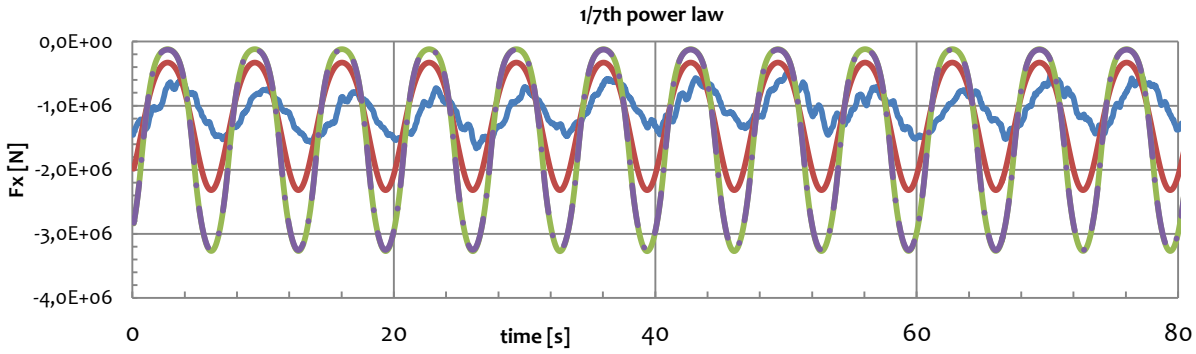

Figure D-3: Validation of axial load predictions in 1/7th power law current field, 134036

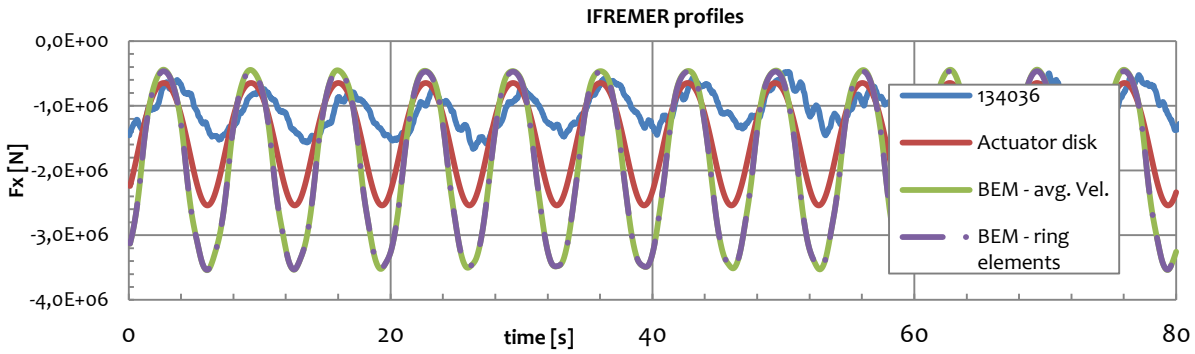

Figure D-4: Validation of axial load predictions for IFREMER profiles, 134036

134038: captive, single rotor (SB – A1), 3.5 m/s current, R8 wave, beta = 0 (TSR = 4.0)

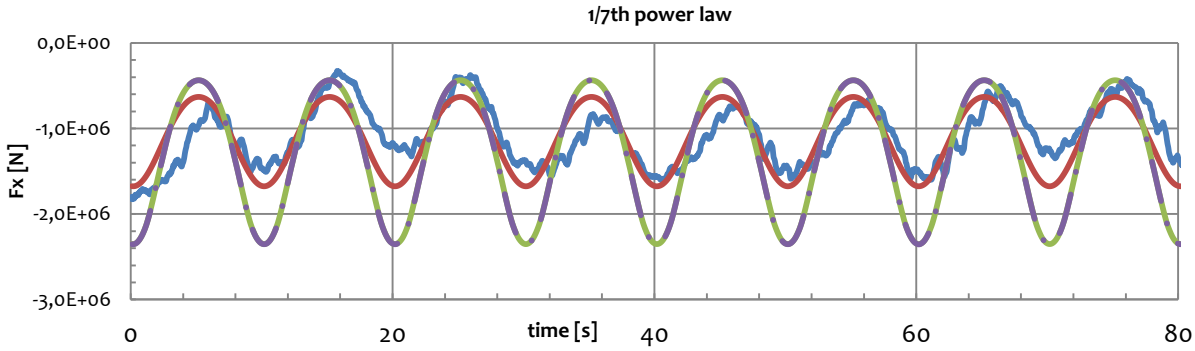

Figure D-5: Validation of axial load predictions in 1/7th power law current field, 134038

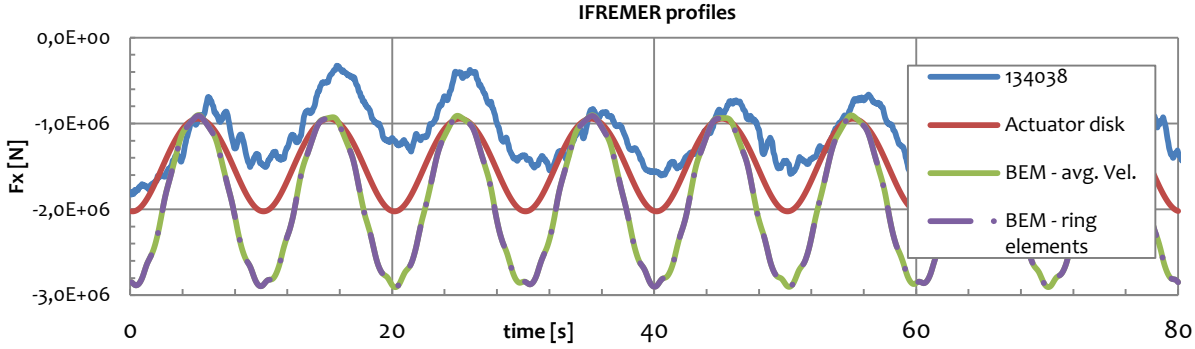

Figure D-6: Validation of axial load predictions for IFREMER profiles, 134038

944036: moored platform, configuration 2, 3.5 m/s current, R6 wave, beta = 0 (TSR = 4.0)

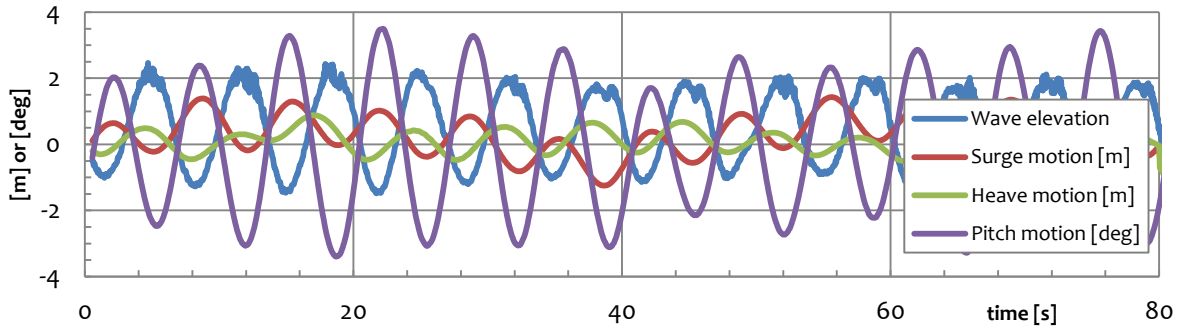

Figure D- 7: Wave elevation and surge-, heave- and pitch motion for configuration 2, 944036

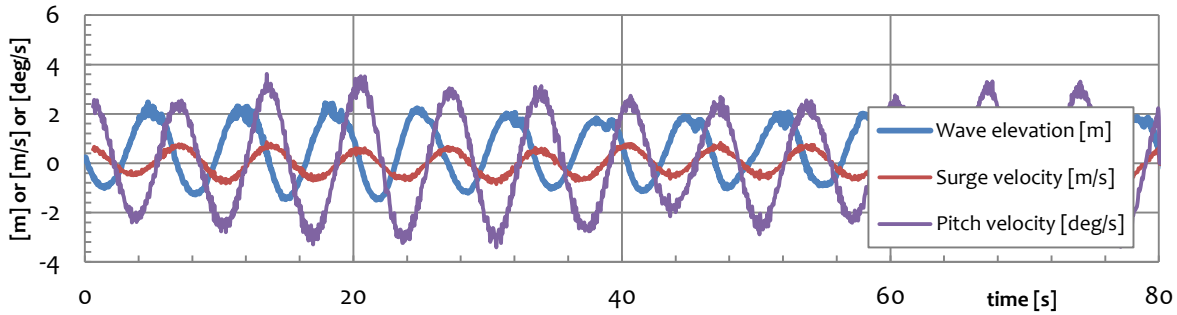

Figure D-8: Wave elevation and surge- and pitch velocity for configuration 2, 944036

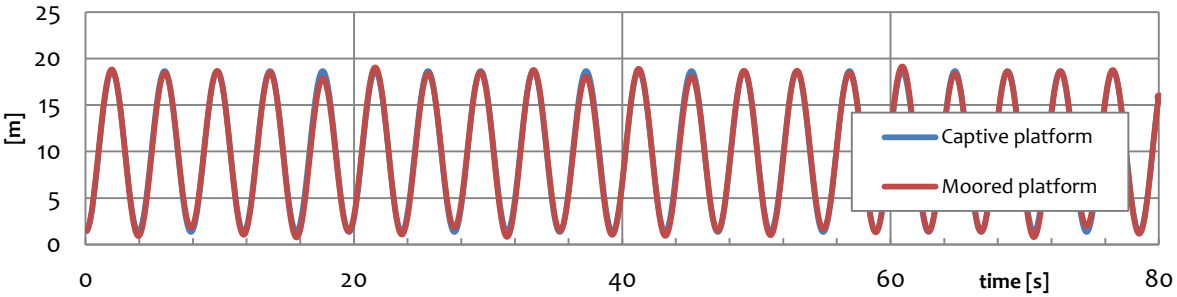

Figure D-9: Comparison of distance of the centre to mean water surface for a captive and moored platform (blade 1, most outward blade element, configuration 2)

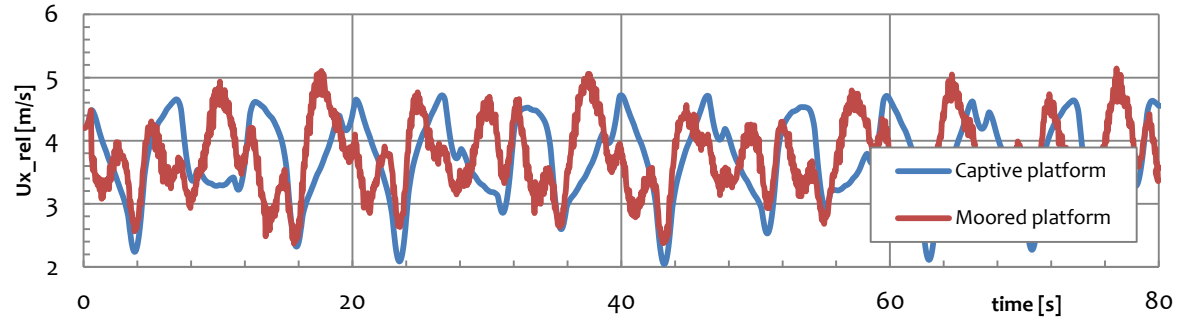

Figure D-10: Comparison of relative inflow velocities for a captive and moored platform (blade 1, most outward blade element, configuration 2)

List of figures

List of tables